ABSTRACT

Title of Dissertation: ULTRA-SMALL SCALE MECHANICAL PROPERTIES MEASUREMENT

Michael Scott Gaither, Doctor of Philosophy, 2011

Dissertation Directed by: Isabel K. Lloyd
Associate Professor
Department of Materials Science and Engineering

Robert F. Cook
Group Leader, Nanomechanical Properties
National Institute of Standards and Technology
Adjunct Professor
Department of Materials Science and Engineering

In order for the microelectromechanical systems (MEMS) industry to continue to grow and advance, it is critical that methods are developed to determine the mechanical reliability of MEMS devices. This is particularly so for advanced devices with contacting, moving components, for which component strength is a key factor in determining reliability. The etching processes used to produce MEMS devices leave residual surface features that typically limit device strength and, consequently, device lifetime and reliability. In order to optimize MEMS device reliability, it is therefore necessary to understand and characterize the effects these etching processes have on MEMS-scale device strengths. At the micro and nano scales, however, conventional strength testing methods cannot be used, and a standardized test method for MEMS-scale strength measurement has yet to be established. The micro-scale theta specimen, shaped like the

Greek-letter theta, acts as a tensile test specimen when loaded in compression by generating a uniform tensile stress in the central web of the specimen. Utilizing the theta specimen for strength measurements allows for simple micro-scale strength testing and assessment of etching effects, while removing the difficulties associated with gripping and loading specimens as well as minimizing potential misalignment effects.

Micro-scale silicon theta samples were fabricated using techniques relevant to MEMS processing. Processing-structure relationships were determined with microscopy techniques measuring sample dimensional variations, etch quality, and surface roughness. Structure-properties relationships were determined using three techniques. Samples were tested by instrumented indentation testing (IIT) and finite element analysis determined sample strength. Sample set strength data were examined via Weibull statistics. Fractographic analysis determined initial fracture locations and fracture propagation behavior.

Key scientific findings included: (1) directly relating the processing-induced etching quality of fabricated samples to sample strength, and (2) critical flaw size calculations from sample strength measurements that were consistent with sample surface roughness. Technical contributions included development of the micro-scale theta specimen fabrication methodology, super-resolution dimensional measurements, and extension of IIT to strength measurements. The micro-scale theta specimen and corresponding testing methodology have enabled successful determination of processing-structure-mechanical properties relationships for three processing approaches. This is vital to the determination of properties-performance relationships in MEMS devices.

ULTRA-SMALL SCALE MECHANICAL PROPERTIES MEASUREMENT

By

Michael Scott Gaither

Dissertation submitted to the Faculty of the Graduate School of the
University of Maryland, College Park, in partial fulfillment
of the requirements for the degree of
Doctor of Philosophy
2011

Advisory Committee:
Associate Professor Isabel K. Lloyd, Chair/Advisor
Adjunct Professor Robert F. Cook, Co-Advisor
Professor Lourdes G. Salamanca-Riba
Professor Manfred R. Wuttig
Professor Hugh A. Bruck

© Copyright by

Michael Scott Gaither

2011

Dedication

To my wife Morgan and my mother Tina, whose encouragement and support made this journey rewarding and possible.

Acknowledgements

I am grateful to my advisors Drs. Robert Cook and Isabel Lloyd for all their generous guidance, expertise, patience, and encouragement throughout this research project. I am grateful to my committee members Drs. Lourdes Salamanca-Riba, Manfred Wuttig, and Hugh Bruck for their time and effort.

I am grateful to many National Institute of Standards and Technology (NIST) staff members for their generous support and expertise. Specifically, I thank Dr. Richard Gates for his training, expertise, and collaboration with the fabrication development during this research project. I thank Dr. Frank DelRio for his guidance as project leader and training and expertise with atomic force microscopy and Mr. George Quinn for his training and expertise with fractography and Weibull statistical analysis. I thank Drs. Edwin Fuller Jr., William Osborn, and Rebecca Kirkpatrick for their generous training, expertise, and collaboration with various aspects of the finite element analysis. I also thank Dr. Gheorghe Stan for his support with the development of the web width image processing routine.

I am grateful to the NIST Nanofab staff for equipment training and fabrication expertise. Specifically, I thank Mr. Laurence Buck, Mr. William Young, Dr. Lei Chen, and Mr. Marc Cangemi for their generous time, patience, and expertise.

My family and friends have been essential to the completion and enjoyment of this research project. Specifically, my wife Mrs. Morgan Gaither has been a constant source of encouragement, the light during dark times. My mother Mrs. Tina Tadsen and step-father Mr. Scott Tadsen have always been my biggest cheerleaders and fans

throughout my education, always letting me know how proud they have been of my efforts and successes. A special thanks to my brother Mr. Bryan Gaither and friend Mr. Brendan Hanrahan for their company in my athletic pursuits during the duration of this research; they helped me keep perspective and a good life balance.

This research was supported by a NIST Cooperative Research Agreement. Research performed in part at the NIST Center for Nanoscale Science and Technology.

Table of Contents

Dedication ii
Acknowledgements iii
Table of Contents v
List of Tables vii
List of Figures viii
Chapter 1: Background and Introduction 1
1.1 The Promise of Micro-Electro-Mechanical Systems (MEMS) 1
1.2 Strength Testing Methodologies 5
1.3 Theta Specimen Testing Prototype 8
1.4 Thesis: Theta-based Approach for MEMS Device Assessment and Optimization 11
1.5 Dissertation Outline 16
Chapter 2: Fabrication and Testing Methodology 18
2.1 Sample Design 18
2.2 Deep Reactive Ion Etching (DRIE) Techniques 21
2.3 Fabrication 21
2.3.1 Step 1: Incoming Wafer 27
2.3.2 Step 2: RCA Clean 27
2.3.3 Step 3: Prime Wafer 27
2.3.4 Step 4: Spin Photoresist 28
2.3.5 Step 5: Expose Front 28
2.3.6 Step 6: Develop Front 29
2.3.7 Step 7: DRIE Front 29
2.3.8 Step 8: Prime Back 31
2.3.9 Step 9: Spin Photoresist 31
2.3.10 Step 10: Expose Back 32
2.3.11 Step 11: Develop Back 32
2.3.12 Step 12: Spray Front 33
2.3.13 Step 13: DRIE Back 33
2.3.14 Step14: Remove Photoresist 34
2.3.15 Step 15: Buffered-Oxide Etch (BOE) 34
2.3.16 Step 16: Final Wafer 35
2.4 Defining Structures 35
2.5 Creating Structures 38
2.6 Preserving Structures 51
2.7 Batch Etch Results 62
2.8 Mechanical Testing Methodology 70
2.9 Summary 73
Chapter 3: Microscopy and Imaging 74
3.1 Surface Roughness Characterization 74

3.2 Web Width Determination 87
3.3 Summary 91
Chapter 4: Finite Element Analysis 92
4.1 Model Configuration 92
4.2 Durelli and Arch Theta Specimens 93
4.3 C-ring Specimen 103
4.4 Gapped-Arch Theta Specimen 107
4.5 Summary 110
Chapter 5: Elastic Behavior 111
5.1 Theta Elastic Deformation 111
5.2 C-Ring Elastic Deformation 115
5.3 Gapped-Arch Theta Elastic Deformation 120
5.4 Summary 122
Chapter 6: Fracture Strength 124
6.1 Strength Measurement and Analysis 124
6.2 First and Second Generation Durelli Theta 125
6.3 Durelli and Arch Theta Strength 126
6.4 Gapped-Arch Theta Strength 136
6.5 C-ring Strength 141
6.6 Summary 144
Chapter 7: Fractography 147
7.1 Material Fracture Behavior 147
7.2 Theta Sample Fracture Behavior 150
7.3 Fracture Mirror Radii 155
7.4 Critical Crack Size Estimation 156
7.5 C-Ring Fractography 158
7.6 Summary 161
Chapter 8: Conclusions and Future Work 163
8.1 Conclusions 163
8.2 Future Work 166
Appendix 169
A. Web Width Determination Procedure 169
References 171

List of Tables

Table 3.1: AFM statistical data for each of the fabricated batches of theta samples including the round and hexagonal batches fabricated as part of the initial generation of thetas. 85

Table 6.1: The Weibull distribution fit data for each set of theta samples. 135

Table 6.2: Weibull distribution fit data for the tested gapped-arch thetas. 140

List of Figures

Figure 1.1: Types of MEMS devices based on the device component feature interactions during operation [Bernstein *et al.*, 1993; Le, 1998; Dudley *et al.*, 2003; Romig *et al.*, 2003; Flater *et al.*, 2006]. DMD: Digital micromirror device. 2

Figure 1.2: Fracture strength as a function of approximate stressed area for single-crystal silicon for a variety of fabrication methods. Data were collected from a large number of sources [Eisner, 1955; Pearson *et al.*, 1957; Sylwestrowicz, 1962; Hu, 1982; McLaughlin and Willoughby, 1987; Johansson *et al.*, 1988; Ericson and Schweitz, 1990; Vedde and Gravesen, 1996; Wilson and Beck, 1996; Wilson *et al.*, 1996; Schweitz and Ericson, 1999; Suwito *et al.*, 1999; Chen *et al.*, 2000; Namazu *et al.*, 2000; Yi *et al.*, 2000; Chen *et al.*, 2002; Sundararajan *et al.*, 2002; Jeong *et al.*, 2004; Quinn *et al.*, 2005; Tsuchiya *et al.*, 2005; Hoffmann *et al.*, 2006; Isono *et al.*, 2006; Nakao *et al.*, 2006; Miller *et al.*, 2007; Zhu *et al.*, 2009; Banks-Sills *et al.*, 2011]. Power law trend lines are shown to highlight the overall behavior of the strength data. TMAH: Tetramethylammonium hydroxide; EDP: Ethylenediamine pyrocatechol; RIE: Reactive ion etching; DRIE: Deep reactive ion etching. 6

Figure 1.3: The first generation theta test specimen designs. (a) Round and (b) hexagonal theta test samples are 300 μm across, and (c) the test strip includes 10 theta samples. Images from Quinn *et al.* [Quinn *et al.*, 2005].. 10

Figure 1.4: The first generation theta specimen fabrication sequence [Quinn *et al.*, 2005]. (a) Photoresist was spun on to the wafer and photolithographically patterned. (b) The theta samples and test strips were formed simultaneously using a through-wafer DRIE step. The photoresist was removed directly after the through-wafer etching. 12

Figure 1.5: The processing-structure-properties-performance relationship for this dissertation with images from each step of the project that will be covered in the following chapters.. 15

Figure 2.1: Schematic diagrams of the (a) Durelli, (b) arch, and (c) gapped-arch theta, and (d) C-ring test specimens. The outer ring of each specimen is diametrally compressed with load *P* and displacement *h*, generating a uniaxial tensile stress state in the web segment in (a) and (b), tension across the gap of an attached nanomaterial in (c), and bending stress state in the central outside region of (d). The diameter of the outer ring is *D* and the width of the web segment is *w*. 19

Figure 2.2: Deep Reactive Ion Etching (DRIE) processes. (a) The Bosch DRIE process produces high-aspect-ratio structures using a repeating sequence of etching and passivation that produce characteristic etch steps known as scallops. (b) The cryogenic DRIE process produces high-aspect-ratio structures using a continuous process of etching

and sidewall passivation that can produce smooth surfaces. 22

Figure 2.3: The wafer layout for each set of second generation samples. Each batch is a single etched wafer. 23

Figure 2.4: Fabrication sequence flow chart. The wafers were first cleaned, and then the front side was processed. Once the front side was done the back side was processed. To complete the fabrication the exposed insulator layer was removed. 25

Figure 2.5: The fabrication sequence for the second generation test samples. The state of the wafer at each step is shown and this corresponds with each step in the flow chart in Figure 2.4. 26

Figure 2.6: (a) Example of the sidewall profile of the photoresist in the batch A processing development prior to the descum process. The photoresist profile had a curvature and typically a footing near the wafer surface (not shown); the location of the typical footing is indicated by the arrow. (b) Another example of the sidewall profile after a one minute descum process. The profile curvature and footing have been removed. ... 30

Figure 2.7: The effect of the HMDS priming method on photolithographic sidewall angles. (a) The poor sidewall angle due to the HMDS liquid spin-prime process. (b) The process in (a) modified with a g-line UV light filter resulting in a better profile. (c) The vapor priming process effect on the original (broadband UV) exposure resulting in a profile consistent with the original photoresist profile in Figure 2.6(a). (d) The vapor priming process effect on the g-line exposure used in (b) resulting in an essentially vertical sidewall. 36

Figure 2.8: Bosch DRIE process modifications. (a) Etch step morphed linearly by 0.5 s over 80 loops produced an inconsistent etch profile resulting is smoothed regions and deteriorated scallops (b) 80 loop etch process modified by performing it in sets of 20 loops resulting in consistent scallop pitches. 40

Figure 2.9: Photoresist behavior during the cryogenic DRIE processing. (a) The resist maintains its single layer state. (b) For the same type of feature as (a) the photoresist cracks and delaminates from the surface prior to or during the etch process. Two specific conditions caused this resist damage to occur: When the resist thickness was greater than 1.3 μm and when the wafer is thermally shocked, changing from room temperature to −110 °C quickly. 42

Figure 2.10: Etch profile results during the early stages of the cryogenic DRIE process development. (a) Plasma did not fully ignite resulting in a very slow etch rate over 15 minutes. (b) Very low O_2 concentration resulting in isotropic etching (and curling of the unattached photoresist). (c) Low-temperature (−130 °C) produced near-crystallographic etching of the silicon (note the pyramid-like micro-masked structures on the left horizontal surface). (d) Oxide masking (between photoresist and silicon) produced inconsistent etch profiles resulting from the insulator layer effect on the wafer conductivity. (e) Low bias power did not direct the etching radicals downward resulting

in side wall etching. 44

Figure 2.11: Etch profile results during the cryogenic DRIE process development approaching the optimal conditions. (a) Low bias power and low O_2 concentration resulted in a negative sidewall taper and footing. (b) Low ICP power and high bias resulted in a higher bias voltage potential and a profile that was near vertical with a footing. (c) High O_2 concentration resulted in a positive sidewall taper. (d) Low O_2 concentration produced a negative sidewall taper. All etch profiles are from 10 min process runs.. 45

Figure 2.12: Feature size dependent etch profile behavior in the cryogenic DRIE process. Different feature sizes result in different side wall profiles and etch rates. For the example case shown, in (a) the 10 μm wide feature has a positively tapered etch profile and etch depth of about 28 μm, while in (b) the 50 μm wide feature on the same etched wafer has a negative profile taper and an etch depth of about 31 μm... 48

Figure 2.13: The cryogenic DRIE process near the silicon-photoresist edge. (a) The edge of the photoresist layer etched away faster than the rest of the photoresist and consequently revealed new silicon that began etching at the top of the etch profile during the deep etch process. (b) By adding a thermally-oxidized silicon dioxide layer between the silicon and photoresist, this effect was greatly decreased... 49

Figure 2.14: Optimized profiles of the (a) Bosch and (b) cryogenic DRIE process. The etched sidewall profiles are vertical... 52

Figure 2.15: Examples of resulting samples for the first fabrication run prior to the oxide removal. The 2-μm oxide layer attached to and around the sample is gray. The black area at the top of the samples is area where the oxide layer has broken out of the wafer. (a) An arch theta sample with smooth edges. (b) An arch theta sample with rough edges and reduced web width dimension. 54

Figure 2.16: Fragment of a sample from the batch A wafer that shows the etch results of the fabrication sequence.. 55

Figure 2.17: The four specimen designs as they appear on the first mask of the second generation specimens: (a) Durelli, (b) arch, (c) gapped-arch, and (d) C-ring. 56

Figure 2.18: Updated mask design for each of the specimen types featured in Figure 2.17: (a) Durelli, (b) arch, (c) gapped-arch, and (d) C-ring. These designs include sacrificial island structures to fill spaces inside and around important structures on samples. This keeps the load constant around these areas and decreases the likelihood of cracks forming in the oxide during the back side etch step. 58

Figure 2.19: PECVD silicon dioxide coating on SOI wafer and fabrication results (a) The PECVD silicon dioxide produces a conformal coating covering the scalloped surface from the front side etch. (b) A more magnified view of the same result showing that the silicon dioxide layer is conformal at the device layer and buried oxide interface of the

SOI wafer. (c) The front side surface after using this process as a front side protective layer; clearly, this oxide was unable to protect the front side etch from the unintended etching when the oxide cracks. The view is of a theta web region at an oblique angle on the side that was adjoined to the buried oxide layer of the SOI. 60

Figure 2.20: Spin coating front side protection results. (a) The photoresist is thin in areas and does not fill in the etched features. (b) Some pitting-like damage observed when this process is used.. 61

Figure 2.21: The spray coating effect on the oxide layer damage problem during the back side etch. (a) No cracking observed around or above the samples. (b) Cracking of the oxide is present though no oxide broke out from the layer... 63

Figure 2.22: Field-emission scanning electron microscopy (FESEM) images of completed (a) Durelli and (b) arch theta test samples. 64

Figure 2.23: (a) Relative size comparison of the first generation (top) and second generation (bottom) test strips. (b) Second generation sample test strip next to a standard razor blade. (c) Oblique view of the second generation sample test strip. 65

Figure 2.24: FESEM images of the through-the-web cross-section of resulting (a) first, (b) second, and (c) third batches of second generation samples. In (a) and (b) the cross-sections of the Bosch DRIE samples maintain a constant thickness. In (c) the sample front is the top of the image. The narrowing at the back of the cryogenic DRIE sample is due to the SOI notching effect).. 66

Figure 2.25: FESEM images of the sidewall etch surfaces for the theta test samples. A portion of the important web segment is indicated by the box in the tilted theta sample of (a). In (b), the sidewalls have regular etch features, known as “scallops”, which are expected with the DRIE process. In (c), the sidewalls have irregular etch features, denoted here as “pits”, which result from unwanted etching of the Si device layer during the etching of the Si handle wafer... 68

Figure 2.26: FESEM image of the etch surface of the web region (tilted) for a (a) second batch of Bosch DRIE sample and (b) a cryogenic DRIE batch sample. The front of the samples is toward the bottom of the images. 69

Figure 2.27: (a) The sample mounting puck for the second generation samples. The samples go into the top slot of the puck and clamped by a pusher plate. (b) The mounting puck installed into an instrumented indenter stage. (c) The 500-μm diameter sapphire spherical indenter used for testing samples. (d) The camera view of the test sample load-point selection. (Inset) Five-indentation cross-pattern used to calibrate the indentation tip to the microscope. The cross-pattern is about 100 μm across. 71

Figure 3.1: AFM images and line-scans of sidewall etch surfaces of the batch A of second generation with (a) scallops and (b) pits. The maximum perturbations along the length of

the scallops and pits are denoted by dashed lines in the respective line-scans. 75

Figure 3.2: AFM scan and power spectral density plot of the (a) round and (b) hexagonal first generation theta samples. The expected scallop wavelength location on the power spectrum is indicated by the arrow and is good agreement with the peaks present in the power spectrum. 80

Figure 3.3: AFM scan and power spectral density plot for the generation II batch A samples: (a) scallops, (b) pitting etch. The expected scallop wavelength location on the power spectrum is indicated by the arrow in (a) and is good agreement with the peaks present in the power spectrum. 81

Figure 3.4: AFM scan and corresponding two-dimensional power spectral density plot of the second generation B batch theta samples. The expected scallop wavelength location on the power spectrum is indicated by the arrow and is good agreement with the peaks present in the power spectrum. 82

Figure 3.5: AFM scan and corresponding two-dimensional power spectral density plot of the second generation C batch theta samples. These samples were etched with cryogenic DRIE where (a) features a region similar to the anticipated surface roughness with a smooth region and some dimpling damage, and (b) includes a significantly larger damaged sidewall structure on the etched surface that will be discussed in Ch 7. 83

Figure 3.6: A simple diagram of a "self-similar fractal"-like surface resulting from the Bosch DRIE process. The scallop pitch, shown in black, is set by the particular Bosch DRIE recipe used to etch the surface. The result of a nearly self-similar fractal-like surface, shown in red (and at a much larger scale than it would actually exist), is due to the nature of the isotropic etching step in the BOSCH DRIE process. 86

Figure 3.7: (a) Grayscale optical image of an arch theta test sample. An optical image of each sample was imported into an image processing routine prior to testing. (b) Vertical line scans of the pixel intensity were analyzed using a full-width half-maximum (FWHM) criteria to determine the web width. The web widths from these line scans were averaged over the entire web segment, resulting in sub-pixel resolution for *w*. 88

Figure 3.8: Histograms of the web width distribution for Durelli and arch theta samples at 0.5 μm intervals. 89

Figure 4.1: The boundary conditions applied to each sample modeled with FEA. The samples have fixed boundary conditions placed on the bottom block beneath the sample to represent the test strip material to which each sample was fixed. The global coordinate system is indicated on the left with the sample thickness in the *z*-direction. The indenter is constrained to load along the *y*-direction indicated by the orange attachments along the circumference of the hemisphere cross-section. Material orientation properties were assigned with a 45° rotation of the global coordinate system in the *x*-*y* plane using the diagonal yellow dash lines to make the length of the web segment along <110>. 94

Figure 4.2: Maximum principal stress distribution for the (a) Durelli and (b) arch theta test specimens subjected to loading with a sapphire sphere. The largest maximum principal stress, σ_{max}, occurs in the web segment, and the largest secondary stress, σ_{sec}, is located at the top and bottom of the inner theta region. For the Durelli theta, the stress ratio $\sigma_{sec}/\sigma_{max}$ = 0.65. For the arch theta, the stress ratio $\sigma_{sec}/\sigma_{max}$ = 0.62. Thus, for both geometries, initial fracture is expected to occur in the web segment. 95

Figure 4.3: Stress concentration in the ends of the web region of the maximum principal stress for each theta specimen geometry. (a) Durelli stress concentration is about 3 % greater than the stress in the web. (b) Arch stress concentration is about 2 % greater than the stress in the web. 97

Figure 4.4: (a) Stress, (b) strain, and (c) load-displacement behavior remained linear at loads up to 2 N. A solid line is drawn through the arch theta data to illustrate the linearity of the data. 99

Figure 4.5: (a) Stress (b) strain, and (c) load-displacement behavior for each of the web width simulated for the Durelli (left) and arch (right) theta specimens. Each sample set is linear and slopes from linear fits to these data were used to generate the interpolation equations, Eqs. (4.8) to (4.13). 102

Figure 4.6: (a) Compliance, (b) stress, and (c) strain *K*-factor plots as functions of inverse web width and corresponding linear fit lines. 104

Figure 4.7: Maximum principal stress for the C-ring specimen under ideal and off-center loading. In (a) the ideal load condition is applied at the center point of the tophat as indicated in the inset. The off-center loading conditions used a load-point applied 20 μm to the (b) left and (c) right of the center point as indicated in the insets. The stress scales are normalized to the max stress in (a), the ideal loading case. 105

Figure 4.8: The C-ring simulation at the step just prior to contact between the faces of the 40 μm C-ring opening at a simulated load of 20 mN. 108

Figure 4.9: The gapped-arch theta specimen. The maximum stress is seen in the region designated as the secondary stress region for the Durelli and arch theta....................... 109

Figure 5.1: *P-h* data for the first unloading segment of 5 different cyclically loaded (a) Durelli and (b) arch theta test samples with a 4 μm to 8 μm distribution of web widths. As w decreases, the compliance, λ, of the theta test specimen increases, illustrated by the changing slope of the data sets. Best fits to all the responses generated compliance values that were all slightly greater than the compliance values predicted from the FEA due to test system deformation compliance. 112

Figure 5.2: *P–h* and corresponding σ–ε data for (a) Durelli and (b) arch theta test samples subjected to five load-unload cycles with a maximum load of roughly one-fifth the typical fracture load. The traces are linear with no discernable hysteresis, which suggests

a secure and stable test platform. E was determined from the slope of the linear portion of the trace. For these particular samples, E = 171 GPa for the Durelli theta and E = 167 GPa for the arch theta. 114

Figure 5.3: Examples of C-ring load-displacement behavior. (a) In this example there is an initial section with a very compliant linear response nearly that of the FEA predicted compliance that transitions gradually to a less compliant linear response. The compliances in the first and second region are λ = 909 nm mN^{-1} and λ = 100 nm mN^{-1}, respectively. (b) In this example there are jumps larger than 1 μm between segments of linear response that maintain nearly the same compliance, λ = 110 nm mN^{-1}, similar to that in the second region of (a). 116

Figure 5.4: Examples of 5-cycle load-displacement behavior for the C-ring specimen. After the initial non-linear region in the first load step, the load-displacement data over the five load-unload cycles exhibits a slight hysteresis that results in a progressive shift in displacement. The initial load segments in (a) and (b) corresponds to the load-displacement behavior highlighted in Figure 5.3(a) and (b), respectively. 118

Figure 5.5: P-h and corresponding σ–ε data of a gapped-arch theta sample for the cyclic loading segment of the test. After an initial non-linear loading segment the five cycle data is linear with negligible hysteresis and a compliance of λ = 9.23 nm mN^{-1} and corresponding elastic modulus of E = 162 GPa. 121

Figure 6.1: Strength comparison of the first batch (batch A) of second generation Durelli thetas to the first generation Durelli thetas. The improvement in test strip design and testing methodology is evident from the increased strengths of specimens. Some strength increase was expected due the decrease in sample size but the adverse effects of the unintended etching process should have affected some samples to have significantly decreased strengths. Even with these considerations, only a small overlap is seen for the strengths of the batch A Durelli thetas compared to the statistical distributions reported for the first generation Durelli thetas [Quinn *et al.*, 2005]. 127

Figure 6.2: P-h and σ–ε data for (a) Durelli and (b) arch theta test samples loaded to failure. E was determined from the slope of the linear portion of the trace, and σ_f was the stress at which fracture occurred. For these particular samples, E was 169 GPa and 166 GPa and σ_f was 2.32 GPa and 2.29 GPa for the Durelli theta and arch theta, respectively. 128

Figure 6.3: (a) Fracture strength as a function of web width. The data can be divided into two groups associated with the sample surface morphology as determined by the etching process as indicated by the dashed line at w = 7.5 μm. For w < 7.5 μm, σ_f varied from 0.8 GPa to 1.9 GPa. For w > 7.5 μm, σ_f varied from 1.4 GPa to 2.7 GPa. The smaller web width samples had greater web width standard deviations indicated by the data error bars. (b) The total strength distribution for the combined Durelli and arch theta test samples is bimodal, as there appear to be three inflection points in the distribution. (c) Weibull failure probability plots for the two distributions in (b) split at w = 7.5 μm. For w > 7.5

μm, m, σ_θ, and σ_{th} were 4.57, 0.90 GPa, and 1.32 GPa, respectively. For w < 7.5 μm, m, σ_θ, and σ_{th} were 2.00, 0.46 GPa, and 0.82 GPa, respectively. In (a) to (c), the grey bands indicate the overlap of the strength distributions.. 130

Figure 6.4: The strength of samples from the (a) second and third batch and (b) all three batches of second generation as a function of the sample web width. In (a), the second (blue) and third (orange) batches both have a single, relatively narrow, grouping of web widths centered at approximately 7.0 μm. The web width standard deviations, indicated by the horizontal bars on each data point, appear larger in the third batch of samples. In (b) the data in (a) is superposed on a graph with the data from the first batch of samples (green). [The data for the first batch was first presented in Figure 6.3(a)]. The fabrication improvements made in the second and third batches are clearly evident by the tighter distribution in web widths, reduced overall web width standard deviations, and sample strengths. 133

Figure 6.5: The strength distributions and three-parameter Weibull fits resulting from the three batches of theta samples. The pitting etch and small scallops correspond to batch A, the large scallops to batch B, and cryo to batch C. 134

Figure 6.6: The break loading segment of the same gapped-arch theta sample in Fig. 5.5. This segment is linear with a corresponding elastic modulus of E = 162 GPa and a strength of σ_f = 1.77 GPa 137

Figure 6.7: The gapped theta strength distribution and three-parameter Weibull distribution fit for the 24 tested samples. Sample strengths ranged from 1.0 GPa to 2.5 GPa. The three-parameter Weibull fit produces values of 4.9, 1.1 GPa, and 0.8 GPa for m, σ_θ, and σ_{th}, respectively. 138

Figure 6.8: Gapped-arch theta equivalent area calculation. (a) The calculated equivalent area for the gapped-arch theta is represented by the red arches that trace across a portion of the internal arches of the sample. (b) Gapped FEA showing the maximum principle stress, tilted to observe the bottom highest stress region. 142

Figure 6.9: An example load-displacement data for a C-ring loaded to fracture. The compliance of this sample was λ = 99 nm mN^{-1} and the FEA translated strength is σ_f = 4.71 GPa. 143

Figure 6.10: All tested C-ring break data and corresponding strengths. The C-rings load and displacement at failure have a linear trend and fitting the data to a line through the origin produces an approximate overall compliance λ_C = 118 nm mN^{-1} for all tested samples. The C-ring tests displayed strengths, based on Eq. (4.15), of between 3.3 GPa and 8.7 GPa. 145

Figure 7.1: (a) Crack-scale features of the fracture surface. Fracture initiation is indicated by the fracture mirror, a smooth region surrounded by cathedral arc lines. Typically, the fracture will deflect onto a preferred cleavage plane. Hackle lines radiate from the

fracture origin. (b) Specimen-scale features of the fracture surface. The crack initiates at a surface flaw, propagates perpendicular to the tensile loading, and then bifurcates or branches. For crystalline materials, this occurs along preferred cleavage planes. 149

Figure 7.2: Fractography was performed by placing sample fragments between grid spaces on a TEM grid that is attached to a SEM stub. Many sample fragments have been attached in this image.. 151

Figure 7.3: (a) Schematic diagram of the {111} and {110} fracture planes that occur in the specimen web segment. (b) and (c) FESEM images of web segment fracture surfaces for the scallop and pit samples, respectively. In both examples fracture initiated on {110} fracture planes and changed to {111} fracture planes once the arc-ribs around the fracture mirror were generated. The mirror location and corresponding origin location is indicated by the arrow; in both (b) and (c), fracture initiated at a sidewall etch feature. Cleavage step hackle radiates from the fracture mirror and origin. The size of the fracture mirror in the scallop-etch example in (b) is clearly smaller than the mirror in the pit-etch example in (c). 152

Figure 7.4: (a) An example batch B arch theta fracture surface and origin. Fracture occurred at the surface centered about a pair of flaws (bottom), initiated on {110}, and the fracture deflected onto {111} directly after cathedral arcs were formed (top). (b) An example batch C arch theta fracture surface and origin. Fracture was similar to (a). Fracture occurred at the surface due to a large etching defect (bottom), initiated on {110}, and the fracture deflected onto {111} directly after cathedral arcs were formed (top). . 154

Figure 7.5: Schematic diagrams of (a) a sharp crack on a planar surface and (b) a short sharp crack at the root of a semi-elliptical notch that is more representative of failure-causing flaws on rough etched surfaces. 157

Figure 7.6: Example of a batch B C-ring fracture. (a) The C-ring fracture occurred above the central high stress region located along the C-ring center line. (b) Straight-on view of the fracture face for the C-ring indicated by the box in (a). Fracture face shows cantilever curl at the bottom of the fracture face indicating that the C-ring had flexural load acting on it at fracture. (c) Fracture initiation location in the region of (b) indicated by the white box. The fracture initiated near the back edge of the C-ring near the thin layer of extra material jutting out from the sample. This material is an artifact of sample fabrication. 160

Chapter 1: Background and Introduction

1.1 The Promise of Micro-Electro-Mechanical Systems (MEMS)

Many advanced materials are intended for use in small scale applications, for example, microelectronics [Gambino and Colgan, 1998; Kim, 2003; Wallace and Wilk, 2003], microelectromechanical systems (MEMS) [Spearing, 2000; Madou, 2002], photonics [Soref, 1993; Fan *et al.*, 2009; Yan *et al.*, 2009], biotechnology [Fan *et al.*, 2009], and magnetic storage [Parkin *et al.*, 2003; Fan *et al.*, 2009; Slaughter, 2009; Gulyaev *et al.*, 2010]. MEMS are microscale devices that are electromechanical in operation: Devices that are mechanically deformed through an electrical control path are actuators; Devices that produce an electrical response on mechanical deformation are sensors. MEMS are typically fabricated using lithographic and etching techniques originally developed for the microelectronics industry and commonly made out of brittle materials, especially silicon. The great potential for MEMS is in devices that can perform significant mechanical work. Such work can be performed by MEMS that incorporate large-load components, such as thermal and piezoelectric actuators [Bell *et al.*, 2005], or that include contacting and moving components, such as electrical contacts in microswitches, hinges in microactuators, and gear teeth in micromotors [Kovacs, 1998].

Figure 1.1 highlights a number of promising MEMS devices and organizes them by the device mechanical behavior and component interactions during operation. Type 0 devices have components that have negligible operational movement compared to component size and the primary example for this type is the inkjet printer head [Le, 1998]. Type 1 devices contain moving components without contacting interactions. These

Type 0 *No Moving Components*	**Type 1** *Moving Components*	**Type 2** *Contacting Components*	**Type 3** *Contacting and Rubbing Components*
For example, see Le, H. *JIST*, 1998.	For example, see Bernstein, J. *et al.* *IEEE MEMS*, 1993.	For example, see Dudley, D. *et al.* *Proc. SPIE*, 2003.	For example, see Flater, E. *et al.* *Wear*, 2006.
Inkjet heads	Accelerometers Gyroscopes Resonators Pressure Sensors	DMD Relays Valves Pumps	Optical Switches Scanners Locks Discriminators

*Designed after Romig, A *et al. Acta Mat.* 2003.

Figure 1.1: Types of MEMS devices based on the device component feature interactions during operation [Bernstein *et al.*, 1993; Le, 1998; Dudley *et al.*, 2003; Romig *et al.*, 2003; Flater *et al.*, 2006]. DMD: Digital micromirror device.

types of MEMS include accelerometers, gyroscopes [Bernstein *et al.*, 1993], resonators, and pressure sensors with many of these devices used in everyday applications, such as vehicle sensors, video game systems, and cell phones. Type 2 MEMS devices have contacting and moving components and these include relays, valves, pumps, and the digital micromirror device (DMD) (by Texas Instruments) [Dudley *et al.*, 2003]. The most complex type of MEMS, Type 3, have contacting and rubbing components and includes devices such as optical switches, locks, gear discriminators, and the inch-worm 'nanotractor' [Flater *et al.*, 2006].

Currently, only a few of the devices featured in Figure 1.1 are commercially successful. These successful devices are limited primarily to the first two types, with a single successful Type 2 device. The remaining MEMS lack reliability, meaning the devices have a very low probability of performing the intended design function effectively for a desired operational lifetime. The one successful Type 2 device is the DMD, which is used in high brightness displays such as projectors and televisions. (The DMD design has three aspects that allow it to operate reliably: The contacting surface area is minimized, the device is coated with a self-healing self-assembled lubricating monolayer, and the device is hermetically sealed [Van Kessel *et al.*, 1998].) Each of the successful MEMS devices have revolutionized and replaced the previous method of providing their particular functions, such as MEMS accelerometers replacing ball-and-shaft vehicle air bag sensors; they have been integrated into everyday life in many ways. This is only a fraction of the potential of MEMS, with many Type 2 and 3 devices that cannot yet be made to be operationally reliable.

Type 2 and 3 devices cannot be made reliable because the adhesion and friction effects of the contacting and rubbing components are difficult to assess. A possible consequence of the large loads and the frictional effects during device operation is that stress generated in a component exceeds the component strength, leading to component failure and thus truncated lifetime and uncertain device reliability. Careful fabrication procedures can lead to increased component strength (*e.g.,* the strength of single-crystal silicon structures and devices has been shown to reach values as great as 18 GPa [Namazu *et al.*, 2000]), but the distribution of strength values over component sample populations is usually extremely broad [Jadaan *et al.*, 2003], and the stress ranges experienced in MEMS devices in use are likely to vary greatly.

Thus, MEMS device reliability is difficult to predict, and, as a result, the number of MEMS devices that demonstrate significant mechanical work is still limited. In order to optimize manufacturing yield and operational performance, especially reliability [van Spengen, 2003], all materials and devices must maintain mechanical integrity; these devices must be designed to withstand the largest locking stress that friction and adhesion effects cause. To enable this, the development or optimization of particular device materials and components, and their processing methods, thus requires measurements of structure and properties at small scales. A pervasive measurement requirement is that of measuring mechanical properties, and relating them to processing and structure: A mechanical test structure capable of assessing the effects of the processing techniques on device material mechanical behavior is thus required and a statistically meaningful number of tests are necessary for precision assessment. A robust strength measurement technique and test structure developed for the micro-scale will enable development of the

processing-structure-properties relationships that are crucial for the optimization of MEMS device materials and components.

In addition, the development of such a robust micro-scale strength measurement technique for MEMS materials and processing should be extendable to other materials and processing such as for materials development in which the materials may be available only in small volumes.

1.2 *Strength Testing Methodologies*

Establishing processing-structure-mechanical properties linkages at small scales is difficult [Lord *et al.*, 2010]: Not only are the involved loads and displacements small, making measurement difficult, but issues of specimen gripping and loading alignment, which are also often problematic at large scales [Durelli *et al.*, 1962], are made more difficult as well. In addition, post-test sample collection and manipulation are difficult, which impedes the ability to identify property-limiting structural defects during failure analysis and thus hinders the capacity to alter processing procedures for property optimization.

The ability to assess the effects of processing variations on strength is a crucial aspect of a strength testing methodology. Such processing-strength variations are highlighted in Figure 1.2, which shows a graph of measured fracture strength of single-crystal silicon (Si) as a function of the approximate stressed area for many sample and loading geometries (uniaxial and equibiaxial tension and bending) and surface processing

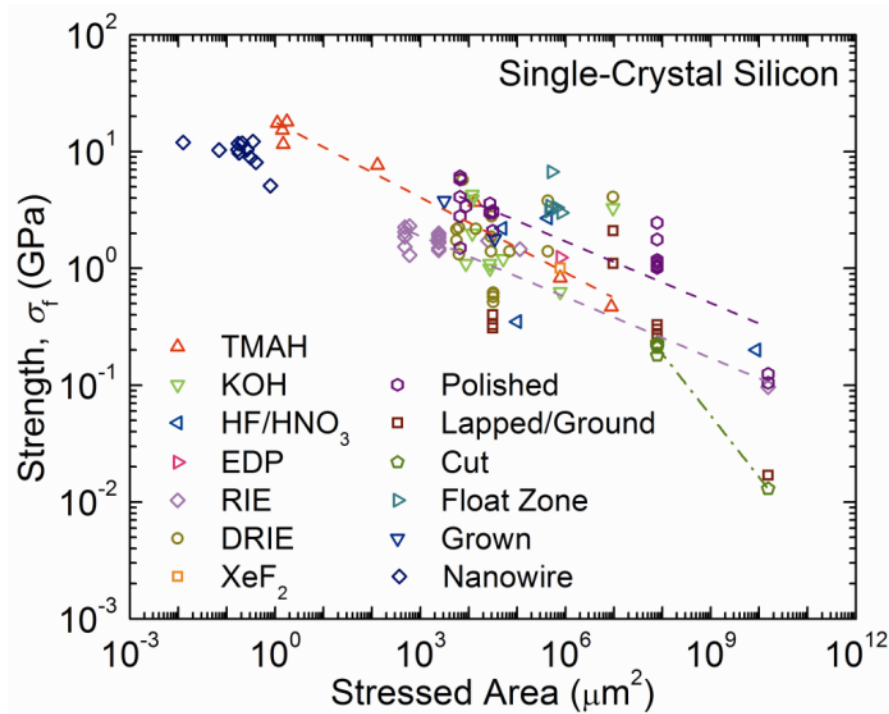

Figure 1.2: Fracture strength as a function of approximate stressed area for single-crystal silicon for a variety of fabrication methods. Data were collected from a large number of sources [Eisner, 1955; Pearson *et al.*, 1957; Sylwestrowicz, 1962; Hu, 1982; McLaughlin and Willoughby, 1987; Johansson *et al.*, 1988; Ericson and Schweitz, 1990; Vedde and Gravesen, 1996; Wilson and Beck, 1996; Wilson *et al.*, 1996; Schweitz and Ericson, 1999; Suwito *et al.*, 1999; Chen *et al.*, 2000; Namazu *et al.*, 2000; Yi *et al.*, 2000; Chen *et al.*, 2002; Sundararajan *et al.*, 2002; Jeong *et al.*, 2004; Quinn *et al.*, 2005; Tsuchiya *et al.*, 2005; Hoffmann *et al.*, 2006; Isono *et al.*, 2006; Nakao *et al.*, 2006; Miller *et al.*, 2007; Zhu *et al.*, 2009; Banks-Sills *et al.*, 2011]. Power law trend lines are shown to highlight the overall behavior of the strength data. TMAH: Tetramethylammonium hydroxide; EDP: Ethylenediamine pyrocatechol; RIE: Reactive ion etching; DRIE: Deep reactive ion etching.

methods sources [Eisner, 1955; Pearson *et al.*, 1957; Sylwestrowicz, 1962; Hu, 1982; McLaughlin and Willoughby, 1987; Johansson *et al.*, 1988; Ericson and Schweitz, 1990; Vedde and Gravesen, 1996; Wilson and Beck, 1996; Wilson *et al.*, 1996; Schweitz and Ericson, 1999; Suwito *et al.*, 1999; Chen *et al.*, 2000; Namazu *et al.*, 2000; Yi *et al.*, 2000; Chen *et al.*, 2002; Sundararajan *et al.*, 2002; Jeong *et al.*, 2004; Quinn *et al.*, 2005; Tsuchiya *et al.*, 2005; Hoffmann *et al.*, 2006; Isono *et al.*, 2006; Nakao *et al.*, 2006; Miller *et al.*, 2007; Zhu *et al.*, 2009; Banks-Sills *et al.*, 2011]. Two clear trends are apparent in Figure 1.2: (1) Fracture strengths tend to decrease with increased stressed area, independent of processing method. This is consistent with the engineering principle [Ashby, 1999] that fabrication methods tend to scale surface roughness, and therefore strength-limiting defect sizes, with component size; (2) Fracture strengths tend to decrease with increased stressed area, with different dependencies for different processing methods. This is consistent with the physics principle [Davidge, 1979] that processing methods tend to generate a particular distribution of flaw potency, and that the probability of a component containing a more potent defect increases with component size. The dashed lines on Figure 1.2 indicate trend (2) for selected fabrication methods. An implication of Figure 1.2 is that if processing method and stressed area are invariant, then strength should not be altered by sample or component geometry.

Test structures to measure the strength of MEMS materials and components that could be used to optimize fabrication processes include tensile bars [Sharpe *et al.*, 1997; Suwito *et al.*, 1999; Boyce *et al.*, 2008], fixed–free beams [Ericson and Schweitz, 1990], fixed–fixed beams [Namazu *et al.*, 2000], and biaxial flexure plates [Chen *et al.*, 2000]. Test specimens that have enabled statistically meaningful numbers of small-scale tensile

strength measurements have often employed complex geometries microfabricated from multilayer polycrystalline material; these include pull tabs [Bagdahn *et al.*, 2003; Boyce *et al.*, 2007; Miller *et al.*, 2007] and chains of links [Boyce, 2010] for which specialized mechanical loading systems were required and on-chip tensile bars for which electrical connection was required for thermal actuation of the tests [Hazra *et al.*, 2009; 2011]. Simpler geometries microfabricated from single layer silicon-on-insulator (SOI) material have also been demonstrated: In one case, large numbers of samples in the form of beams were tested, using loading by an atomic force microscope (AFM) [Namazu *et al.*, 2000]; in another, a tensile dog-bone geometry was demonstrated [Banks-Sills *et al.*, 2011], although the specimen does not lend itself well to testing large numbers of samples and a specialized mechanical loading system is required.

A simple and optimized test specimen design and testing methodology that can be utilized over many materials and processing techniques, and that avoids the loading and misalignment difficulty typically associated with strength testing methodologies, is desirable in order to provide a broad testing methodology useful to the MEMS industry for device assessment, modification, and optimization.

1.3 Theta Specimen Testing Prototype

An experimental method that avoids many of the difficulties in measuring mechanical properties of materials at small scales is instrumented indentation testing (IIT) [Oliver and Pharr, 1992; Field and Swain, 1993; 1995; Mencik *et al.*, 1997; Oliver and Pharr, 2004; Oyen and Cook, 2009]. Commercial IIT instruments are well able to measure loads in the micronewton to 100s of millinewtons range and displacements in the nanometer to

10s of micrometers ranges, enabling small-scale mechanical testing. As the only IIT measurement requirement is the mounting of a large specimen surface, typically millimeters or more in dimension, perpendicular to the axis of a probe loaded into the surface in compression, gripping, alignment, and manipulation difficulties are largely obviated. In addition, examination of the resulting indentations on the large specimen surface is relatively easy, allowing for failure analysis [Anstis *et al.*, 1981; Cook and Pharr, 1990; Bradby *et al.*, 2001; Cook, 2006; Gouldstone *et al.*, 2007]. Elastic modulus, hardness and yield stress, toughness, and viscosity are thus all measurable with IIT [Chantikul *et al.*, 1981; Oliver and Pharr, 1992; Field and Swain, 1993; Oyen and Cook, 2009].

Recently, a new experimental test specimen was introduced [Quinn *et al.*, 2005; Fuller *et al.*, 2007; Gaither *et al.*, 2010] that allows tensile strength of brittle materials to be measured at small scales and which utilizes many of the advantages of IIT: The tensile test specimen deliberately does not attempt to replicate large-scale tensile test specimen geometries with the attendant gripping and alignment difficulties, but instead integrates the “specimen” into a test “frame”. The integrated circular frame and specimen cross-piece, or “web” segment, resemble the Greek letter Θ, and the overall specimen is known as a “theta” specimen [Durelli *et al.*, 1962; Durelli and Parks, 1962; Durelli, 1967]. The specimen is easily tested in compression with an IIT device, resulting in tension in the specimen web segment and thereby avoiding gripping issues. Precision microfabrication techniques can lead to a well-defined alignment of the tensile specimen relative to the loading axis, thereby minimizing alignment issues. Two theta specimens with outer geometry variations were fabricated as shown in Figure 1.3(a) and (b), a round theta

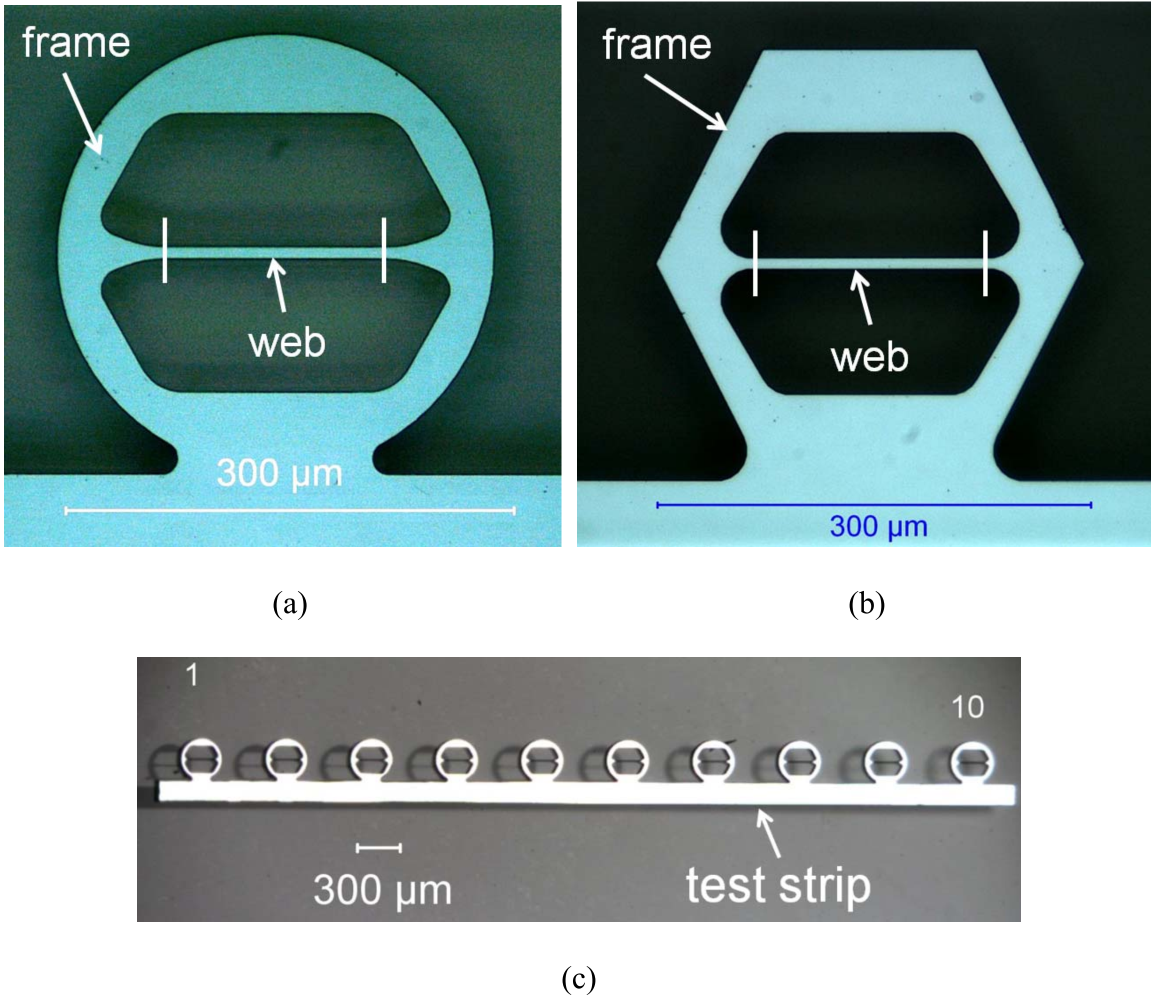

Figure 1.3: The first generation theta test specimen designs. (a) Round and (b) hexagonal theta test samples are 300 μm across, and (c) the test strip includes 10 theta samples. Images from Quinn *et al.* [Quinn *et al.*, 2005].

[Figure 1.3(a)] and a hexagonal theta [Figure 1.3(b)], and each set was fabricated on a 10 sample test strip as shown in Figure 1.3(c). The first generation fabrication sequence utilized a single through-wafer etch step, shown in Figure 1.4. These first generation samples were successfully tested via IIT, sample strengths were determined form the linear load-displacement responses [Quinn *et al.*, 2005], and fracture was observed to occur in the theta web region as expected [Quinn, 2008]. These test specimens and testing results demonstrated the viability of the theta specimen technique for micro-scale strength measurements, but also revealed a number of problems, which will be addressed in the next section.

1.4 Thesis: Theta-based Approach for MEMS Device Assessment and Optimization

My thesis is that the theta specimen is an optimal test structure for use in a commercially viable method for measure strength and optimizing MEMS through the establishment of processing-structure-properties relationships. I propose to demonstrate this through optimizing the overall methodology building on the earlier theta testing demonstration.

The first generation theta specimens presented in the previous section demonstrated as a proof-of-concept that the theta specimen can be used to measure strength at the micro-scale; however clear problems with the test structure and testing methodology were apparent with this first generation. For instance, the use of a single wafer for the sample device layer and single etch step, as shown in Figure 1.4, did not produce controlled etch surface features, nor optimal device dimensions due to side wall taper, a deviation from a 90° sidewall angle.

(a)

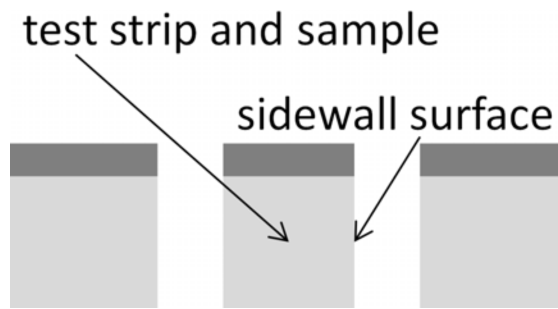

(b)

Figure 1.4: The first generation theta specimen fabrication sequence [Quinn *et al.*, 2005]. (a) Photoresist was spun on to the wafer and photolithographically patterned. (b) The theta samples and test strips were formed simultaneously using a through-wafer DRIE step. The photoresist was removed directly after the through-wafer etching.

The wafer used for the first generation fabrication had to be thin due to the requirement that the test strips and samples were simultaneously fabricated by a through-wafer etch. The sample test strips in Figure 1.3(c) were difficult to handle, manipulate, and mount for testing. The test strip design and the consequent mounting configuration did not produce a secure and stable mounting and testing configuration. The sample strip was difficult to fix in the holder and could move during testing. The test strip was also difficult to seat for testing. In addition, due to the mounting method, the sample was neither capable of being mounted without some tilt nor avoid contact with the surrounding material. This reduced both the ability to load the sample properly and avoid load transfer to the surrounding mount material. The samples were not isolated from one another and fragments from tested samples could potentially interfere with subsequent samples tests. Furthermore, post-test analysis was also difficult due to the test strip design and mounting configuration.

The indenter-to-sample testing interaction was also non-ideal due to the use of a large flat punch indenter tip that had a degree of tilt that inevitably loaded the theta samples primarily at one end rather than the ideal position in the center. The first generation theta geometries in Figure 1.3(a) and (b) were designed after the original Durelli theta design, which was not optimized to minimize secondary stresses. When loaded, the primary stress in the theta samples was across the constant cross-section web region while significant secondary tensile stress was also induced across the internal top and bottom surfaces of the theta samples.

Each of these problems has been addressed in the current research. The second generation theta testing methodology has been optimized by several means. The

mounting and loading configuration has been changed for ease of mounting and testing, loading location control, and sample alignment and isolation. The theta specimen and test strip have been optimized and additional test specimens have been developed to explore this testing methodology for extended applications. The optimized test strip was designed to be much larger and thicker than the samples connected to it as opposed to the strip and samples being of similar size scales for the first generation (see Figure 1.3 and Figure 2.23 later). The sample fabrication has been optimized to provide sample thickness and etch process control. The optimized fabrication approach was amenable to multiple process variations for sample creation and provides an opportunity for extending this methodology to additional materials and processing in the future.

To demonstrate that this theta-specimen testing approach enables the assessment and optimization of MEMS processing and structural designs, a number of sample fabrication runs are developed, performed, and assessed. Figure 1.5 is a diagram designed to illustrate important aspects necessary for developing an understanding of MEMS component behavior that can ultimately lead to improved MEMS reliability. This sort of diagram is often used in the discussion of materials science and engineering aspects of materials and components [Ashby, 1999]. Processing, structure, properties, and performance are all important links in the assessment and optimization of MEMS devices. Images from chapters in this dissertation are included in Figure 1.5 next to the particular associated relationship. Processing-structure relationships are established by analyzing the fabricated sample structures at both sample and surface length scales. Structure-properties relationships are established through the testing and evaluation of the fabricated sample sets. In future work, the demonstration of these developed relationships

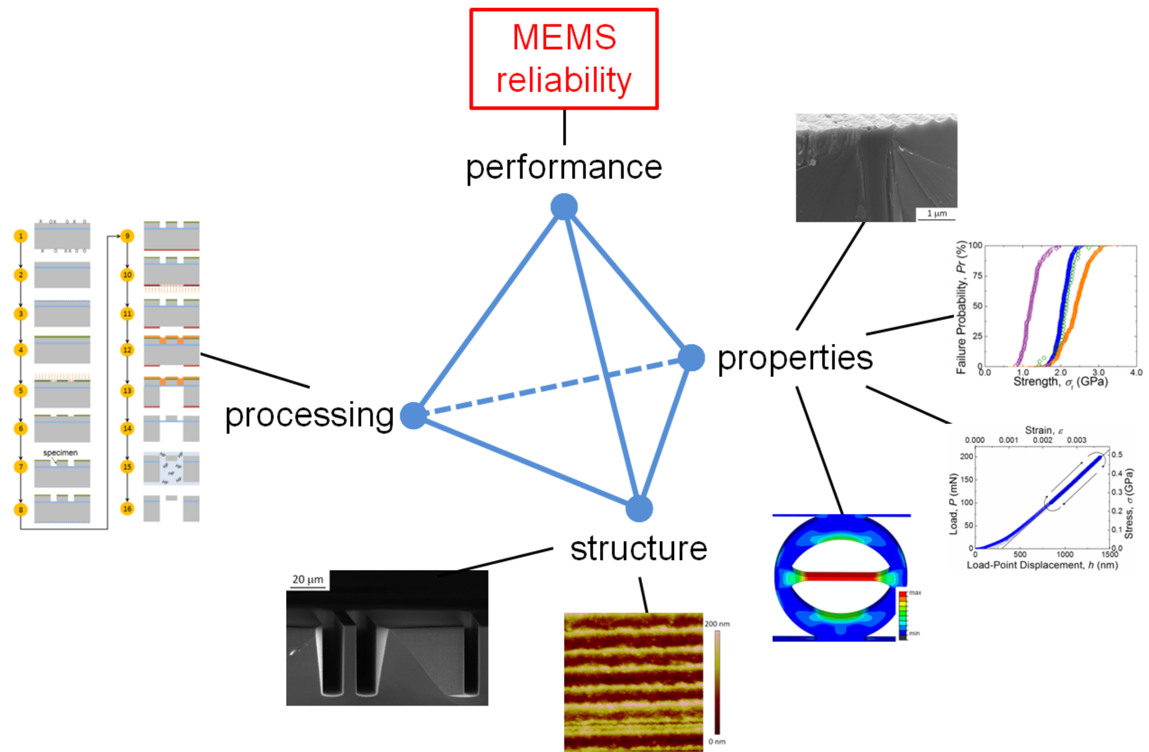

Figure 1.5: The processing-structure-properties-performance relationship for this dissertation with images from each step of the project that will be covered in the following chapters.

with this testing approach can be used to extend this methodology to the determination of properties-performance relationships. The dissertation outline in the next section provides the layout for how I accomplished each portion of this research, the details of which are presented in the following chapters.

1.5 *Dissertation Outline*

This dissertation is organized as follows. In this first chapter the background and motivation of this research is covered. The development of the processing-structure relationships is presented in Chapters 2 and 3. In Chapter 2 the design and fabrication of all test specimens and the experimental testing method is presented. Four specimen types are developed for strength testing using an optimized testing design that allows for simple testing in a conventional instrumented indenter. The resulting etch surface features and sample geometry variations of the fabricated samples are analyzed via AFM and an image processing routine, respectively, in Chapter 3. Statistical data are compared from the AFM analysis of every processing method variation of the fabricated batches of test samples. The image processing routine in Chapter 3 provides the distribution of sample geometry dimension variations for each batch of fabricated test samples.

The development of the structure-property relationships is presented in Chapters 4 to 7. Chapter 4 presents the finite element analysis (FEA) simulations and analysis of the four test specimens. The simulation analyses are used to determine the sample compliance and develop stress and strain relationships as functions of IIT load and load-point displacement, respectively. Several sample geometry dimension variations were

performed in the FEA simulations to account for the fabricated sample variations presented in Chapter 3.

In Chapters 5 to 7 the experimental test results and post-test examination are covered. In Chapter 5 the elastic deformation response of the fabricated samples are compared to the FEA simulated relationships. The comparison between the FEA and experimental results validates the testing methodology for the theta specimen approach. In Chapter 6 the fracture strength behavior of each sample is determined using FEA interpolation equations developed in Chapter 4. Weibull analysis is applied to the strength distributions of each sample set. In Chapter 7 fractography is applied to fracture surfaces of the tested samples to determine the flaws that induced fracture and the way the samples fractured. Fracture mirror size comparisons are made and critical flaw size calculations are compared to the surface roughness measurement made in Chapter 3.

The summary of this research and the usefulness of this testing methodology to small-scale mechanical testing are discussed in Chapter 8. Future paths of investigation are also covered in Chapter 8. Future investigations will focus on the extension of this testing approach to additional materials, to device reliability, and to the MEMS industry.

Chapter 2: Fabrication and Testing Methodology

In this chapter the processing-structure relationship is developed through the optimization of the test specimen designs, fabrication sequence, and the sample etching techniques. The optimizations of the fabrication sequence and sample etching techniques are described in detail. Resulting large-scale surface features for each fabrication run were examined including surface etch quality and sample cross-sections. The IIT methodology for the optimized design is also covered.

2.1 Sample Design

Four small-scale test specimen designs for measuring strength were included in this research project: Two were theta specimens with different internal geometries for tensile strength measurement, a C-ring specimen for bending strength, and a gapped-theta specimen for nanomaterial tensile strength and as an alternative bending strength structure. Figure 2.1 shows schematic diagrams of each test specimen developed for small scale testing. All specimen geometries are formed from a frame with a circular exterior that is attached to a macro-scale strip at the base (not shown, see Figure 2.23 later) similar to the first generation test strip, and include a hat structure at the specimen top. The theta specimens in Figure 2.1(a)-(c) incorporate a web across the center of the specimen with the latter design having a gap in the center of the web. The specimen geometry shown in Figure 2.1(a) is based on the original design by Durelli [Durelli *et al.*, 1962; Durelli and Parks, 1962; Durelli, 1967] and consists of straight sections joined by tangential circular sections to define the frame interior. The specimen geometry shown in

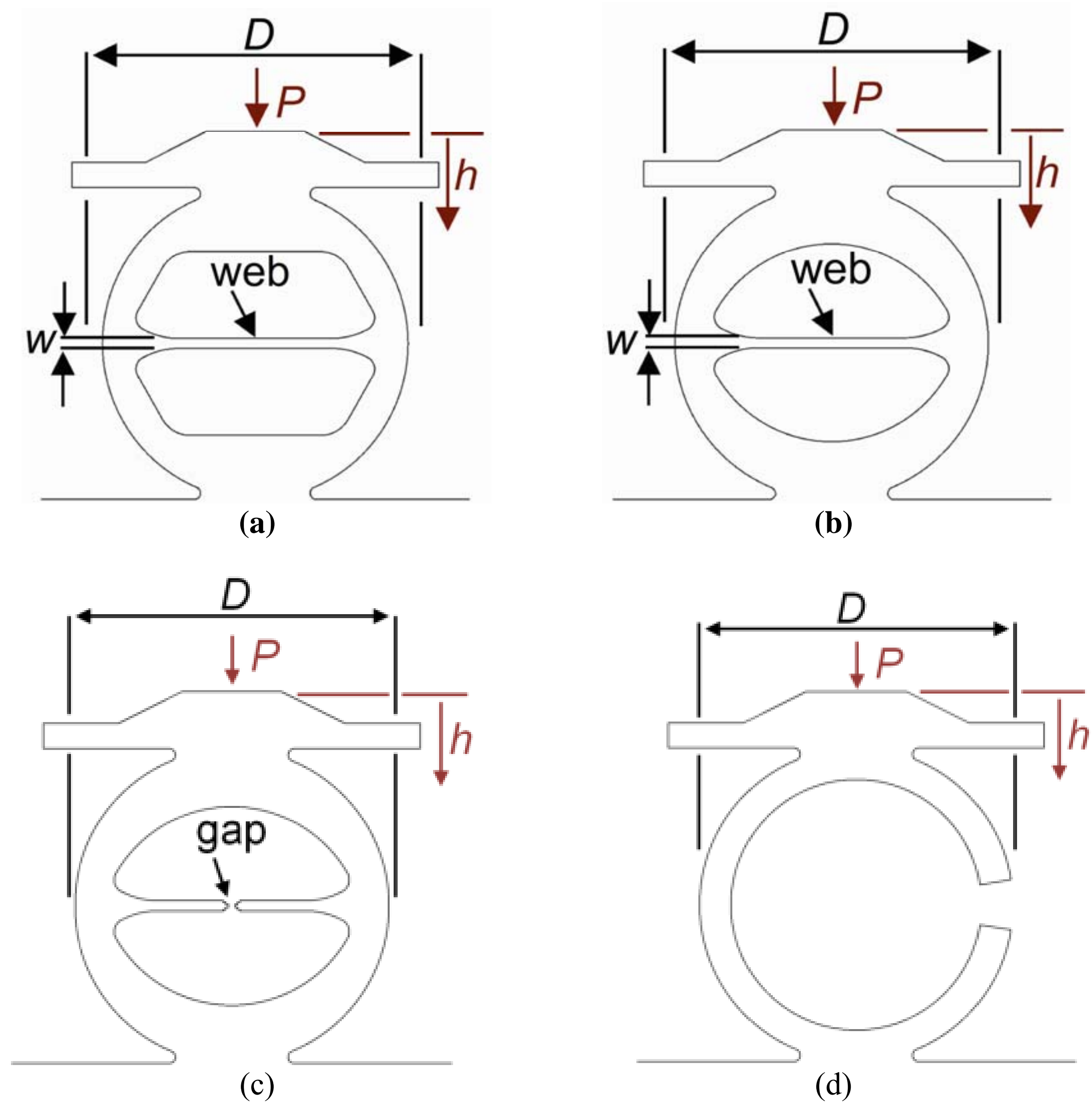

Figure 2.1: Schematic diagrams of the (a) Durelli, (b) arch, and (c) gapped-arch theta, and (d) C-ring test specimens. The outer ring of each specimen is diametrally compressed with load P and displacement h, generating a uniaxial tensile stress state in the web segment in (a) and (b), tension across the gap of an attached nanomaterial in (c), and bending stress state in the central outside region of (d). The diameter of the outer ring is D and the width of the web segment is w.

Figure 2.1(b) is the new arch theta specimen [Gaither *et al.*, 2010], and consists of a single circular arch to define the frame interior.

The theta specimen designs use tangential circular sections to incorporate the web and have the same diameter, *D*, of 250 μm and web width, *w*, of 8 μm. During testing, a load, *P*, is applied to the top surface of the specimen and the load-point displacement, *h*, is measured. Loading the Durelli and arch theta specimens in compression generates a uniform tensile stress across the uniform cross-section of the web. The arch theta design replaces the complex internal geometry of the original Durelli design with an arch, thereby reducing the size and extent of secondary, non-web, stresses in the specimens on loading (see Ch. 4). The top hat structure is included to minimize loading misalignments and stress concentrations [Fuller *et al.*, 2007; Gaither *et al.*, 2010] that also lead to large secondary stresses. Both of these design changes increase the probability that sample failure would initiate, as intended, in the web. The stressed area of the web, in tension, in both designs was approximately 6.25×10^3 μm^2, about the center of the area range of Fig. 1.2.

The gapped-arch theta specimen [Figure 2.1(c)] is designed exactly like the arch theta sample with a 10 μm gap in the center of the web region. The C-ring specimen [Figure 2.1(d)] was included as a micro-scale bend test similar to a conventional bend test. It was designed to be a scaled down version to the ASTM standard C-ring test method [C1323–96, 2001]. The C-ring design includes an inner diameter of 200 μm and an opening of 40 μm on the right side.

2.2 *Deep Reactive Ion Etching (DRIE) Techniques*

Two etching techniques were utilized in the fabrication of multiple batches of samples, both of which are deep reactive ion etching (DRIE) techniques. Figure 2.2 shows how these two DRIE methods can produce high-aspect-ratio structures with vertical sidewalls. For Bosch DRIE in Figure 2.2(a), alternating short steps of SF_6 isotropic etching and C_4F_8 passivation, at ambient temperature, produce an essentially anisotropic etch overall with characteristic etch steps called scallops [Senturia, 2001; Chen *et al.*, 2002]. For cryogenic DRIE in Figure 2.2(b), a continuous process of etching and passivation with SF_6 and O_2, respectively, are used to produce an anisotropic etch overall with characteristic smooth sidewalls [Chekurov *et al.*, 2007]. The cryogenic DRIE process is performed at low temperatures between −130 °C and −90 °C.

Three sample batches were fabricated in this project: Two Bosch DRIE processes, with significantly different scallop pitch sizes, and a single cryogenic DRIE process were used to fabricate the first two and third batch of samples, respectively. Each process was optimized for the second generation sample mask layout in order to produce vertical sidewalls, most importantly in the web region, to produce a constant cross-section tensile test region. The details of the Bosch DRIE processes applied and modified, as well as the development of the applied cryogenic DRIE process, are discussed in a later section.

2.3 *Fabrication*

Each fabrication run was performed on a single wafer and each sample batch was created with a different etching recipe. The sample layout on each wafer is illustrated in Figure 2.3. This layout allowed for hundreds of Durelli and arch thetas and C-rings to be

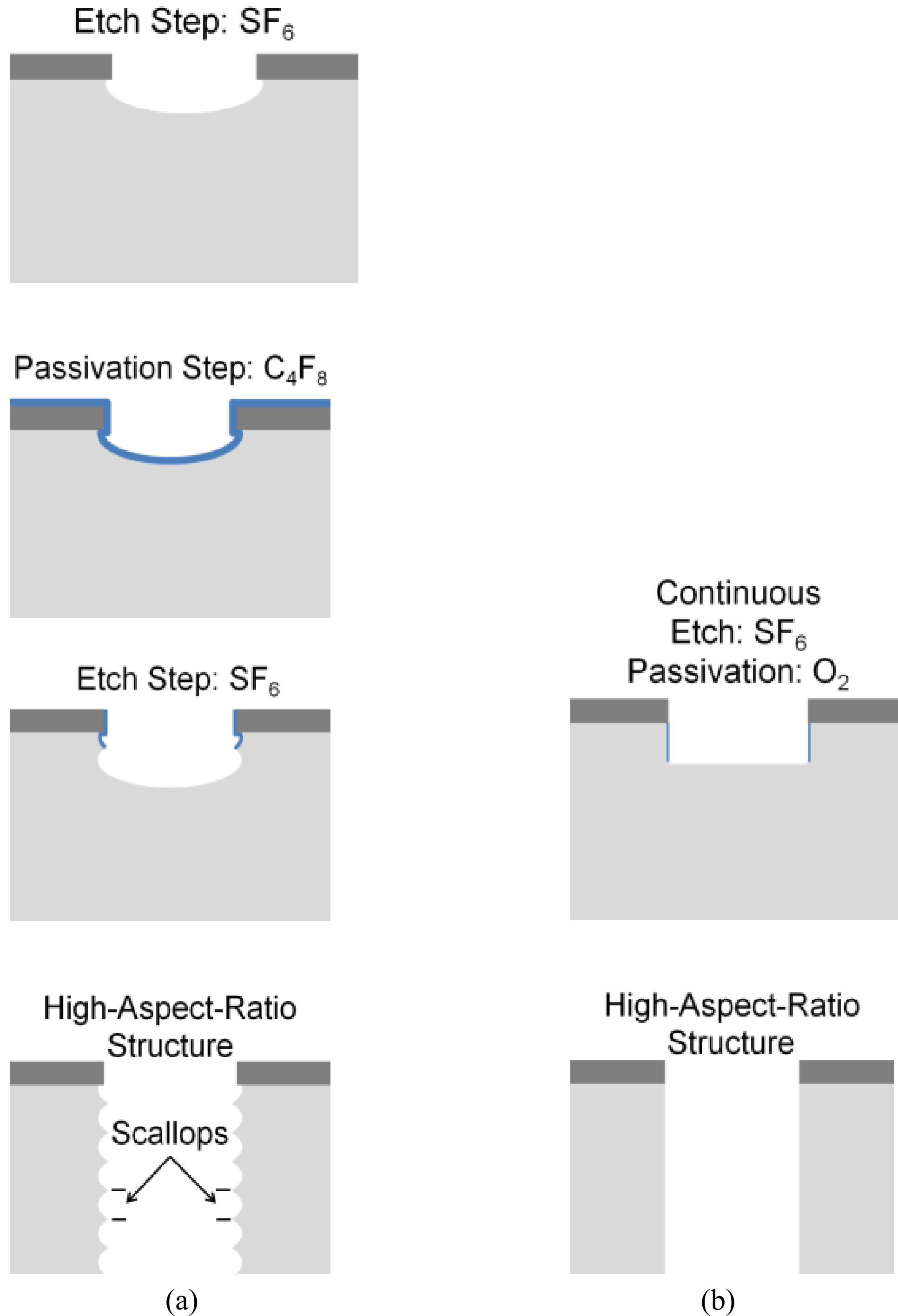

Figure 2.2: Deep Reactive Ion Etching (DRIE) processes. (a) The Bosch DRIE process produces high-aspect-ratio structures using a repeating sequence of etching and passivation that produce characteristic etch steps known as scallops. (b) The cryogenic DRIE process produces high-aspect-ratio structures using a continuous process of etching and sidewall passivation that can produce smooth surfaces.

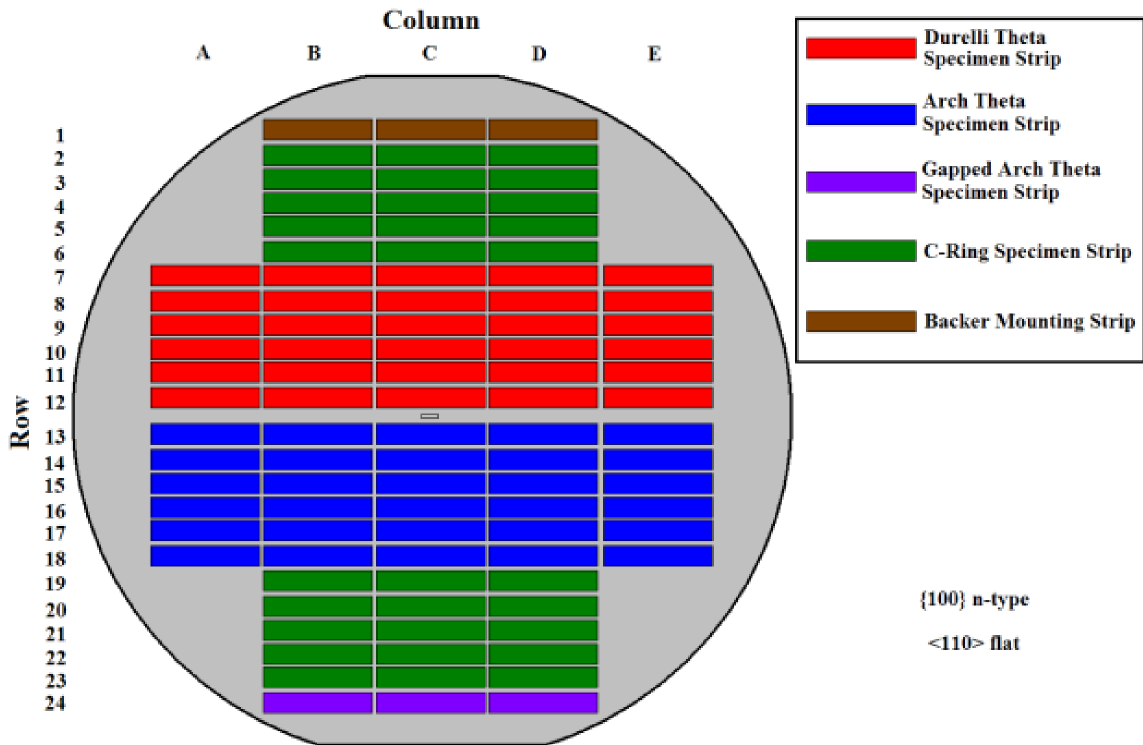

Figure 2.3: The wafer layout for each set of second generation samples. Each batch is a single etched wafer.

fabricated in a single run. The second generation fabrication sequence has been optimized from problems discovered in the first generation of theta specimens and covered in Ch. 1. The fabrication sequence flow chart and schematic diagram for the second generation of test sample sets is shown in Figure 2.4 and Figure 2.5, respectively. The three batches of samples, denoted as batch A, B, and C, were fabricated using the fabrication sequence in Figure 2.4 and Figure 2.5 using a single wafer for each sample batch. All three wafers were 100 mm diameter (001) silicon-on-insulator (SOI) wafers, consisting of three layers: Device, insulator, and handle wafer layers. The single-crystal silicon (Si) device layers were (25.0 ± 0.5) μm thick for the batch A and B wafers, and (25 ± 1) μm for the batch C wafer. The SiO_2 isolation layers were (2.0 ± 0.1) μm thick for the batch A and C wafers, and (1.00 ± 0.05) μm for the batch B wafers. The Si handle wafer layers were (400 ± 10) μm, (400 ± 5) μm, and (480 ± 10) μm thick, for the batch A, B, and C wafers, respectively. The uncertainty values represent variations across the wafer as specified by the manufacturer (Ultrasil Corporation, Hayward, CA). The SOI structure allowed for better control of sample device thickness and more robust strips for manipulation and mounting of samples for testing than with the first generation design [Quinn *et al.*, 2005; Quinn, 2009]. The Si device layer and Si handle wafer layer were patterned by front- and back-side photolithographic masks and etched using DRIE to define the sample and strip structures. After Si etching, the SiO_2 layer was removed with a buffered-oxide etch to create the freestanding samples. The subsections below detail the steps shown in Figure 2.4 and Figure 2.5 for the second generation sample fabrication process. Details of the development of particularly important and sensitive steps will be discussed in a later section.

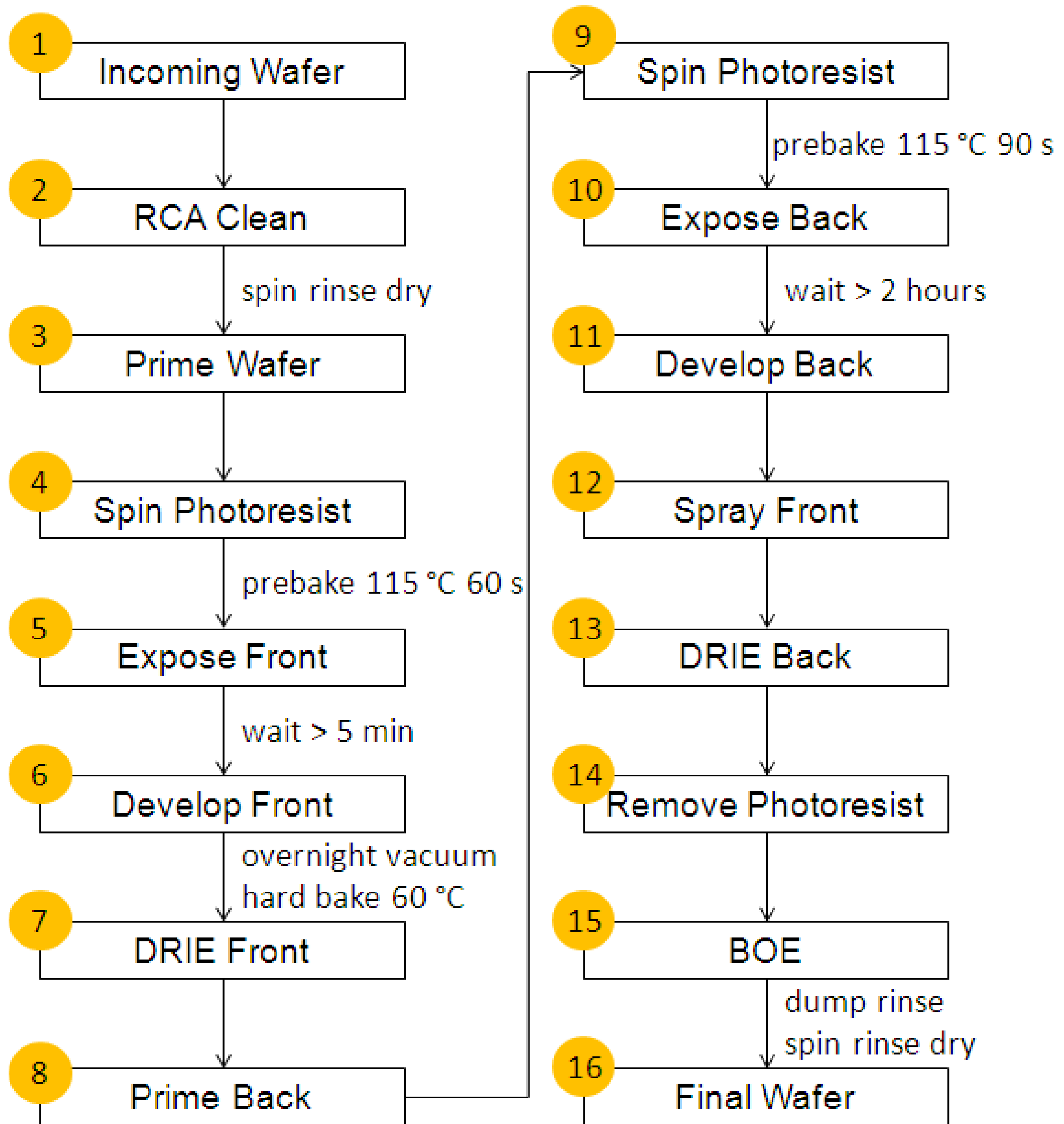

Figure 2.4: Fabrication sequence flow chart. The wafers were first cleaned, and then the front side was processed. Once the front side was done the back side was processed. To complete the fabrication the exposed insulator layer was removed.

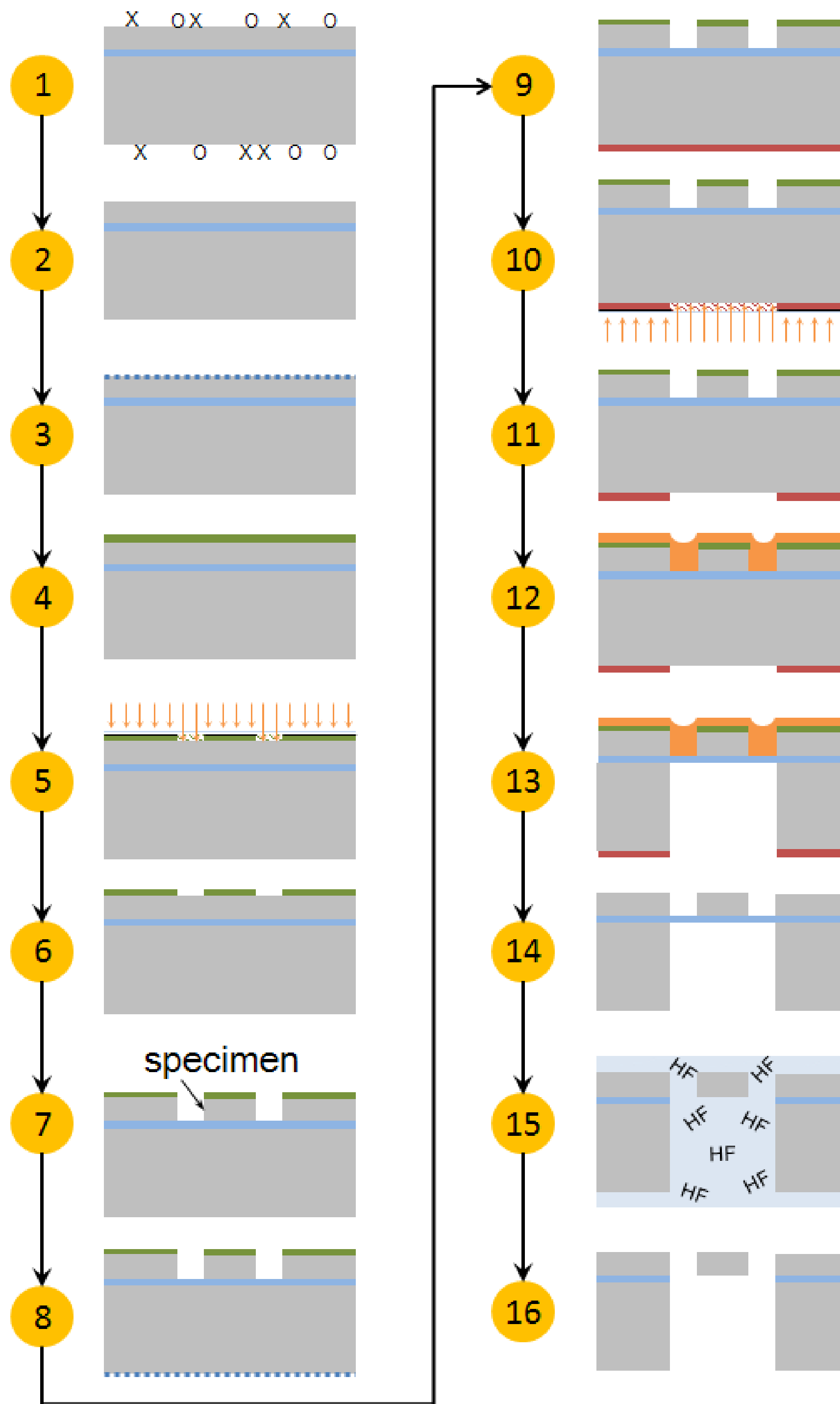

Figure 2.5: The fabrication sequence for the second generation test samples. The state of the wafer at each step is shown and this corresponds with each step in the flow chart in Figure 2.4.

2.3.1 Step 1: Incoming Wafer

As received from the manufacturer, the state of the surfaces of each SOI wafer was unknown. The surface was likely contaminated by some amount of organic and inorganic materials indicated in Figure 2.5 by the O and X symbols, respectively.

2.3.2 Step 2: RCA Clean

Each SOI wafer was cleaned with a RCA clean (named after the developer, Radio Corporation of America). This consisted of two standard clean (SC) recipes. SC1 is used to remove organics and debris while SC2 is used to remove the remaining metal contaminants left by SC1 from the surface. In SC1 the wafer is placed in a 5:1:1 mixture of deionized (DI) water, ammonium hydroxide, and hydrogen peroxide, respectively, at 80 °C for 10 minutes. After SC1 the wafer is placed into a dump rinse process that soaks the wafer in DI water for 60 s then replaces with new DI water four times. The wafer is then placed in a 2 % hydrofluoric acid solution for 20 s to remove oxidized hydrocarbons. The wafer is then placed back into the dump rinse process. In SC2 the wafer is placed in a 5:1:1 mixture of DI water, hydrochloric acid, and hydrogen peroxide, respectively, at 80 °C for 10 minutes. The wafer is then placed into a final dump rinse process and then placed in a spin rinse dryer tool (SRD-880S31EML, Semitool, Kalispell, MT) to dry the wafer without any residue. [All chemicals are from the same manufacturer (J.T. Baker, Mallinkrodt Baker, Inc., Phillipsburg, NJ).]

2.3.3 Step 3: Prime Wafer

Once the wafer was cleaned, a hexamethyldisilazene (HMDS) (J.T. Baker, Mallinkrodt Baker, Inc., Phillipsburg, NJ) monolayer was applied to the wafer in order to

promote adhesion between the wafer surface and photoresist. The development of this sensitive step will be discussed further in a later section.

2.3.4 Step 4: Spin Photoresist

A layer of positive photoresist (Microposit S1813 Positive Photoresist, Rohm and Haas Electronic Materials LLC, Marlborough, MA) was spun onto the wafer using a spinner and hot-plate tool (Model 200CB, Brewer Science, Rolla, MO). The photoresist is stored under refrigeration; prior to spinning, the photoresist is set out overnight to warm to room temperature. The photoresist was portioned onto the wafer and the wafer spun at 3000 rpm for 60 s to obtain photoresist thickness uniformity. The wafer was then prebaked at 115 °C for 60 s to bake off solvent in the photoresist [Liu *et al.*, 2011]. The photoresist layer was 1.3 μm, 1.4 μm and 1.2 μm thick for the first, second, and third batch wafers, respectively. [Step height measurements here, and throughout, were performed with a profilometer (DekTak 6m, Digital Instruments/Veeco Metrology Group, Plainview, NY); the profilometer was calibrated against a thickness standard.]

2.3.5 Step 5: Expose Front

The photoresist was then exposed at 130 mJ cm^{-2} using a front side contact aligner (MA8, Suss MicroTec, Munchen, Germany) with a 950 W Hg lamp. The sample patterns were transferred using a patterned chromium mask with soda-lime glass substrate; in the first batch the mask was made off-site (Compugraphics Photomask Solutions, Los Gatos, CA), while subsequent batches used a front side mask made on-site that will be described in a later section. The photolithographic mask designs were

transferred to the SOI wafers such that the web segment of the test samples was oriented along a <110> direction with less than 0.5° misalignment [Gaither *et al.*, 2010].

2.3.6 Step 6: Develop Front

A five-minute wait (minimum) was observed between exposure and development to ensure nitrogen outgassing of the photoresist [Liu *et al.*, 2011]. The front side was then developed to remove photoresist from the exposed areas using tetramethyl ammonium hydroxide (TMAH)-based developer (Microposit MF-319 Developer, Rohm and Hass Electronic Materials LLC, Marlborough, MA). Development took less than one minute. After development the wafer was rinsed for one minute in a deionized water bath and then placed in a spin-rinse-dryer to remove all developer and avoid residue on the exposed silicon surface. The wafer was then loaded into a vacuum oven (VWR 1410, Sheldon Manufacturing, Inc., Cornelius, OR) overnight at approximately 60 °C and a (vacuum-gauge) pressure of 98 kPa for an overnight vacuum 'hard' bake. The hard bake improves the chemical and physical stability of the photoresist [Liu *et al.*, 2011], which increases the substrate-to-photoresist etching selectivity.

2.3.7 Step 7: DRIE Front

The resulting photoresist sidewall profile from the exposure process was not perfectly vertical; the profile typically contained a footing near the substrate that was easily removed with a photoresist descum process. Prior to etching the front silicon device layer, a one to two minute photoresist descum step was performed to improve the sidewall profile of the photoresist as shown in Figure 2.6. The sidewall footing (typical of the lithographic process, but not present in the figure) and sidewall curvature in

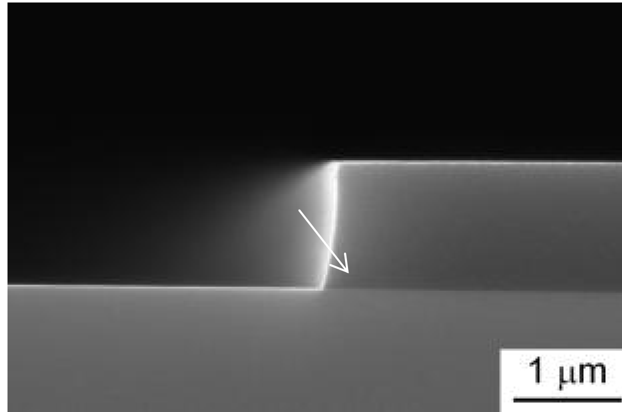

(a)

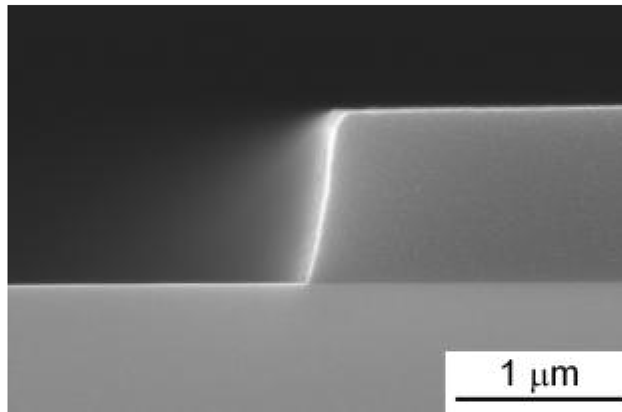

(b)

Figure 2.6: (a) Example of the sidewall profile of the photoresist in the batch A processing development prior to the descum process. The photoresist profile had a curvature and typically a footing near the wafer surface (not shown); the location of the typical footing is indicated by the arrow. (b) Another example of the sidewall profile after a one minute descum process. The profile curvature and footing have been removed.

Figure 2.6(a) is removed with the descum in Figure 2.6(b). (The two examples in Figure 2.6 are from two different process run resulting in slightly different sidewall angles but the two examples demonstrate the effect of the descum process on the sidewall profile.) This was accomplished using a reactive ion etcher (790 Series, Unaxis, St. Petersburg, FL) and the descum process was run at 80 Pa, 15 standard cubic centimeters per minute (sccm) O_2, and 150 W with a nominal photoresist etch rate of 75 nm min^{-1}. The 25 μm Si device layer was then etched using deep reactive ion etching (DRIE) techniques to create the test specimens with vertical sidewalls. As stated, three different processes were used, one for each of the batches of second generation samples. These important processes are discussed further in a later section.

2.3.8 Step 8: Prime Back

Once the front side had been etched and the sample structures created, the backside of the wafer was processed, starting with the priming of the wafer backside surface with HMDS in the same manner as Step 3. Details of this step are discussed in a later section.

2.3.9 Step 9: Spin Photoresist

A thicker layer of positive photoresist (Megaposit SPR 220-7.0 Positive Photoresist, Rohm and Haas Electronic Materials LLC, Marlborough, MA) was spun onto the wafer backside using the same spinner and hot-plate tool as Step 4. Again, the photoresist was set out overnight to warm to room temperature. The photoresist was portioned onto the wafer and the wafer spun at 1600 rpm for 60 s to obtain photoresist thickness uniformity. The wafer was then prebaked at 115 °C for 90 s to bake off solvent

in the photoresist. The photoresist layer was nominally 8.5 μm, 9.5 μm, and 8.8 μm thick for the first, second, and third batches, respectively.

2.3.10 Step 10: Expose Back

The photoresist was then exposed at 470 mJ cm^{-2} using a back side contact aligner (BA6, Karl Suss, Munchen, Germany) with a 1000 W Hg lamp. The sample patterns were transferred using a patterned chromium mask with soda-lime glass substrate (Compugraphics Photomask Solutions, Los Gatos, CA). The back side contact aligner was used to match up the front and back side patterns on the wafer using corresponding alignment marks that were included on each mask. Particular care was required to ensure the patterns were matched on each wafer.

2.3.11 Step 11: Develop Back

A two hour wait (minimum) was observed between exposure and development. The back side was then developed to remove photoresist from the exposed areas using another tetramethyl ammonium hydroxide (TMAH) based developer (Megaposit MF-26A Developer, Rohm and Hass Electronic Materials LLC, Marlborough, MA). Development took approximately two minutes. After development the wafer was rinsed and spin-rinse dried as described in Step 6. For the first batch the wafer was then placed in a vacuum oven for an overnight vacuum hard bake as described in Step 6. For the second and third batch the vacuum hard back was performed after Step 12.

2.3.12 Step 12: Spray Front

This step was added after the first batch of samples due to the need to protect the front side from an unintended etch process during the back side etch (Step 13). The development and details of this step are discussed in a later section.

2.3.13 Step 13: DRIE Back

Prior to etching the back side handle wafer, a 1 min to 2 min photoresist descum step was performed. The back side handle wafer was then etched using the same Bosch DRIE recipe for all three batch wafers. The recipe (developed with a colleague) consisted of a three step cycle: A deposition step that masks all exposed wafer surfaces, a short etch step to remove the deposited mask from the horizontal surfaces, and a longer etch step that isotropically etches the exposed silicon. This final step creates the scallops characteristic of the Bosch DRIE process. The recipe was operated at a chamber pressure of 3.1 Pa, and inductively-coupled plasma (ICP) power of 900 W. Back-side cooling was applied with helium at 6.7 kPa to help control wafer temperature during processing. The deposition step was 3 s using 60 sccm C_4F_8 and 40 sccm Ar. The first etch step was 4 s using 60 sccm SF_6, 40 sccm Ar, and a bias power of 12 W. The second etch step was 7 s using 60 sccm SF_6, 40 sccm Ar, and a bias power of 12 W. This three step process was one Bosch DRIE loop and the etch rate for this process was approximately 1 μm $loop^{-1}$. The handle wafer thickness was 400 μm for the first and second batch wafers and 480 μm for the third batch wafer. In order to complete the back side etch and fully define the structures at the end of the etch, a 5 % to 10 % increase in the number of loops was needed.

2.3.14 Step14: Remove Photoresist

After the backside was etched all resists were removed using a series of steps. Two different successful approaches were used to accomplish this step during fabrication of the three wafers. In the first, a 2 min descum in the reactive ion etcher removes the tougher outer layer of photoresist. This is follow by a 30 min bath of 65 °C photoresist stripper (Microposit Remover 1165, Rohm and Hass Electronic Materials LLC, Marlborough, MA). The clean process was completed with a 30 min etch in a microwave asher (Model 300, PVA TePla, Corona, CA) at 500 W, 60 Pa, and 600 sccm O_2. In the second, the wafer was placed into a bath of Remover PG (MicroChem, Newton, MA) at 65 °C for 10 minutes, and then placed into a dump rinse cycle. After the dump rinse the wafer was placed into a room temperature bath of Nanostrip (OM Group, Cyantek, Fremont, CA) for up to 2 min, and then placed back into a dump rinse cycle followed by the spin-rinse-dryer. The Remover PG removes the majority of the photoresist, while the Nanostrip removes the last layer of photoresist that tend to be more difficult to remove.

2.3.15 Step 15: Buffered-Oxide Etch (BOE)

Once the resist materials were removed from the wafer, the oxide layer (2 μm for the first and third batch, 1 μm for the second batch) was etched using a 6:1 buffered-oxide etch (BOE) mixture (J.T. Baker, Mallinkrodt Baker, Inc., Phillipsburg, NJ) containing hydrofluoric acid and ammonium fluoride. This released the specimens from surrounding material (except where they were attached to the test strip); island structures inside and around the samples were released and remained in the BOE bath.

2.3.16 Step 16: Final Wafer

After all processing has been completed the samples and test strips are ready for removal from the wafer. Prior to removal, optical images were captured of each sample (see Ch. 3). Test strips were removed with a diamond scribe on the narrowed outer regions of the strips.

2.4 Defining Structures

This section covers details regarding the fabrication process, covering steps 3 to 6 and 8 to 11 in Figure 2.5, in particular the modifications made to Steps 3 and 8. For the batch A wafer the front and back sides were primed by first performing a 1-min dehydration bake at 200 °C to remove moisture from the surface. Directly after the dehydration bake HMDS was spun onto the wafer at 3000 rpm for 30 s. This procedure appeared to work well with the batch A wafer; a monolayer of HMDS was applied without producing problems with the subsequent lithographic processes as shown in Figure 2.6(a). However, while working on the process development for later batch wafers, a significant problem arose. Using this HMDS priming process, the photoresist sidewall angle and develop times were not consistent with identical runs of the subsequent steps (*i.e.*, spin, expose, and develop photoresist) to the HMDS priming.

The photoresist sidewall profiles can be seen in Figure 2.7. Photoresist development after exposure, using the front and back side processes, are supposed to take less than one and two minutes, respectively, based on the photoresist and exposures used with reference to manufacturer product specifications; this was not typically the case. The develop times took upwards of 5 minutes and 15 minutes for the front- and back-side

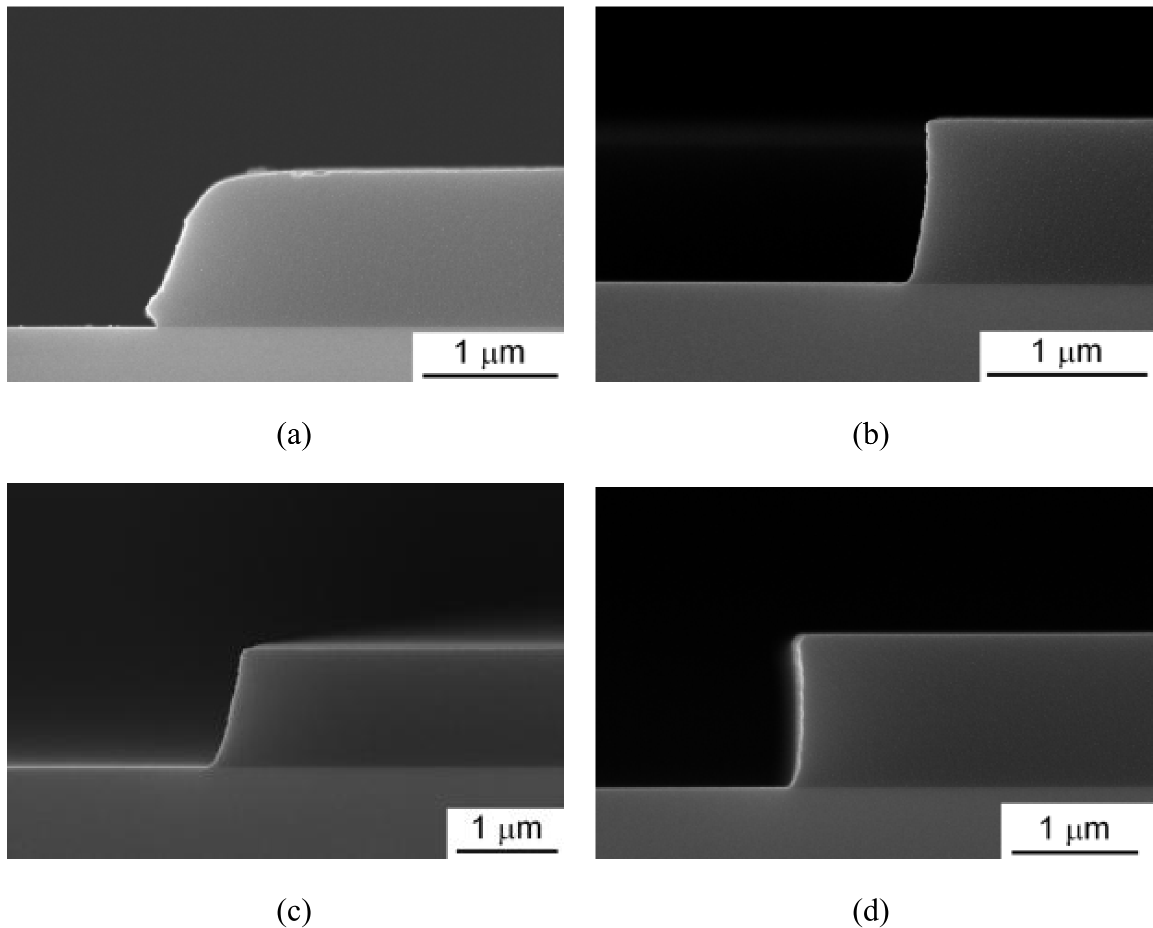

(a) (b)

(c) (d)

Figure 2.7: The effect of the HMDS priming method on photolithographic sidewall angles. (a) The poor sidewall angle due to the HMDS liquid spin-prime process. (b) The process in (a) modified with a g-line UV light filter resulting in a better profile. (c) The vapor priming process effect on the original (broadband UV) exposure resulting in a profile consistent with the original photoresist profile in Figure 2.6(a). (d) The vapor priming process effect on the g-line exposure used in (b) resulting in an essentially vertical sidewall.

processes, respectively. Furthermore, the sidewall angles, for the same processes, which had been shown to produce nearly vertical sidewalls as desired in earlier attempts [Figure 2.6(a)] such as the batch A wafer, would get progressively worse, as in Figure 2.7(a), with the longer develop times required in a process run. Many attempts to address this problem were undertaken, including increasing the spin speed and time for the HMDS spin process to 5000 rpm for 60 s, increasing photoresist exposure time, and switching from broadband ultraviolet (UV) light exposure to exposure at particular wavelength with UV wavelength filters, *e.g.*, a 435 nm wavelength UV filter called g-line for the front side photoresist. Changing the HMDS spin speed and time did not change any results. The increase in exposure time did decrease the develop time but also overexposed the sample patterns, altering the sample dimensions. The g-line UV filter did improve the sample sidewalls to nearly vertical [Figure 2.7(b)], and improved the develop times somewhat, but develop times were still outside the expected ranges.

An additional option in this set of experiments was a new HMDS vapor priming tool (YES-310TA, Yield Engineering Systems Inc., Livermore, CA), which became available during the time of this investigation. The vapor priming process was performed at 150 °C on clean bare wafers and took 20 min from start to finish. By placing the wafers inside the oven at 150 °C the HMDS could be deposited onto the wafer as a monolayer from the vapor phase. Wafers that were vapor primed resulted in desired photoresist sidewall profiles and develop times, whether exposed with broadband or g-line UV light. The photoresist profiles of the broadband and g-line exposures are shown in Figure 2.7(c) and (d) respectively. The fabrication sequence was modified to use the vapor priming process for steps 3 and 8 in Figure 2.5 and broadband UV light exposure

was kept for steps 5 and 10 in Figure 2.5 since the descum process in steps 7 and 13 already removes photoresist footing and improves the vertical nature of the sidewall profile.

2.5 Creating Structures

This section covers the processes used in the creation of device layer structures that occurs during step 7 using various etching techniques. Three different DRIE processes to define the sample structures were used in order to determine the effects of processing on the surface structure (Ch.3) and consequently the sample strength (Ch. 6). These MEMS-relevant processes [Li *et al.*, 2003; Tsui *et al.*, 2004; Sun *et al.*, 2005; Henry *et al.*, 2009] were chosen to show that this strength testing methodology can be used for MEMS processing assessment and optimization for MEMS device reliability.

Batch A and B samples were both fabricated using Bosch DRIE recipes developed on a deep silicon etching tool (Shuttleline, Unaxis USA Inc, St. Petersburg, FL) that produced different scallop sizes (discussed in Ch. 3). Similar to the recipe described in the step 14 subsection, each Bosch DRIE recipe was operated with an ICP power of 900 W, 40 sccm Ar, and He back-side cooling at each step in the cyclic etch process. For the deposition step, both recipes used 60 sccm C_4F_8, the batch A recipe for 2 s at 2.9 Pa chamber pressure and the batch B recipe for 3 s at 3.1 Pa. For the first etch step, both recipes used 60 sccm SF_6 and a bias power of 12 W, the batch A recipe for 3 s at 3.2 Pa chamber pressure and the batch B recipe for 4 s at 2.9 Pa. For the second etch step, both recipes used a bias power of 12 W at 3.1 Pa chamber pressure, the batch A recipe with 80 sccm SF_6 for 3 s and the batch B recipe with 120 sccm SF_6 for 6 s. Prior to

running these recipes the tool chamber was cleaned to remove potential contamination using a standard two-step etching process for 30 min to 60 min with first an O_2, Ar, and SF_6 mixture and then an O_2 and Ar mixture.

The batch A wafer was etched with a total of 63 process loops. During the etch process the wafer backside is cooled with He to control the wafer temperature; however this did not maintain the wafer temperature through the full set of cycles and the wafer warmed as the number of consecutive loops increases. This causes the pitch of the scallops to increase over the total set of loops completed in a single etching. In order to optimize the process for batch B, changes to the batch A process was explored to attempt to compensate this behavior.

The process was modified in two ways and these results are shown in Figure 2.8. In the first change, the second etch step was linearly morphed from 3 s to 3.5 s over 80 loops, shown in Figure 2.8(a), to compensate the wafer heating response. In the second change, the total front etch process was split into multiple etch steps to avoid the wafer heating response, so the etch was done with the batch A process with 20-loop steps with 30 minute breaks until 80 loops are completed, shown in Figure 2.8(b). The morphed etch process did not produce an improved etch quality while the multiple etch steps modification produced the most uniform etch steps. The multiple etch steps were used to modify the batch B front side etch, using 10-loop steps 4 times with a final 3 loops to etch the remaining front side silicon, resulting in a total of 43 etch loops.

The cryogenic DRIE process, which was developed at −110 °C, on an ICP etching tool (PlasmaLab System 100, Oxford Instruments, Bristol, England), was particularly difficult to optimize. The process was developed from scratch, with the choice of

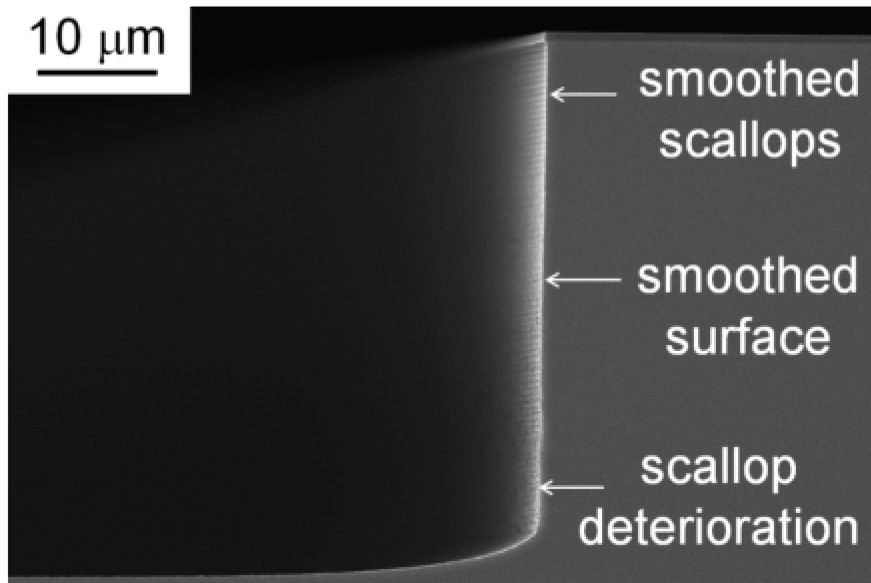

(a)

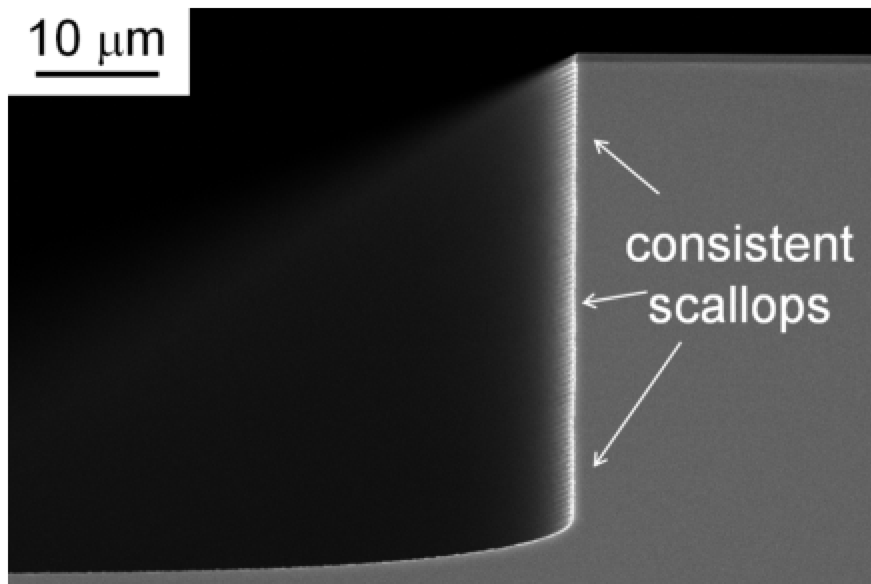

(b)

Figure 2.8: Bosch DRIE process modifications. (a) Etch step morphed linearly by 0.5 s over 80 loops produced an inconsistent etch profile resulting is smoothed regions and deteriorated scallops (b) 80 loop etch process modified by performing it in sets of 20 loops resulting in consistent scallop pitches.

−110 °C to achieve an anisotropic etch profile, fast silicon etch rate, and greater silicon-to-mask etching selectivity [Zhao *et al.*, 2000]. Silicon etch rates as great as 30 μm min^{-1} have been observed with deep cryogenic etching [Jansen *et al.*, 2009]. A number of other parameters were variables in the process development including the chamber pressure, ICP and bias power for the plasma striking and etch steps, Ar flow rates to strike plasma, and O_2 and SF_6 flow rates for the etching step. Several etching parameters were monitored during the process development, specifically etch rate, silicon-to-mask selectivity, sidewall angle, and the shape of the etch profile base.

The first problem that was difficult to overcome was to light the plasma and have it sustain for the duration of the etching process. This depended on selecting an effective combination of chamber pressure, ICP and bias power, and the amount of Ar in the O_2 and SF_6 gas mixture. The optimal conditions will be detailed later in the recipe description. The other problem observed early in the process development was photoresist cracking and delaminating at the processing temperature, as shown in Figure 2.9. When the photoresist thickness was greater than 1.3 μm and the wafer was inserted into chamber when the cooling system was at-temperature (−110 °C) the photoresist would crack and delaminate as in Figure 2.9(b) due to thermal shock and possibly the thermal expansion mismatch between the silicon and photoresist; however, if the wafer was allowed to cool gradually, by placing it in the chamber prior to the cooling system being at-temperature, the cracking and delamination did not occur, as shown in Figure 2.9(a). The problem could be avoided entirely by using photoresist thicknesses less than or equal to 1.3 μm. This was the preferred solution as it saved processing time.

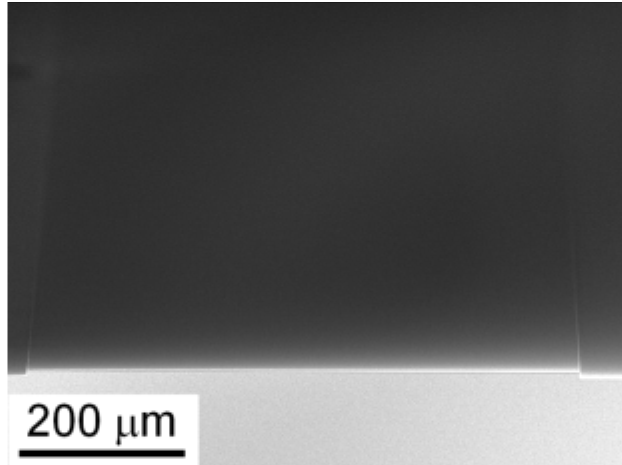

(a)

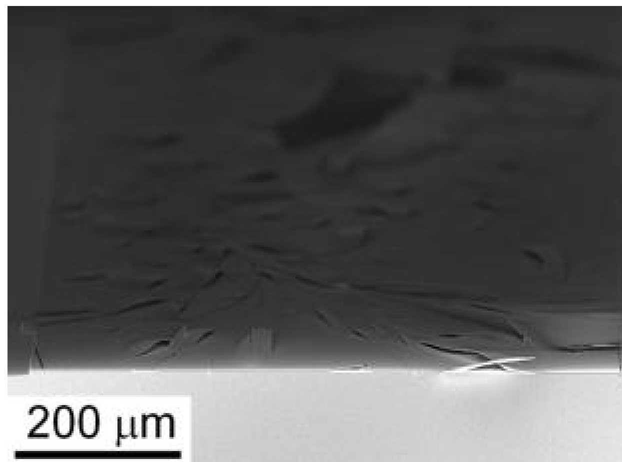

(b)

Figure 2.9: Photoresist behavior during the cryogenic DRIE processing. (a) The resist maintains its single layer state. (b) For the same type of feature as (a) the photoresist cracks and delaminates from the surface prior to or during the etch process. Two specific conditions caused this resist damage to occur: When the resist thickness was greater than 1.3 μm and when the wafer is thermally shocked, changing from room temperature to −110 °C quickly.

Photoresist cracking has been observed with other photoresists used in the cryogenic DRIE process [Sainiemi and Franssila, 2007; Kamto *et al.*, 2010].

Methods have been developed that detail how to generate and optimize cryogenic DRIE processes [Zhao *et al.*, 2000; de Boer *et al.*, 2002; Chekurov *et al.*, 2007; Jansen *et al.*, 2009]. These methods were used for guidance in selecting starting parameters and subsequent modification. The silicon etch rate was highly dependent upon the ICP power, with greater ICP power resulting in higher etch rates, while the silicon-to-mask selectivity was dependent significantly on the bias power, with lower bias power increasing the selectivity. The bias power could not be reduced too low due to the need for it in the electrical pathway and maintaining the plasma; this was particularly significant for the SOI wafers and silicon dioxide coated test wafers as the insulator disrupted the electrical pathway. The ICP and bias power settings for a particular set of gas mixtures also affected the etching profile; the power setting produce a DC bias voltage with the wafer as part of the electrical conduction pathway, and the best etch profile results were observed for bias voltages between 20 V and 40 V. The etch profile of the wafer was also sensitive to the O_2 concentration, as observed by other researchers [Jansen *et al.*, 2001; Addae-Mensah *et al.*, 2010] with greater concentrations of O_2 resulting in more positively tapered sidewalls and very low or no O_2 resulting in isotropic etching. Some of the etching profiles, observed during the development of the cryogenic DRIE recipe, are shown in Figure 2.10 and Figure 2.11.

In Figure 2.10 etch profiles from the early stages of the process development are featured to illustrate the different types of etch behavior observed under particular sets of conditions. Figure 2.10(a) is the etch profile from a 15-min etch that only had a faint

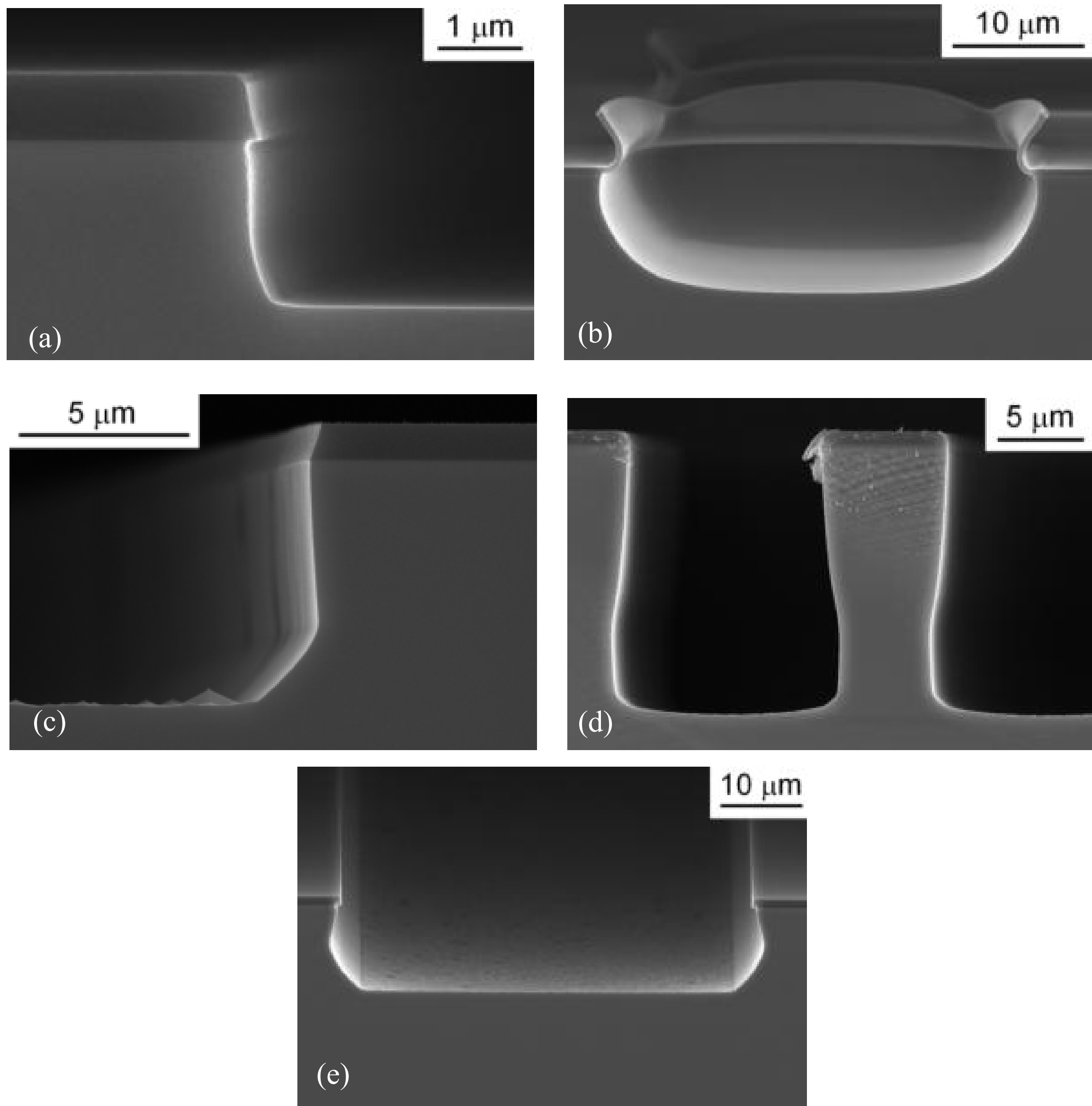

Figure 2.10: Etch profile results during the early stages of the cryogenic DRIE process development. (a) Plasma did not fully ignite resulting in a very slow etch rate over 15 minutes. (b) Very low O_2 concentration resulting in isotropic etching (and curling of the unattached photoresist). (c) Low-temperature (−130 °C) produced near-crystallographic etching of the silicon (note the pyramid-like micro-masked structures on the left horizontal surface). (d) Oxide masking (between photoresist and silicon) produced inconsistent etch profiles resulting from the insulator layer effect on the wafer conductivity. (e) Low bias power did not direct the etching radicals downward resulting in side wall etching.

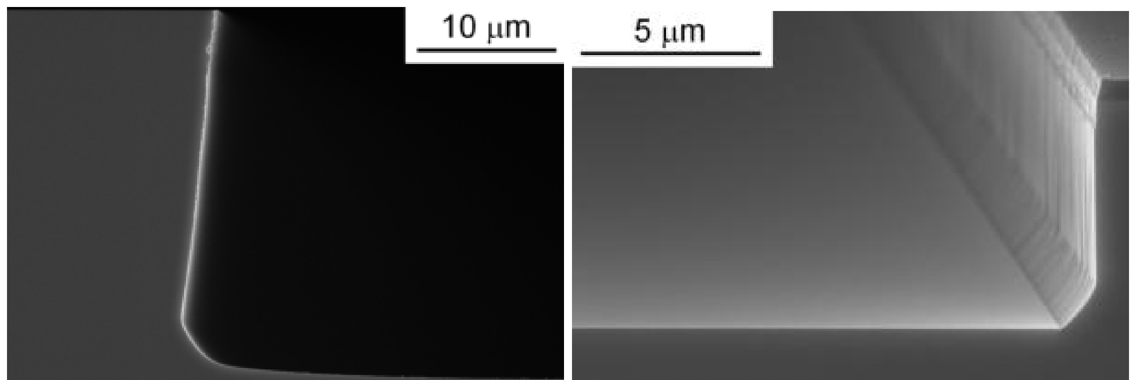

(a) (b)

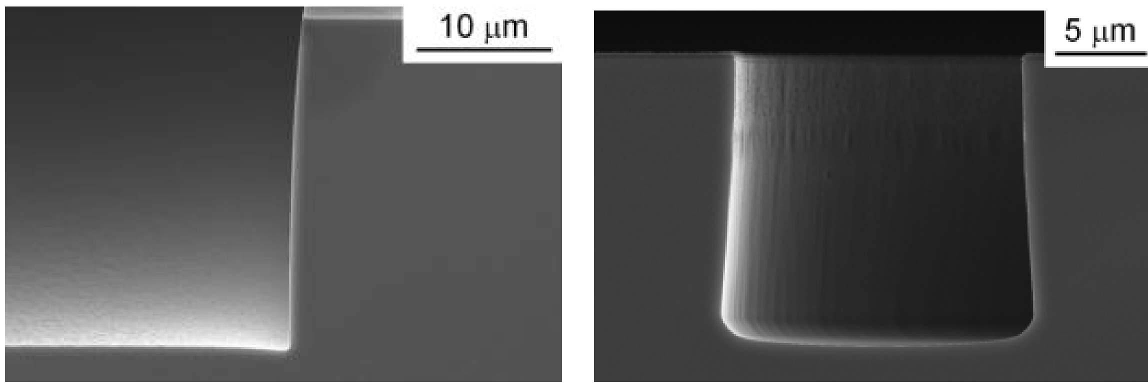

(c) (d)

Figure 2.11: Etch profile results during the cryogenic DRIE process development approaching the optimal conditions. (a) Low bias power and low O_2 concentration resulted in a negative sidewall taper and footing. (b) Low ICP power and high bias resulted in a higher bias voltage potential and a profile that was near vertical with a footing. (c) High O_2 concentration resulted in a positive sidewall taper. (d) Low O_2 concentration produced a negative sidewall taper. All etch profiles are from 10 min process runs.

greenish plasma glow near the wafer surface; the silicon etched very slowly and with a poor vertical sidewall due to the plasma not fully lighting. The chamber should glow a bright pink-purple when properly lit. Figure 2.10(b) is the etch profile from a 9-min process run with very little O_2. The isotropic etching is the result of an insufficient amount of O_2 to passivate the silicon sidewalls from the SF_6 radicals, which were free to etch all the exposed silicon. The photoresist is seen to have curled backwards in the areas where the silicon has been removed from beneath it. Figure 2.10(c) shows the etching result from a 10-min process run at −130 °C, which appears to exhibit crystallographic-dependent etching near the bottom of the etch profile, indicated by the pyramid-like structures at micro-mask locations and the straight footing on the profile base. Crystallographic-dependent etching at −125 °C has been observed elsewhere [Craciun *et al.*, 2002]. The process development at −110 °C did not exhibit crystallographic-dependent etching. Figure 2.10(d) shows a 10 min process run for a wafer that included a silicon dioxide layer between the silicon and photoresist layer. The reason for the inclusion of this layer will be discussed later in this section. The silicon dioxide layer produced inconsistent and undesirable etch profiles such as in Figure 2.10(d) that was likely due to this insulating layer disrupting the silicon wafer conduction pathway necessary for the process to run properly. Process optimization with the oxide layer was abandoned due to inconsistent etch behavior. Figure 2.10(e) shows the etch profile of a process run with a relatively low bias power. The bias power was insufficient to fully drive the plasma etching gases downward, normal to the wafer, to obtain a vertical etch profile. This resulted in sidewall etching.

The etch profiles in Figure 2.11 are from the process development near the optimized conditions. In Figure 2.11(a) a negative sidewall angle and some footing is a result of a low bias power and low O_2 concentration. Figure 2.11(b) is an etch profile with a vertical sidewall but with a footing. This is the result of low ICP power and high bias power and a corresponding higher bias voltage potential. The etch profiles in Figure 2.11(c) and (d) are nearly optimized, with only the O_2 concentration being too high in Figure 2.11(c), resulting in a positive sidewall taper, and too low in Figure 2.11(d), resulting in a negative sidewall taper.

The cryogenic DRIE technique is sensitive to feature size and separation [Walker, 2001; Craciun *et al.*, 2002]. Both the etch rate and sidewall angle in the process development were varied by the size and separation of features on the second generation mask. This can be seen across the selected mask features shown in Figure 2.12, where the etch profile of a 10-μm feature in Figure 2.12(a) has a positive taper to the etch profile and an etch depth of 28 μm while a 50-μm feature in Figure 2.12(b) has a negative taper to the etch profile and an etch depth of 31 μm. The cryogenic DRIE process was optimized for the web region of the theta samples, as this feature is the critical dimension of the samples and all other features with larger separation between adjoining features have slightly curved sidewall profiles.

The photoresist mask did present a problem in the process development for longer etch times as shown in Figure 2.13(a). During the front side etch process the edge of the photoresist layer etched away faster than the rest of the photoresist and consequently revealed new silicon that began etching at the top of the etch profile. This change in surface finish was not desirable. To attempt to avoid this problem a 220 nm silicon

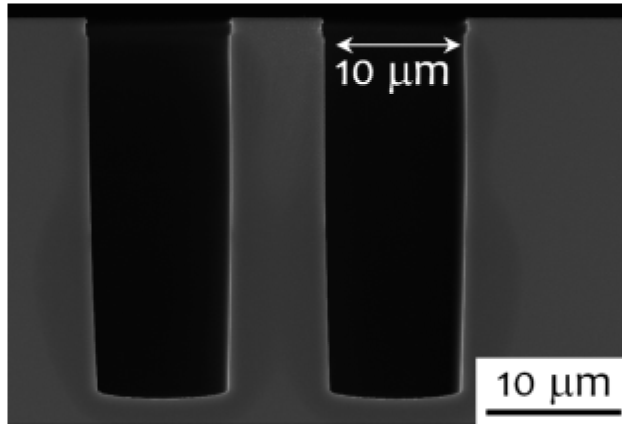

(a)

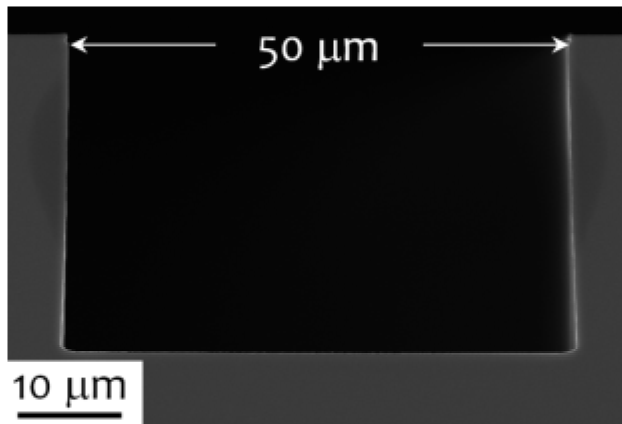

(b)

Figure 2.12: Feature size dependent etch profile behavior in the cryogenic DRIE process. Different feature sizes result in different side wall profiles and etch rates. For the example case shown, in (a) the 10 μm wide feature has a positively tapered etch profile and etch depth of about 28 μm, while in (b) the 50 μm wide feature on the same etched wafer has a negative profile taper and an etch depth of about 31 μm.

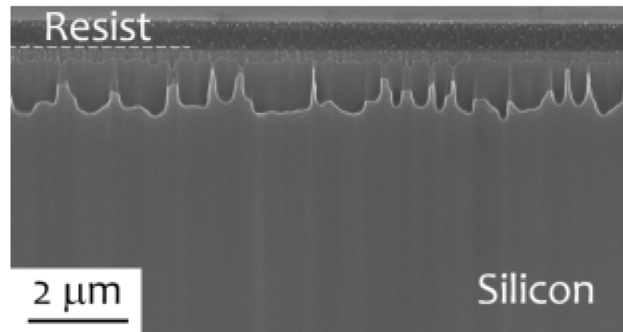

(a)

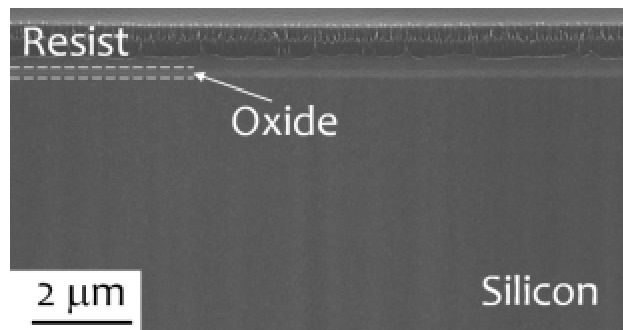

(b)

Figure 2.13: The cryogenic DRIE process near the silicon-photoresist edge. (a) The edge of the photoresist layer etched away faster than the rest of the photoresist and consequently revealed new silicon that began etching at the top of the etch profile during the deep etch process. (b) By adding a thermally-oxidized silicon dioxide layer between the silicon and photoresist, this effect was greatly decreased.

dioxide layer was added to the test wafers using low-pressure chemical vapor deposition tool (Mini Tytan 4600, Tystar, Torrance, CA) prior to the photoresist spin, exposure, and development. The exposed oxide layer was etched using an oxide etch process in a reactive ion etcher, using a 80 sccm CHF_3 and 1.2 sccm O_2 mixture at 200 W. The result of the cryogenic DRIE process using this is shown in Figure 2.13(b) where the photoresist damage is restricted to the photoresist layer. The oxide layer appears to dampen the damage process; however, this modification also produced inconsistent silicon etch profiles [Figure 2.10(d)] and could not be used for the batch C wafer fabrication. Using the silicon dioxide layer as the only mask also could not be used for two reasons: (1) The exposed silicon dioxide layer contributed oxygen to the chamber gas mixture and requires further process development to compensate; (2) the addition of a second insulator layer, on outside of the SOI wafer caused significant electric disruption in the bias voltage behavior for the process condition that could not be compensated for. The photoresist damage problem could not be removed in the process development.

The optimized cryogenic DRIE process started with a 3-min wafer temperature stabilization step with 1.3 kPa of He backside cooling used to bring the wafer to −110 °C. A 10 s gas stabilization step was then performed at 1.1 Pa with 25 sccm SF_6, 5 sccm O_2, and 50 sccm Ar, followed by a 5 s plasma strike step using an ICP and bias power of 1800 W and 30 W, respectively, with 28 sccm SF_6, 5 sccm O_2, and 25 sccm Ar. In the following etch step, which is performed for the desired length of time, the bias power is reduced to 5 W and Ar is removed. The greater initial amount and following reductions in Ar is done because the Ar is needed to strike the plasma and the reduction is to gradually transition to no Ar in the following etch step. The process had an etch rate of 25 μm

min^{-1}, a sidewall angle of 90°, and a silicon-to-photoresist selectivity of greater than 20. Prior to the etching the wafers a room temperature chamber cleaning process was run using a SF_6 and O_2 etching mixture which was run for 30 min to 60 min.

The process optimization results for the Bosch and cryogenic DRIE are shown in Figure 2.14. Both examples are process development test wafers viewing a cut through a theta sample web region. The etching on these wafers was deep enough (> 25 μm) to show that each developed recipe would produce vertical sidewalls for the entire front side etch of the SOI device layer. Dozens of 100-mm test wafers (Montco Silicon Technologies Inc., Spring City, PA) were consumed in the optimization of the three batches.

2.6 Preserving Structures

This section covers the discovery of the need for step 12 in Figure 2.5, the methods attempted, and the method adopted to accomplish front side protection. During the fabrication of the batch A samples unforeseen problems arose that needed to be addressed for future fabrication runs, specifically cracking and break of the exposed oxide layer and unintended etching of the front side.

An unexpected aspect of the batch A wafer processing was that the 2-μm oxide layer cracked and broke during the back side etch step as the oxide layer was being completely released (in areas where the front side was etched). The oxide layer is compressively stressed in the SOI wafer and the large openings on the mask design allow the oxide layer to buckle when large areas are exposed, and the oxide layer subsequently

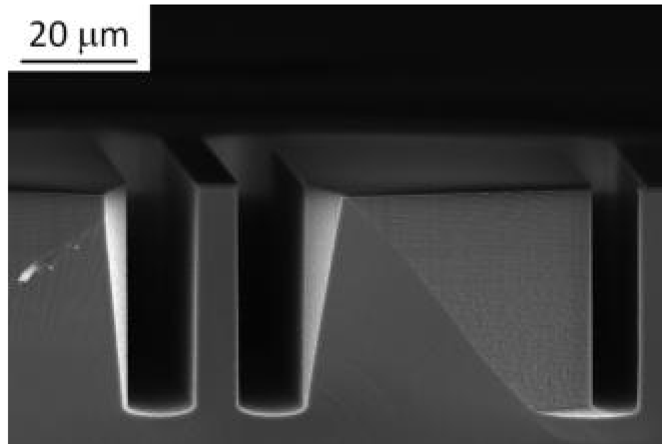

(a)

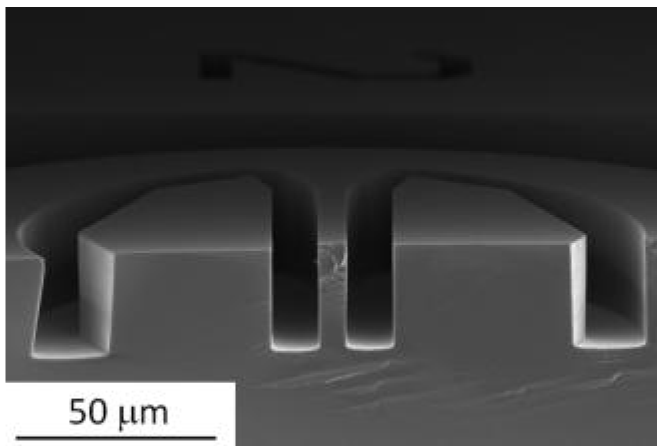

(b)

Figure 2.14: Optimized profiles of the (a) Bosch and (b) cryogenic DRIE process. The etched sidewall profiles are vertical.

cracks and breaks out either during the etching or as the wafer experiences any jarring during the loading and unloading of the wafer or other wafer handling. This is likely the origin of the second unintended etch surface (discussed in the next section); wherever the oxide layer broke open during the backside etch would allow the front side to be etched irregularly for the remainder of the back side etch step. Furthermore, observations of the front side etch prior to the back side etch did not reveal any clear variation between samples.

Figure 2.15 shows examples of samples directly after the back side etch in the batch A fabrication in which the oxide layer has broken out (prior to the oxide etch). In Figure 2.15(a) the broken out oxide layer is apparent near the top of the image. The sample edges appear smooth in this image. However in Figure 2.15(b) the broken out oxide layer is again at the top but the sample edges appear ragged. Figure 2.16 shows a sample fragment from batch A after it was released and broken from a test strip, which has two etch qualities (on the left side). There is a mesa that has a surface of DRIE scallops while the remainder of the surface has an unintended pitting etch quality that appears to have eaten away the scallops in all areas except the location of the mesa. The ragged edge of the sample in Figure 2.15(b) likely corresponds to the larger unintended pitting etch surface while the smooth edge sample in Figure 2.15(a) corresponds to the intended scalloped surface; this is discussed further in Ch. 3.

Two changes were made to the fabrication of subsequent sample batches. The first change was to modify the front side mask layout to fill in the openings present around samples in the first mask of second generation specimens, as shown in Figure 2.17. Island structures, capable of floating away during the BOE step of the fabrication,

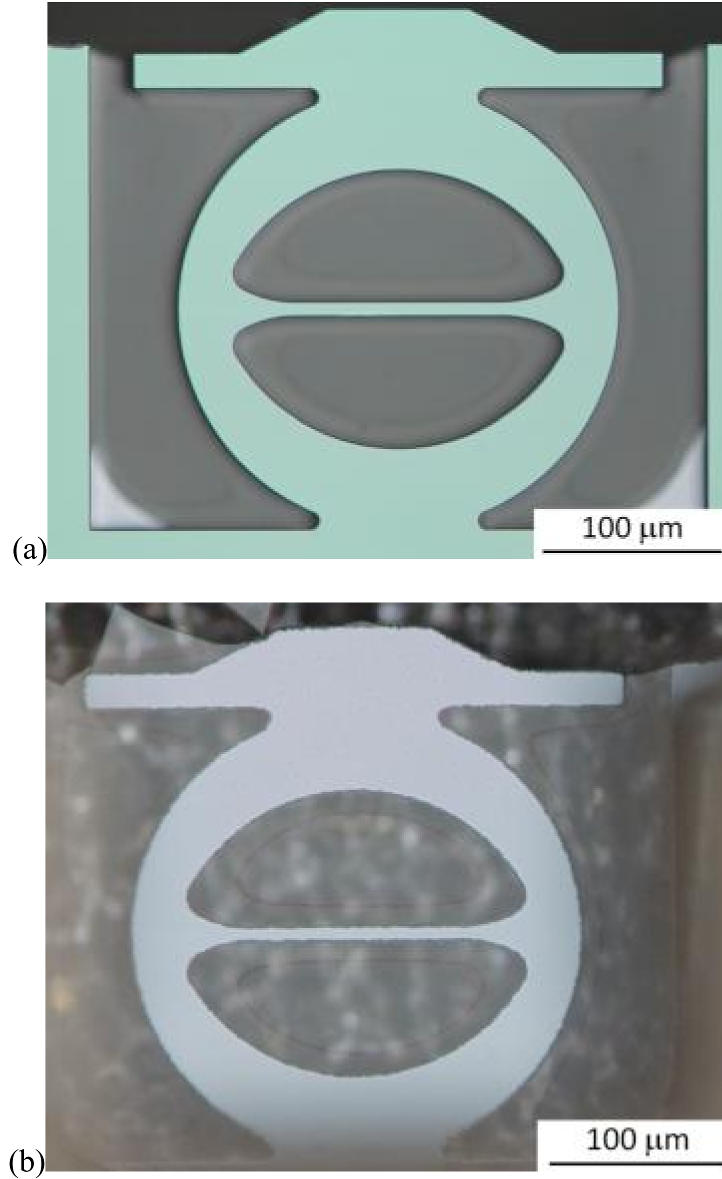

Figure 2.15: Examples of resulting samples for the first fabrication run prior to the oxide removal. The 2-μm oxide layer attached to and around the sample is gray. The black area at the top of the samples is area where the oxide layer has broken out of the wafer. (a) An arch theta sample with smooth edges. (b) An arch theta sample with rough edges and reduced web width dimension.

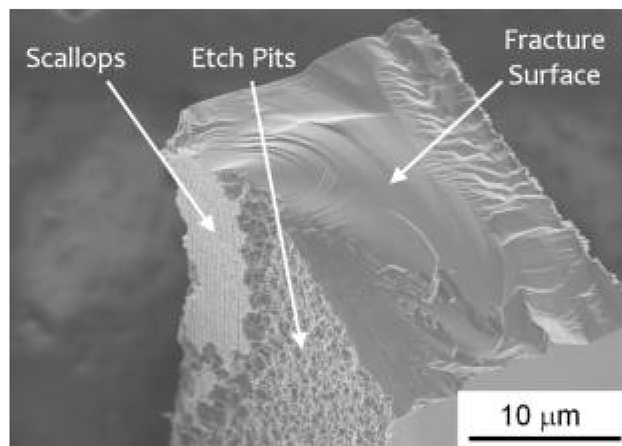

Figure 2.16: Fragment of a sample from the batch A wafer that shows the etch results of the fabrication sequence.

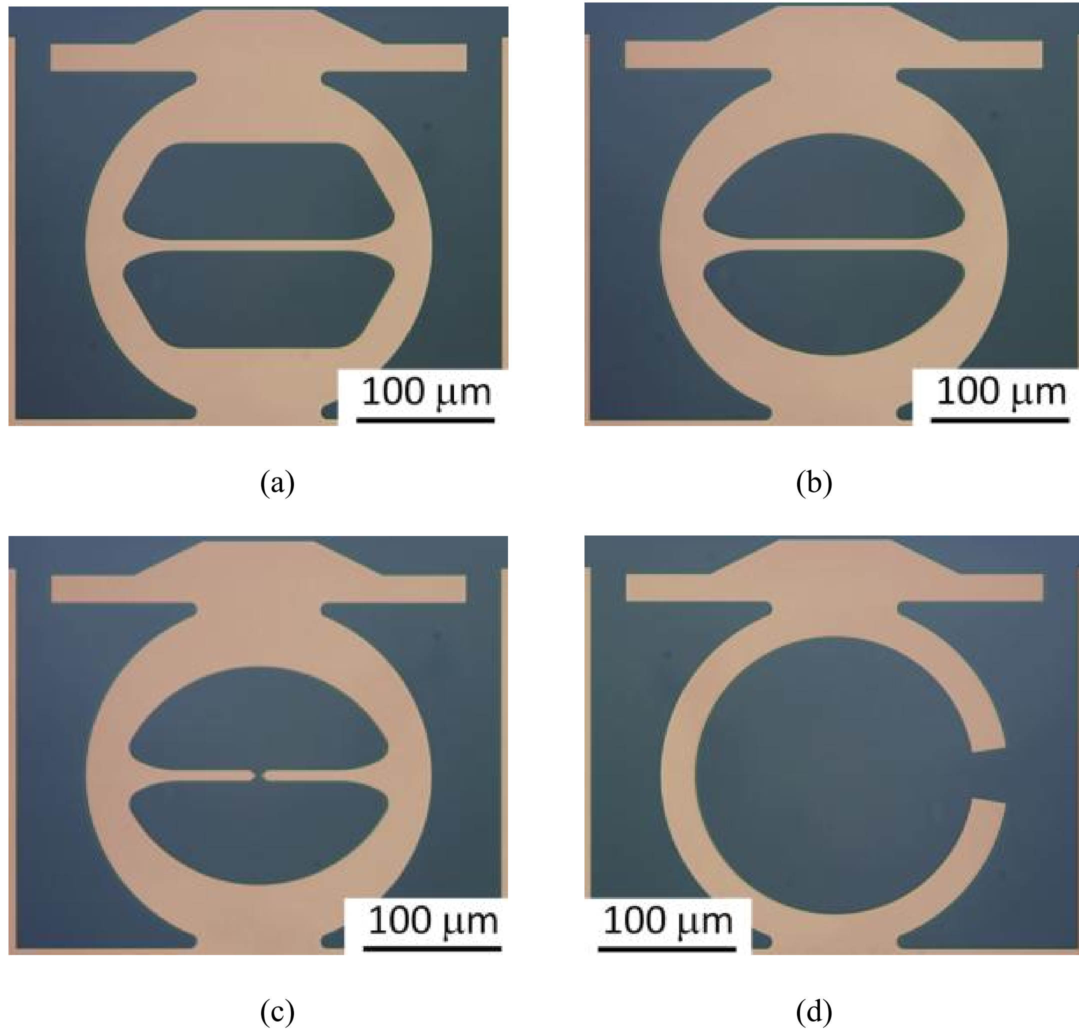

Figure 2.17: The four specimen designs as they appear on the first mask of the second generation specimens: (a) Durelli, (b) arch, (c) gapped-arch, and (d) C-ring.

were added in the critical areas of the samples, namely the inside of the theta samples [Figure 2.17(a) to (c)] and the inside and outside of the C-ring samples [Figure 2.17(d)]. These modifications are shown in Figure 2.18. The island structures were included for two reasons: (1) The oxide layer is less likely to crack in these smaller regions; (2) the islands provide a uniform feature size openings in these critical areas that allow for effective etch process optimization, especially important for the cryogenic DRIE process.

The modified 100-mm wafer mask was generated using a mask making tool (DWL 66FS, Heidelberg Instruments, Heidelberg, Germany) with a 4-mm write head. The mask blank (Nanofilm, Westlake Village, CA) consisted of a soda lime glass substrate and a thin layer of chromium. The soda line and chromium mask blank was covered with photoresist (AZ 1518, Clariant, Somerville, NJ). The photoresist was exposed with the updated mask design on the mask maker and then developed with MF-319 (Microposit Developer, Rohm and Hass Electronic Materials LLC, Marlborough, MA). Following development and a dump rinse step the exposed chromium was etched for 60 s in a chromium etchant (Type 1020, Transene Company Inc., Danvers, MA). After the chromium etch the mask was dump rinsed and the photoresist was removed using the Remover PG and Nanostrip cleaning process covered earlier.

After the spin-rinse-dry the mask was complete and this mask was used for step 5 in the fabrication flow for the batch B and C wafers (as well as for all test wafer process development). The web width of the modified front side mask was w =7.6 μm compared to w = 7.7 μm for the original front side mask.

The second modification was to cover the front side with an additional protective masking layer in an effort to stop the oxide layer from cracking and breaking when large

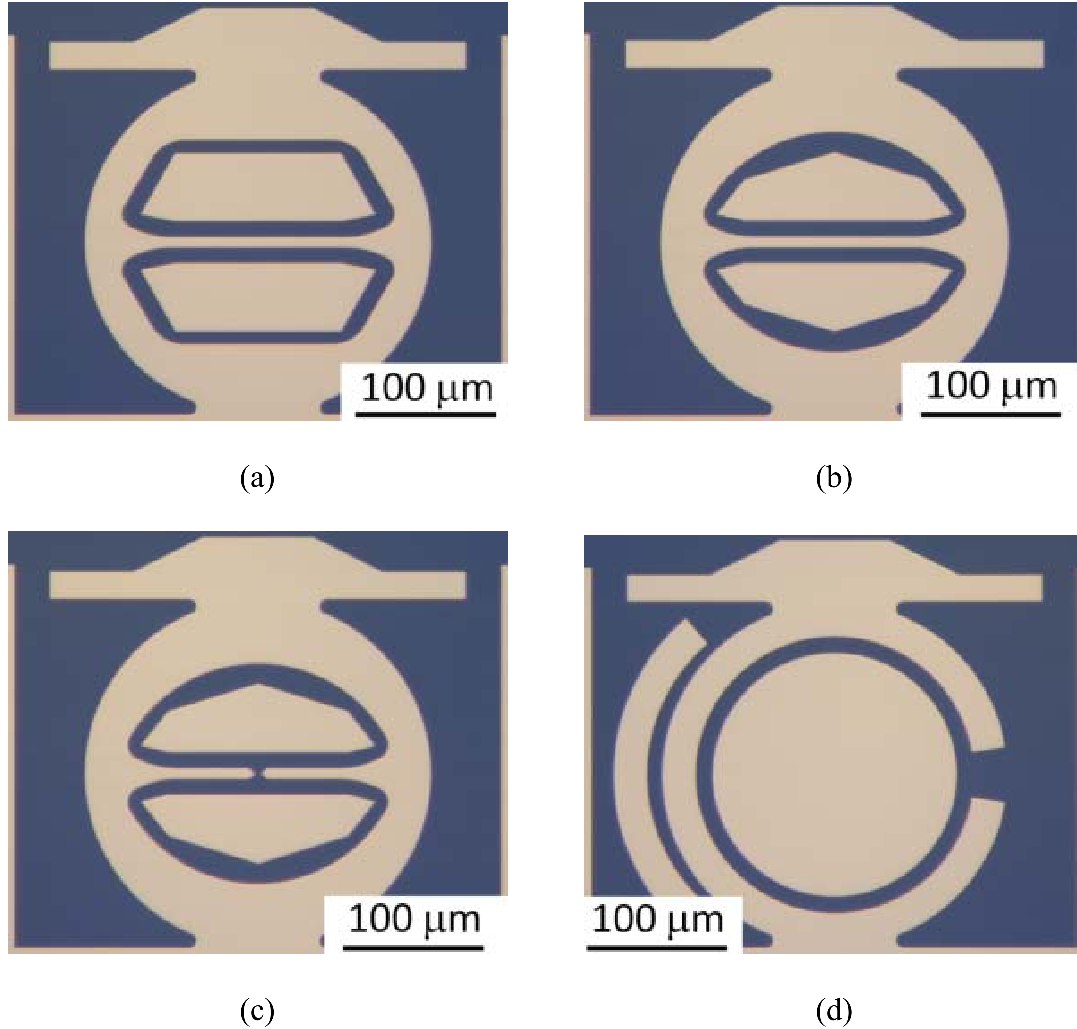

(a) (b)

(c) (d)

Figure 2.18: Updated mask design for each of the specimen types featured in Figure 2.17: (a) Durelli, (b) arch, (c) gapped-arch, and (d) C-ring. These designs include sacrificial island structures to fill spaces inside and around important structures on samples. This keeps the load constant around these areas and decreases the likelihood of cracks forming in the oxide during the back side etch step.

areas were exposed. The first approach was to deposit a conformal plasma-enhanced chemical vapor deposition (PECVD) silicon dioxide layer. This was performed on a modified reactive ion etching tool (790 series, Unaxis USA Inc., St. Petersburg, FL) using a process at 300 °C and 120 Pa with a gas mixture of 160 sccm SiH_4 and 900 sccm N_2O. This was performed in two 5 min deposition steps with a rotation of the wafer in the chamber by about 135° to minimize pinhole generation in the deposition process. The conformal deposition on the side walls was about one-fourth that of the horizontal wafer surfaces resulting in an approximately 100 nm silicon dioxide layer covering the etch scallops. The results of this approach in the fabrication process are shown in Figure 2.19. In Figure 2.19(a) and (b) the conformal oxide coating is present even at the silicon-oxide interface; however, this oxide coating was not sufficient to withstand the oxide breaking and unintended etching process as can be seen in the etch damage on the theta sample in Figure 2.19(c). The PECVD oxide was either removed in part when the buried oxide layer broke open or the PECVD was etched away when exposed to the etch gases after the buried oxide layer broke open.

Another approach was to spin an additional layer of photoresist on the front side after the front side etch step using the same front side spin recipe. The results of this approach are shown in Figure 2.20. In Figure 2.20(a) the spun-on resist was not conformal nor did it fill the etched features. The resist was thin in areas of the etch profile. The processing result in Figure 2.20(b) shows some etch damage though the etch surface was mostly protected by this process. The oxide layer was still able to break open using this protection method.

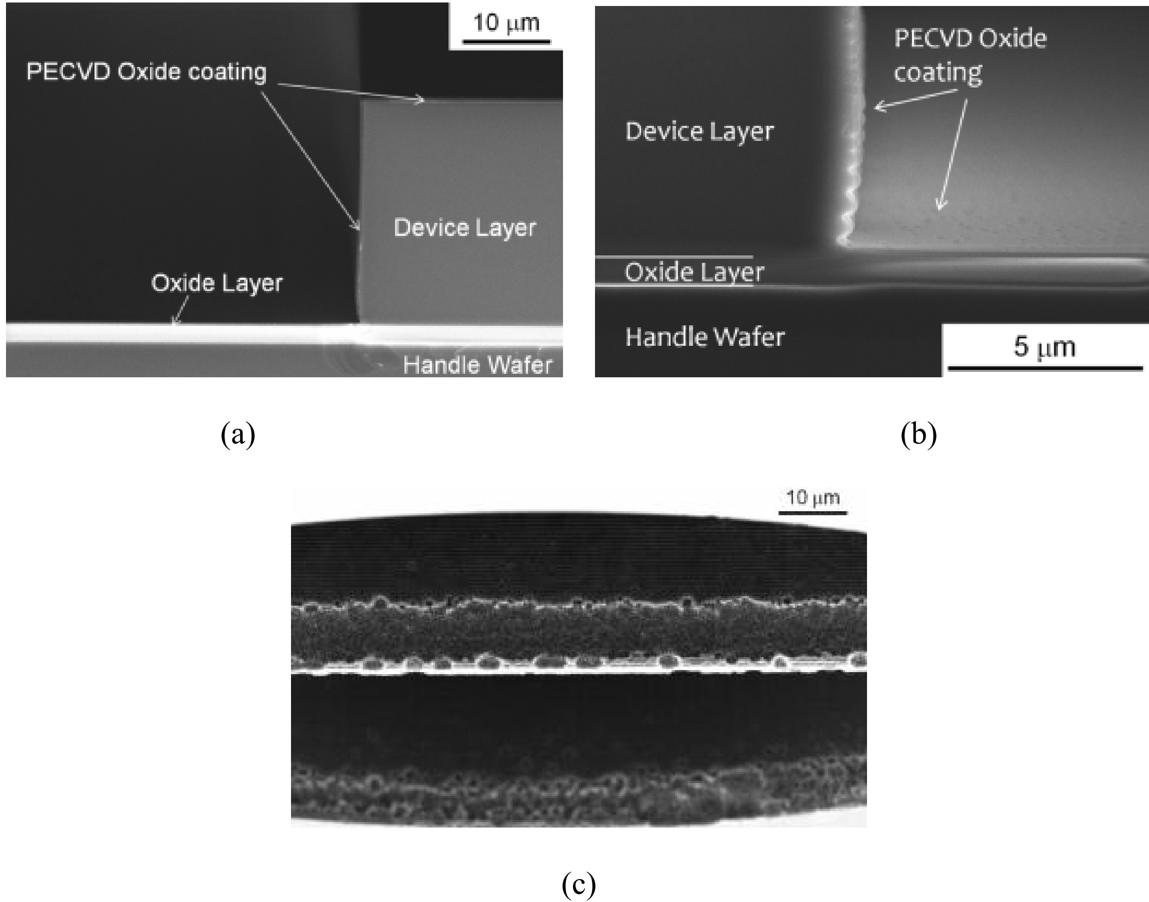

Figure 2.19: PECVD silicon dioxide coating on SOI wafer and fabrication results (a) The PECVD silicon dioxide produces a conformal coating covering the scalloped surface from the front side etch. (b) A more magnified view of the same result showing that the silicon dioxide layer is conformal at the device layer and buried oxide interface of the SOI wafer. (c) The front side surface after using this process as a front side protective layer; clearly, this oxide was unable to protect the front side etch from the unintended etching when the oxide cracks. The view is of a theta web region at an oblique angle on the side that was adjoined to the buried oxide layer of the SOI.

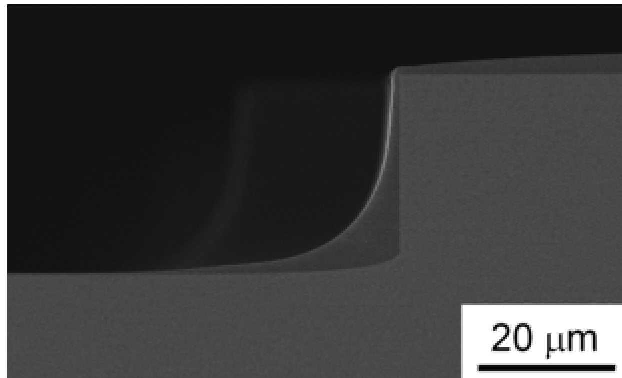

(a)

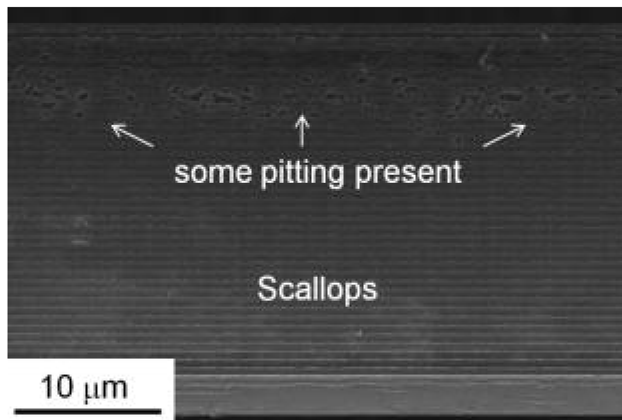

(b)

Figure 2.20: Spin coating front side protection results. (a) The photoresist is thin in areas and does not fill in the etched features. (b) Some pitting-like damage observed when this process is used.

The approach that did not allow the oxide layer to break and consequently protected the front side etch surface was the use of a spray coating of photoresist (MicroSpray, MicroChem, Newton, MA). The oxide breakage protection provided by this coating is shown in Figure 2.21. For the most part the oxide layer did not crack as in Figure 2.21(a), and when the oxide layer did crack as in Figure 2.21(b) the oxide did not break out. This resist layer was effective at supporting the compressive stress in the SOI oxide layer; far less cracking was observed near samples and using these changes produced samples without the unintended secondary etch behavior.

2.7 Batch Etch Results

Resulting Durelli and arch theta samples are shown in Figure 2.22(a) and (b), respectively. As can be seen in Figure 2.22, test strip material near the left and right sides of samples and just below the top level of the sample was included in the design to protect samples from any unintended damage during handling. Finally, each test strip, consisting of 10 theta samples spaced along a 15 mm length, was removed from the wafer using a diamond scribe on notched regions at each end of the strip. Figure 2.23 shows the relative size change from first generation to second generation samples [Figure 2.23(a)] and the robustness of the second generation sample test strip [Figure 2.23(b)]. This test strip design enables easy manipulation and testing of very small samples by including the samples on a much larger test strip, which the investigator can handle with little difficulty.

Figure 2.24 features examples of the fabricated sample cross-sections for each batch performed. For the small scallop and large scallop Bosch DRIE samples in

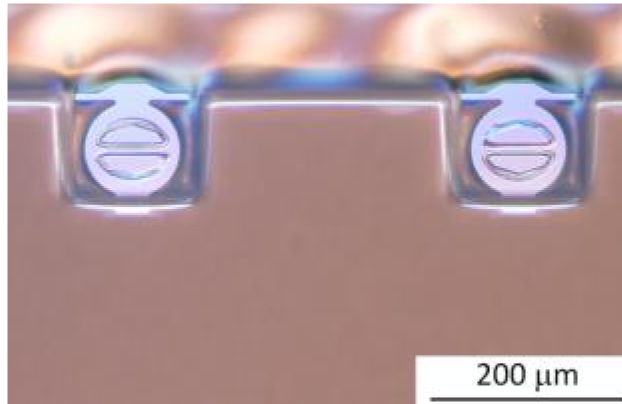

(a)

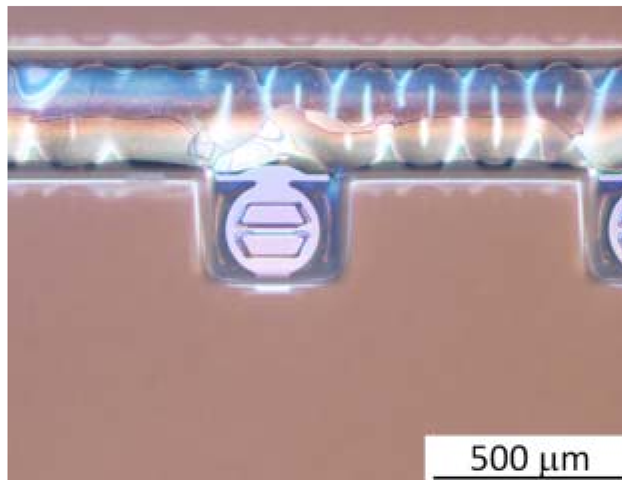

(b)

Figure 2.21: The spray coating effect on the oxide layer damage problem during the back side etch. (a) No cracking observed around or above the samples. (b) Cracking of the oxide is present though no oxide broke out from the layer.

(a)

(b)

Figure 2.22: Field-emission scanning electron microscopy (FESEM) images of completed (a) Durelli and (b) arch theta test samples.

(a)

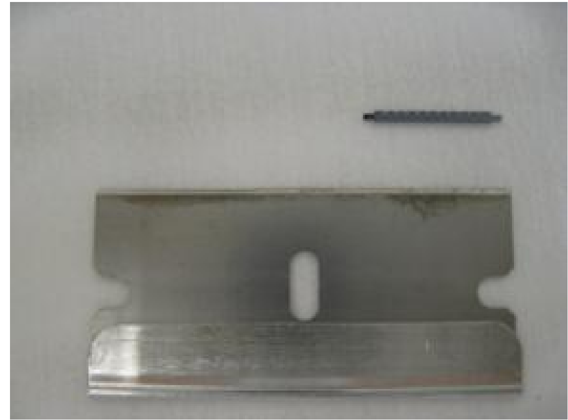

(b)

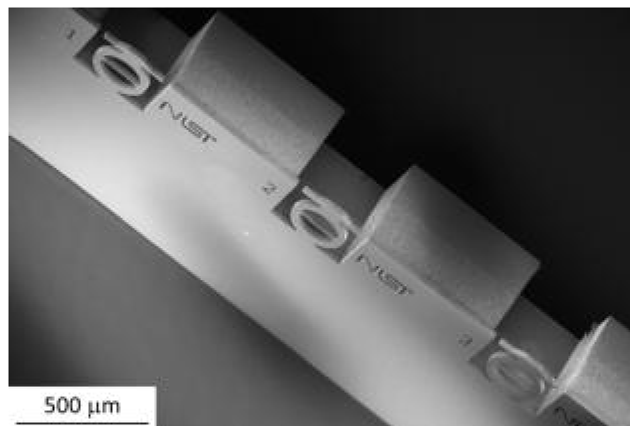

(c)

Figure 2.23: (a) Relative size comparison of the first generation (top) and second generation (bottom) test strips. (b) Second generation sample test strip next to a standard razor blade. (c) Oblique view of the second generation sample test strip.

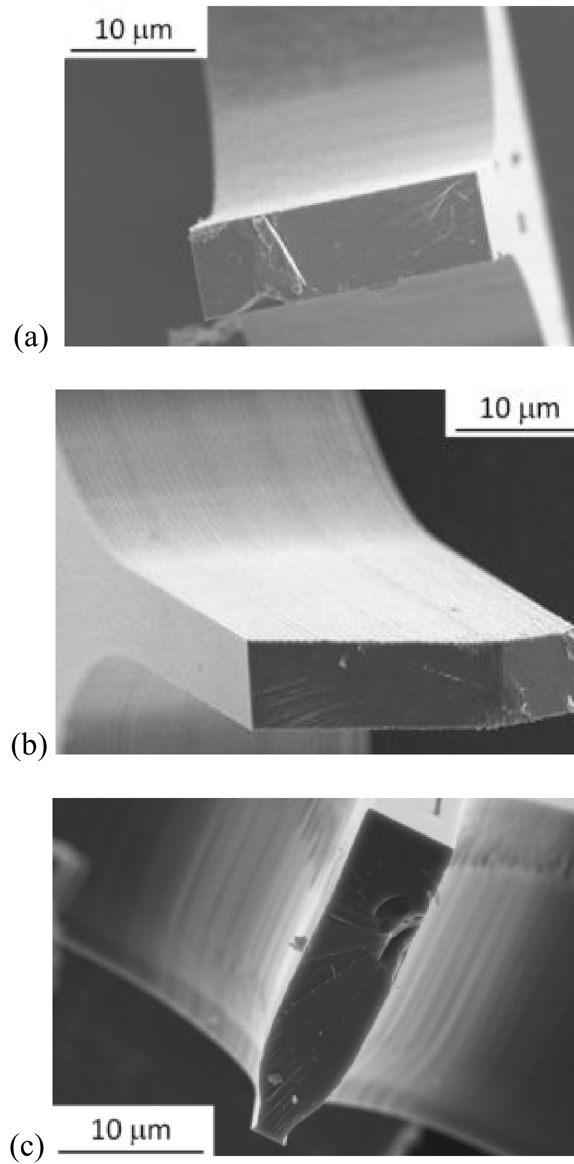

Figure 2.24: FESEM images of the through-the-web cross-section of resulting (a) first, (b) second, and (c) third batches of second generation samples. In (a) and (b) the cross-sections of the Bosch DRIE samples maintain a constant thickness. In (c) the sample front is the top of the image. The narrowing at the back of the cryogenic DRIE sample is due to the SOI notching effect)

Figure 2.24(a) and (b), respectively, the cross-sections maintain a nearly constant sidewall profile with a sidewall angle of less than 0.5° from vertical. The cross-section of the cryogenic DRIE sample in Figure 2.24(c) also maintains a constant nearly constant sidewall profile through most of the sample etch, however there is a narrowing apparent resulting at the end of the front side etch. This narrowing is due to the SOI notching effect, a common result in SOI processing [Jansen *et al.*, 1995; Walker, 2001; Chekurov *et al.*, 2007] that is sometimes difficult to avoid. For the Bosch processed wafers no SOI notching effects were observed, having been successfully avoided with the developed Bosch recipe. However, the developed recipe for cryogenic DRIE was not sufficiently optimized to avoid the SOI notching effect; to perform this optimization would require several SOI wafers to be used in a similar way that the aforementioned test wafer were used, which would be very costly. The notching of the web region did not appear to affect the sample testing results (see Ch. 7).

The first batch of second generation samples exhibited two forms of surface etching, shown in Figure 2.25. The etch quality in Figure 2.25(b) is consistent with the regular etch steps known as scallops that are characteristic of DRIE. However, in Figure 2.25(c) a clearly different etch surface quality is apparent. The effect of this unintended etch surface, in the form of irregular pits, is discussed in Ch. 6. The second and third batches were fabricated by a larger scallop Bosch DRIE and the developed cryogenic DRIE process, respectively. The resulting etch surface finishes are shown in Figure 2.26 with a view such as that indicated in Figure 2.25(a). The scallop-etched sample in Figure 2.26(a) clearly has a set of relatively larger scallops across the web region [note the scale difference between Figure 2.26(a) and Figure 2.25(b)]. The cryogenic DRIE sample

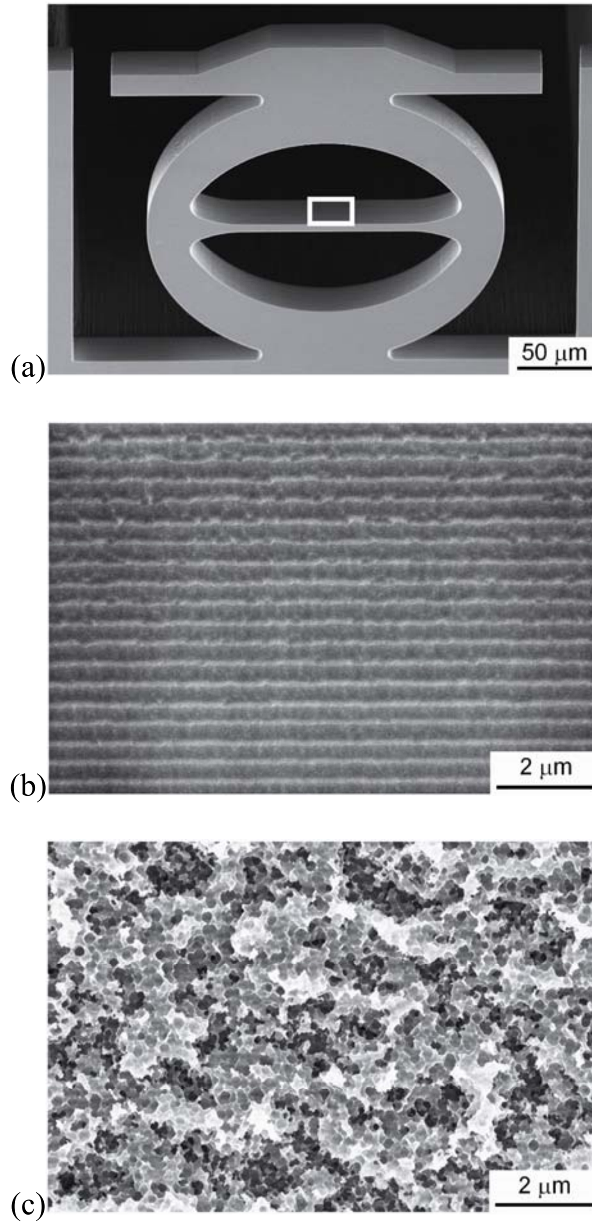

Figure 2.25: FESEM images of the sidewall etch surfaces for the theta test samples. A portion of the important web segment is indicated by the box in the tilted theta sample of (a). In (b), the sidewalls have regular etch features, known as "scallops", which are expected with the DRIE process. In (c), the sidewalls have irregular etch features, denoted here as "pits", which result from unwanted etching of the Si device layer during the etching of the Si handle wafer.

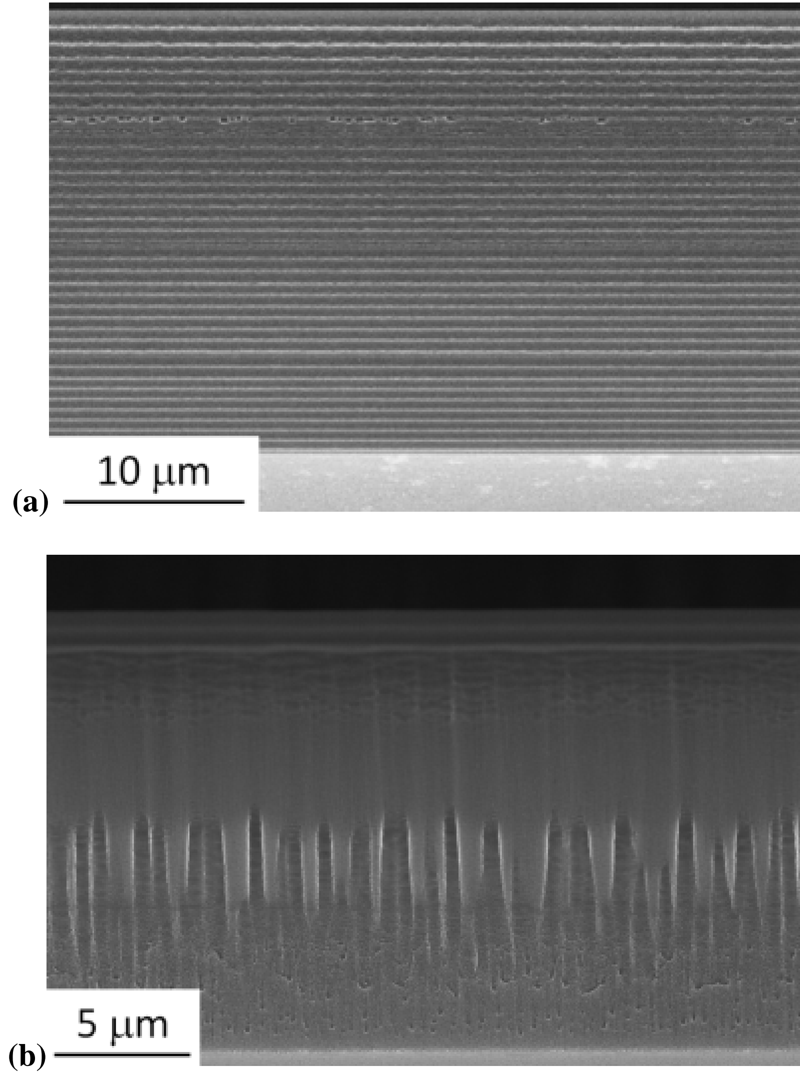

Figure 2.26: FESEM image of the etch surface of the web region (tilted) for a (a) second batch of Bosch DRIE sample and (b) a cryogenic DRIE batch sample. The front of the samples is toward the bottom of the images.

surface in Figure 2.26(b) has a smooth surface in regions, however the surface a rough-stepped region near the center of the sample. This is due to deterioration of the photoresist mask edges during the etch process that exposes new silicon to etch. During the process development for the cryogenic DRIE samples other mask option were explored, however other mask options, such as an oxide mask, compounded with the poor electrical conduction of the SOI wafer, led to inconsistent etch results. Using a photoresist mask was the best approach. The characterization of each batches resulting etch surface is covered in Ch. 3. The effect of these processing surface finishes on strength is discussed in Ch. 6.

2.8 Mechanical Testing Methodology

Fabricated samples were mounted in an aluminum puck [Figure 2.27(a)] that was designed to be installed in a conventional IIT sample stage [Figure 2.27(b)]. The test strips were clamped across the full-wafer 427-μm thickness into this fixture (separately) that was then mounted into an IIT device (Nano Indenter XP, MTS Systems Corporation, Eden Prairie, MN), such that the samples were upright and isolated from the surrounding clamp material. Each test required to determine the appropriate indenter velocity in order to effectively detect sample failure without setting the indenter velocity too low as to have false detections; this was especially sample was then diametrally compressed *via* IIT using a 500-μm diameter spherical sapphire indenter tip [Figure 2.27(c)] (Micro Star Technologies, Huntsville, TX) and an IIT break-detection routine, developed within the instrument software (Testworks v.4.10A, MTS Systems Corporation, Eden Prairie, MN), that withdrew the indenter on detection of sample failure to minimize subsequent sample

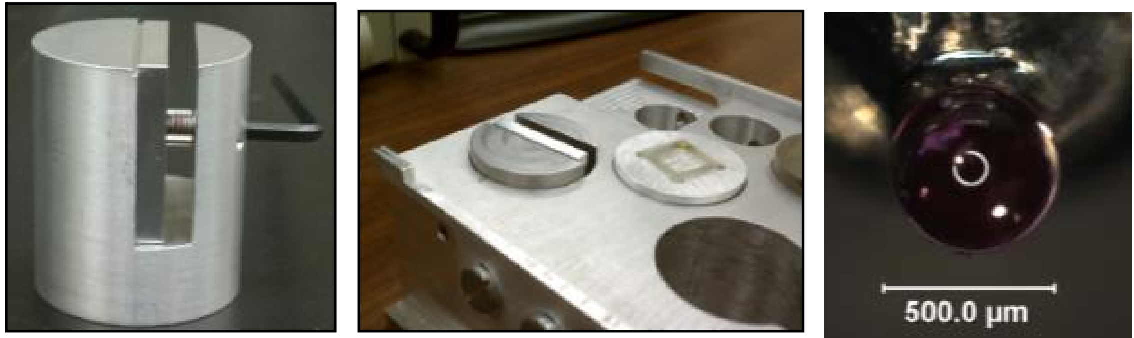

(a) (b) (c)

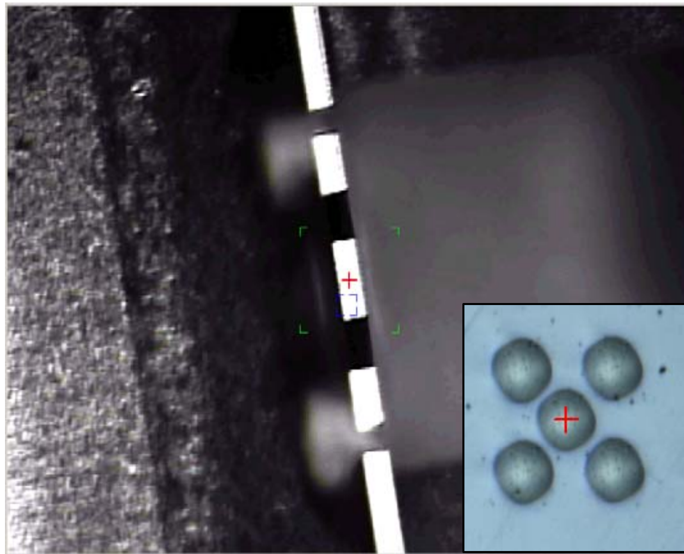

(d)

Figure 2.27: (a) The sample mounting puck for the second generation samples. The samples go into the top slot of the puck and clamped by a pusher plate. (b) The mounting puck installed into an instrumented indenter stage. (c) The 500-μm diameter sapphire spherical indenter used for testing samples. (d) The camera view of the test sample load-point selection. (Inset) Five-indentation cross-pattern used to calibrate the indentation tip to the microscope. The cross-pattern is about 100 μm across.

damage. Development of the break detection routine was important at higher indentation loads as this entered the high-load regime of the indentation system where a second loading mechanism engaged that produces an increase in load-displacement noise (see Ch. 6). The sample load-point location was selected as shown in Figure 2.27(d) with the red crosshair directly over the center point of the sample tophat. The microscope-indenter calibration was performed using a five-indentation cross pattern, an example of which is shown in the inset in Figure 2.27(d). After the indenter performs the five indentations and returns the camera to the indentation location the center of the indentation was selected by placing the red crosshair in the center of the central indentation as shown in Figure 2.27(d). The accuracy of the load-point selection is estimated to be within 1 μm.

Two sets of test conditions were used for the first batch of second generation theta samples. In the first, the IIT device was operated in load control and set to load to a peak load of 200 mN, cycle five times between the peak load and 100 mN with a 30 s peak hold each cycle, and then unload, using loading and unloading rates progressively increasing from 0.5 mN s^{-1} to 13.3 mN s^{-1}. In the second, the IIT device was subsequently operated at a target displacement rate of 20 nm s^{-1} and loaded until the break-detection routine detected a rapid increase in indenter velocity, associated with an increase in sample compliance and sample failure, and withdrew the indenter. Load and displacement were recorded throughout the cyclic loading and sample failure measurements with data acquisition rates of 5 Hz and 100 Hz, respectively. For the second and third batches of theta samples the two above test conditions were combined into a single procedure to perform the complete sample test in one run without withdrawing the indenter tip from sample contact. The cyclic peak load and unload

values were decreased to 50 mN and nearly 0 mN, respectively, for the C-ring samples, and 250 mN and nearly 0 mN, respectively, for the gapped-theta samples.

Sample load and displacement data were converted into the longitudinal stress, σ, and strain, ε, in the web using finite element analyses (see Ch. 4); in particular, sample strength, σ_f, was calculated from the peak load at sample failure and the sample web dimensions (see Ch. 3).

2.9 *Summary*

The second generation strength test samples have been fabricated from an optimized fabrication sequence using optimized specimen and test strip designs. The processing-structure relationship was developed for chosen MEMS-relevant processing techniques focusing on the effects of the processing on the sample sidewall profile and structure and overall sample cross-sectional geometry. A cryogenic DRIE fabrication recipe was developed specifically for the second generation designs. Various aspects of the fabrication process required significant development. The fabricated samples are mounted and tested in IIT using a developed routine capable of detecting sample failure.

Chapter 3: Microscopy and Imaging

In this chapter the processing-structure relationship of the fabricated samples are examined at both nano- and micro-scales. At the nano-scale, atomic force microscopy (AFM) is used to characterize the etched surfaces of all the fabricated sample sets used for strength testing, including first generation theta samples. At the micro-scale, the web width of each fabricated theta sample was determined using an image processing routine.

3.1 Surface Roughness Characterization

Topography measurements of the resulting etch surfaces were analyzed with AFM (Nanoscope, Digital Instruments/Veeco Metrology Group, Plainview, NY) to characterize surface roughness. Intermittent contact mode AFM, at a line scan rate of 1 Hz, was used to scan five μm by five μm sample sidewall surfaces for each fabricated sample set, including the first generation samples, using cantilevers (TAP300 AFM Probes, Bruker, Camarillo, CA) with a 40 N m^{-1} spring constant, 325 kHz resonance frequency, and 10 nm tip radius. Each scan contains 512 pixels by 512 pixels.

Etched surfaces are generally not smooth but have a roughness associated with the surface. An example of this roughness can be seen in Figure 3.1, in which AFM images and topographic lines scans along the tensile loading direction are presented of a DRIE scallop surface [Figure 3.1(a)] and a pitted surface [Figure 3.1(b)] from the batch A of second generation samples. The AFM images appear similar to the FESEM images of the etched surfaces presented in Ch. 2 [Figs. 2.10(b) and (c)]. These surfaces have very

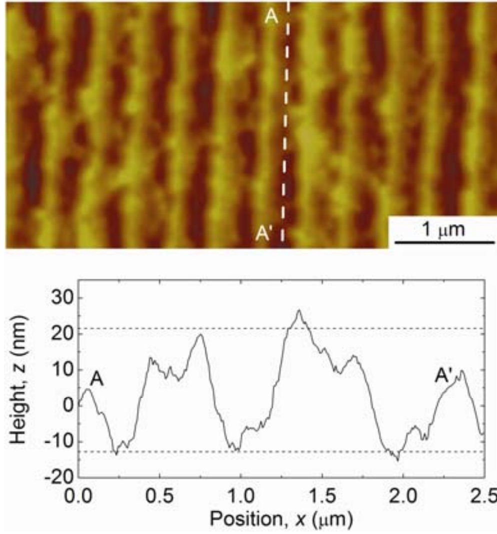

(a)

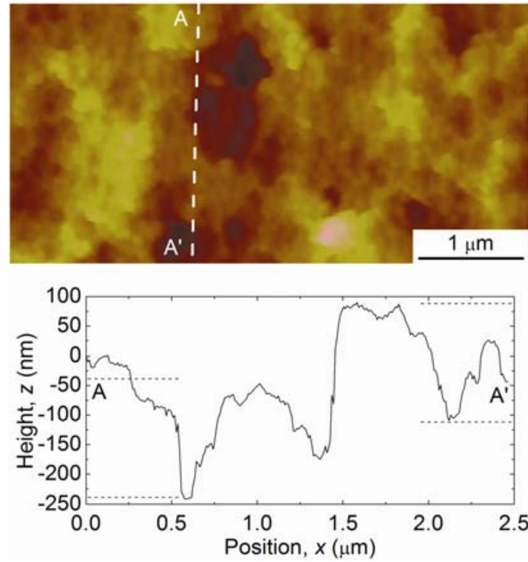

(b)

Figure 3.1: AFM images and line-scans of sidewall etch surfaces of the batch A of second generation with (a) scallops and (b) pits. The maximum perturbations along the length of the scallops and pits are denoted by dashed lines in the respective line-scans.

different topographical features; the line scans across the selected AA’ segments of the AFM images in Figure 3.1 illustrates this difference. The peak-to-valley height difference, indicated by the pairs of horizontal dashed lines in each line scan, is much greater across the pitting etch sample surface in Figure 3.1(b) than the DRIE scallop sample surface in Figure 3.1(a). The peak-to-valley topography of the DRIE scallop surface [Figure 3.1(a)] along the loading direction parallel to the scallops was approximately 30 nm. The peak-to-valley topography of the pitted surface [Figure 3.1(b)] along the loading direction was approximately 250 nm, although the valley base level was much more irregular than that observed for the scalloped surface to give surface features approximately 150 nm in scale.

The strengths of fabricated samples or device components are commonly limited by the surface roughness created during the fabrication process. When the sample (or device component) is under enough stress, the surface microstructure of, for instance, an etch surface, will induce a stress concentration at a particularly potent surface feature and induce fracture. In order to assess the effects of a particular processing method on the strength of samples it is necessary to measure and characterize the surface roughness of the samples of interest.

A rough surface measured with AFM is typically analyzed by statistical methods. The AFM data is represented as a height distribution function $h(x_i, y_i)$, where x_i and y_i are pixel coordinates and h is the relative vertical height of the surface. A common method of characterizing the height distribution of a surface is by means of the root-mean-squared roughness

$$R_{\text{rms}} = \sqrt{\left\langle \left[h\left(x_{\text{i}}, y_{\text{i}}\right) - \langle h \rangle \right]^2 \right\rangle}\,, \qquad (3.1)$$

where < > denotes an average (and <h> is the average height of the scan) [Dotto and Kleinke, 2002]. The R_{rms} is only a measure of how the heights vary across the surface independent of how the lateral distribution of the heights may depend on one another; it simply reveals how rough the surface is. In order to understand how the processing method affected the strength of samples it is necessary to know something about the shape and regularity of surface features. R_{rms} does not give information about the structure or pattern of the surface in the lateral directions; it does not reveal how the surface is correlated laterally. Furthermore, surfaces with identical root-mean-squared surface roughness can have very different appearances and result in different mechanical behavior.

Surfaces typically exhibit two basic types of overall structures, both of which are of a fractal nature [Barabasi and Stanley, 1995]. When a surface in nature is observed at different scales and looks the same, the surface is *self-similar* fractal. A self-similar surface means that if the surface is scaled by the same factor in all directions, the surface will be statistically the same before and after the scaling. This is not usually the case. In many cases, scaling by the same factor in all dimensions will never result in a statistically identical surface; however, for these other type of surface structures, a scaling that is different for *each* direction can result in a statistically identical surface. A surface with this type of structure is known as *self-affine* fractal. Examples of self-affine fractal surfaces are found in many areas of nature, some of which are biological systems such as bacteria growth [Barabasi and Stanley, 1995], and surfaces such as asphalt and concrete

road surfaces [Persson *et al.*, 2005]. A surface that cannot be repeated with either type of scaling is not fractal.

In order to understand the roughness nature of the particular processing method used, it is necessary to understand how the surface features are correlated laterally and how scaling affects the surface. This requires a robust analysis technique such as the surface roughness power spectrum, $C(q)$, where q is the wavenumber of the spectrum. The two-dimensional power spectrum or power spectral density (PSD) function is defined as the Fourier transform of the height autocorrelation function

$$C(q) = \frac{1}{(2\pi)^2} \int \mathrm{d}^2\mathbf{x} \langle h(\mathbf{x}) h(\mathbf{0}) \rangle \mathrm{e}^{-\mathrm{i}\mathbf{q}\cdot\mathbf{x}} \ . \tag{3.2}$$

where $\langle h(\mathbf{x}) h(\mathbf{0}) \rangle$ is the height autocorrelation function, and $\mathbf{x}$ is (x_i, y_i) [Persson *et al.*, 2005]. Analysis of power spectrum plots of $\log[C(q)]$–$\log(q)$ typically reveals a linear region over a range of wavenumbers. The slope of this linear region is used to determine the fractal nature and the corresponding fractal dimension of a particular surface. In this linear region the power spectrum has a power-law behavior of

$$C(q) \sim q^{-2(H+1)} \tag{3.3}$$

where H is the Hurst or scaling exponent [Persson *et al.*, 2005]. For a self-similar fractal surface $H = 1$, while a self-affine fractal surface will have a Hurst exponent between 0 and 1. If the Hurst exponent is greater than 1, the surface is not fractal. The fractal dimension, D_f, can be determined from the relationship

$$D_f = 3 - H \ . \tag{3.4}$$

For self-similar and self-affine fractal surfaces, D_f will have a value of 2 to 3, respectively.

The first generation round and hexagonal theta samples [Quinn *et al.*, 2005; Quinn, 2009], as well as all three batches of second generation theta samples, were analyzed to measure the R_{rms} and PSD of each set of samples. These results are shown in Figure 3.2 to Figure 3.5. In each figure the 5 μm by 5 μm AFM scan is shown on the left and the corresponding power spectrum on the right. The round and hexagonal first generation samples are examined in Figure 3.2(a) and (b), respectively. The scallop and pitting samples from the first batch of second generation samples (batch A) are examined in Figure 3.3(a) and (b), respectively. The surface of a second batch (batch B) second generation sample is examined in Figure 3.4. Figure 3.5 examines two different regions of the third batch (batch C) of second generation samples; this sample, fabricated with cryogenic DRIE exhibit two surface finishes, one with a smoother dimple-type surface [Figure 3.5(a)] and the other with a rougher etch that resulted from photo-mask edge damage during etching [Figure 3.5(b)]. The largest R_{rms} was observed in the first generation samples [Figure 3.2(a) and (b)], batch A pits [Figure 3.3(b)], and batch C etch (resulting from the photo-mask edge damage) [Figure 3.5(b)] with approximately 10 nm difference in R_{rms} across these samples. The batch A scallop [Figure 3.3(a)] and batch C [Figure 3.5(a)] samples had much lower nearly identical R_{rms}, while the batch B sample (Figure 3.4) had a R_{rms} about mid-way between these two groups. Each power spectrum had a linear region ($\log[q] > -2$) and linear fits in log-log space produced good fits. The slopes of these fits were used to determine a Hurst exponent and each of the scallop samples [Figure 3.2, Figure 3.3(a), and Figure 3.4] had Hurst exponents near 1 corresponding to a nearly self-similar fractal surface. The other etch surfaces [Figure 3.3(b) and Figure 3.5] had Hurst exponents much greater than 1 which indicates that

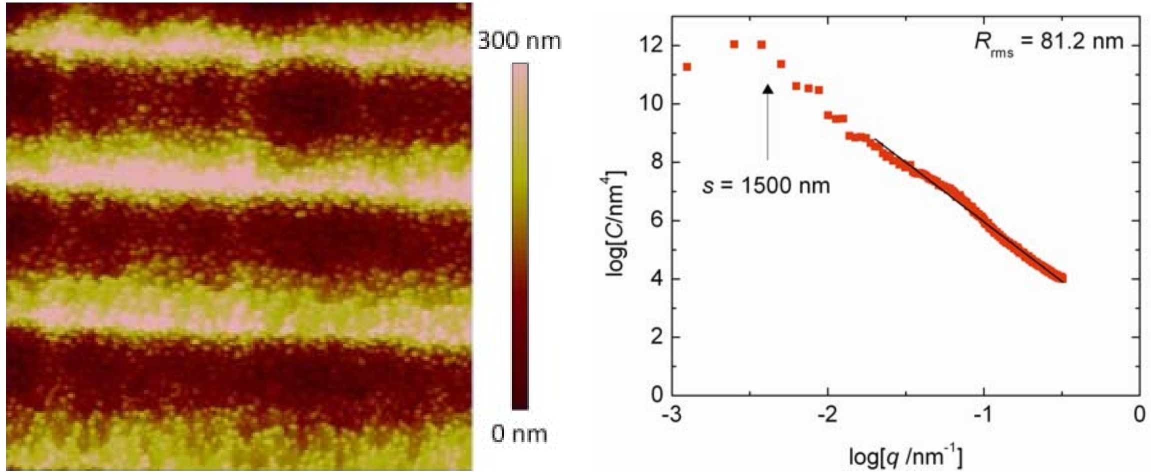

(a)

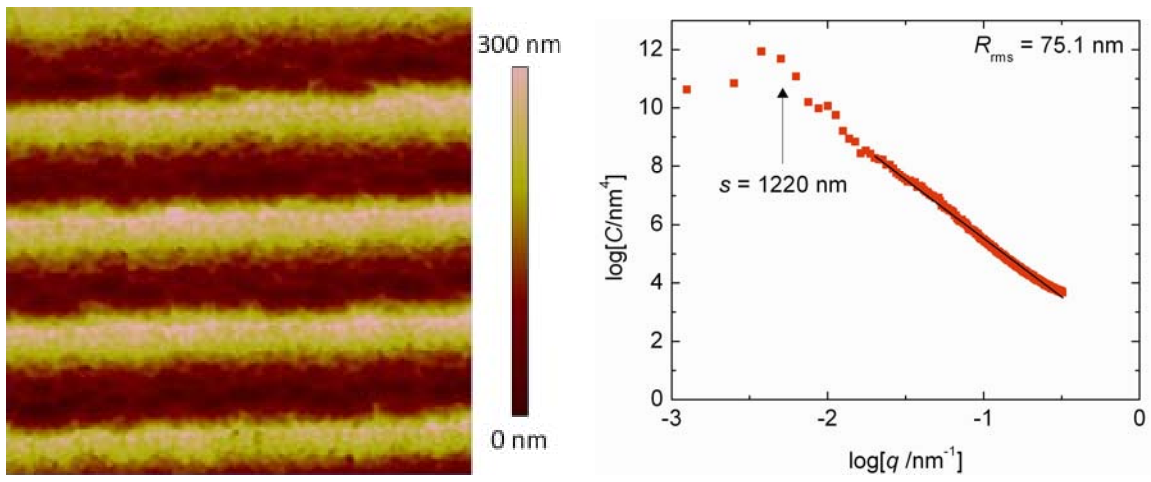

(b)

Figure 3.2: AFM scan and power spectral density plot of the (a) round and (b) hexagonal first generation theta samples. The expected scallop wavelength location on the power spectrum is indicated by the arrow and is good agreement with the peaks present in the power spectrum.

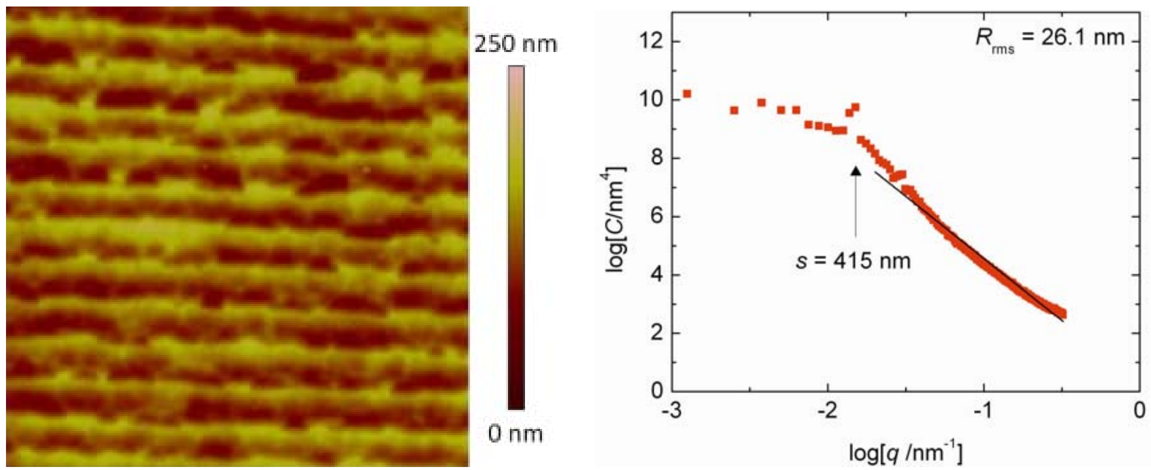

(a)

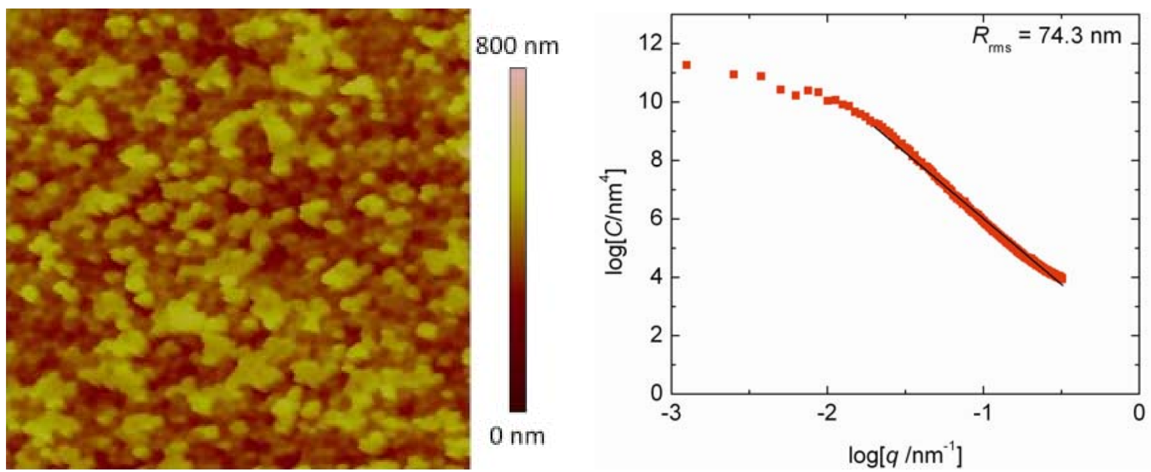

(b)

Figure 3.3: AFM scan and power spectral density plot for the generation II batch A samples: (a) scallops, (b) pitting etch. The expected scallop wavelength location on the power spectrum is indicated by the arrow in (a) and is good agreement with the peaks present in the power spectrum.

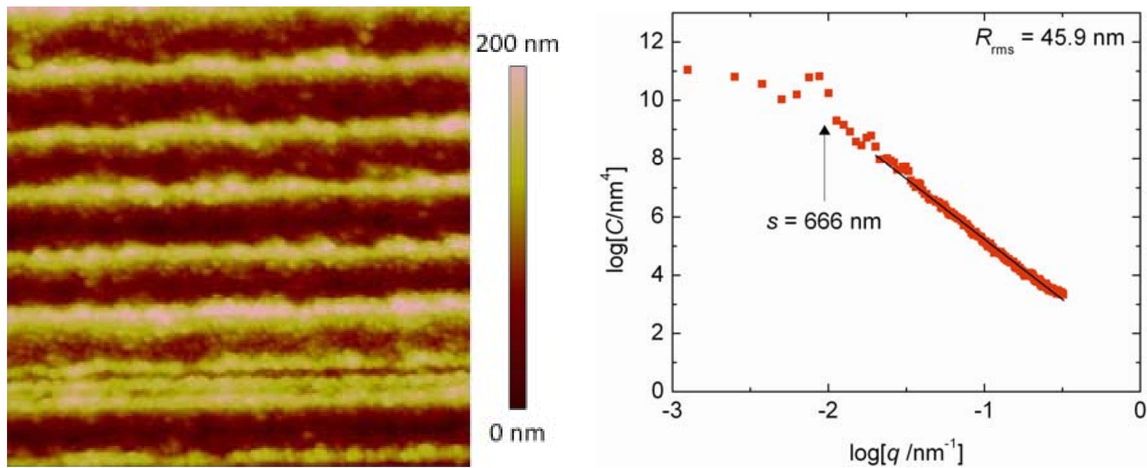

Figure 3.4: AFM scan and corresponding two-dimensional power spectral density plot of the second generation B batch theta samples. The expected scallop wavelength location on the power spectrum is indicated by the arrow and is good agreement with the peaks present in the power spectrum.

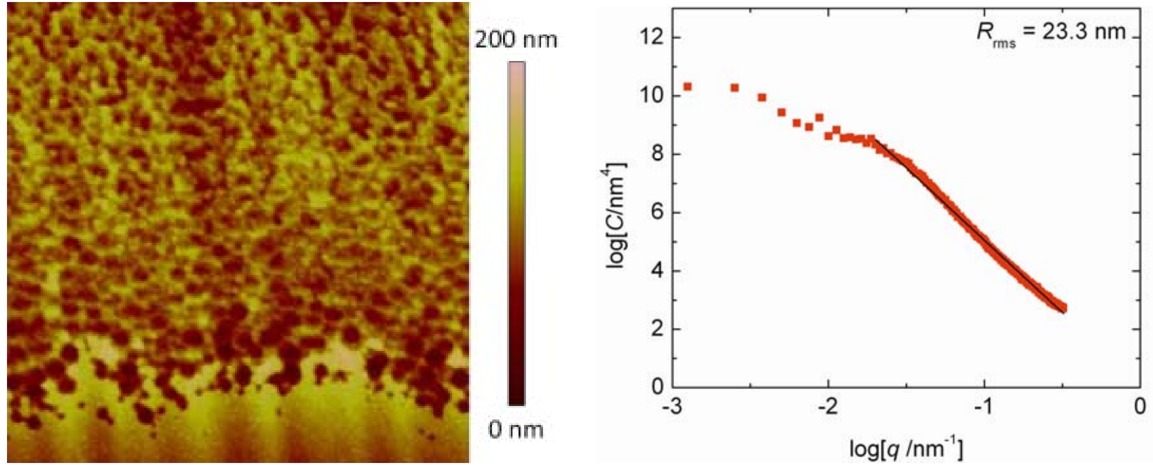

(a)

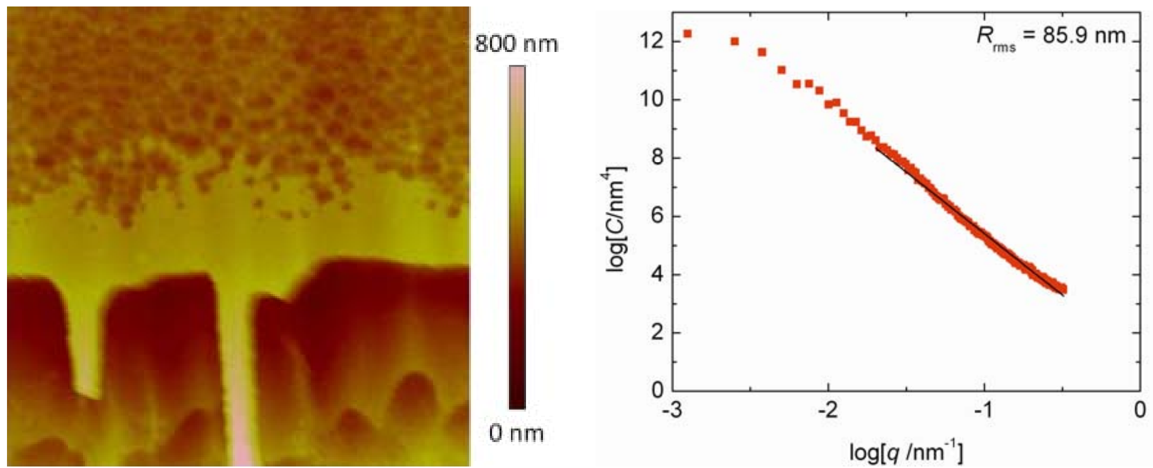

(b)

Figure 3.5: AFM scan and corresponding two-dimensional power spectral density plot of the second generation C batch theta samples. These samples were etched with cryogenic DRIE where (a) features a region similar to the anticipated surface roughness with a smooth region and some dimpling damage, and (b) includes a significantly larger damaged sidewall structure on the etched surface that will be discussed in Ch 7.

these surfaces were not fractal at any scale. In each of the scallop samples [Figure 3.2, Figure 3.3(a), and Figure 3.4] the regular scallop pitch size, s, is determined from the AFM scan and indicated with an arrow on the power spectrum. For each of these cases the location of the scallops q_s, determined by the relation $q_s = (2\pi)/s$, is in good agreement with the location of a peak in the power spectrum.

These results are organized in Table 3.1. Sample sets fabricated with Bosch DRIE broadly have Hurst exponents near 1 corresponding to nearly self-similar fractal surfaces. A diagram illustrating how this self-similar fractal-like nature would look on the scallop surface is shown in Figure 3.6. The size of the fractal-like structure is exaggerated to make it clear. The surface has controlled and uncontrolled aspects. The controlled aspect corresponds to the larger scale scalloping nature (black) of the developed Bosch DRIE recipes that produces the overall anisotropic etch profile. The uncontrolled aspect corresponds to the smaller scale isotropic etching (red) that occurred during the formation of each scallop in the process loops of Bosch DRIE. This isotropic etching produced the nearly self-similar fractal surface; if the isotropic etching were allowed to proceed for an extended period of time the surface should exhibit a fractal nature.

The pits in the batch A samples and the two cryogenic DRIE surfaces examined do not appear to have a fractal nature. Other etched surfaces have been examined in the literature, and scaling exponent values corresponding to self-affine [Dotto and Kleinke, 2002] and nearly self-similar [Zhao *et al.*, 1999] surfaces have been observed. Deposition techniques also produce rough surfaces that are self-affine [Yang *et al.*, 1993; Aue and DeHosson, 1997; Zhao *et al.*, 2000] and self-similar [Yang *et al.*, 1997] as well a potentially non-fractal [Mohanty *et al.*, 2009] surface.

Table 3.1: AFM statistical data for each of the fabricated batches of theta samples including the round and hexagonal batches fabricated as part of the initial generation of thetas.

Batch Set	R_{rms} (nm)	PSD Slope	Hurst Exponent, H	Scallop Pitch, s (nm)
Generation I Round	81.2	4.07 ± 0.02	1.04	1500
Generation I Hexagonal	75.1	4.03 ± 0.02	1.01	1220
Generation II.A Scallops	26.1	4.25 ± 0.04	1.13	415
Generation II.A Pits	74.3	4.50 ± 0.02	1.25	---
Generation II.B	45.9	4.13 ± 0.02	1.07	666
Generation II.C Dimples	23.3	4.95 ± 0.02	1.48	---
Generation II.C All	85.9	4.21 ± 0.03	1.11	---

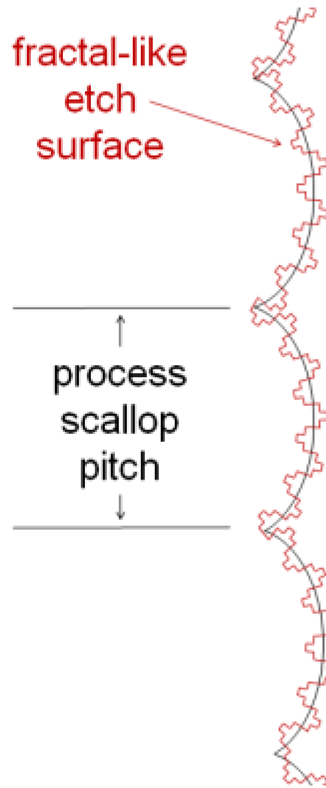

Figure 3.6: A simple diagram of a “self-similar fractal”-like surface resulting from the Bosch DRIE process. The scallop pitch, shown in black, is set by the particular Bosch DRIE recipe used to etch the surface. The result of a nearly self-similar fractal-like surface, shown in red (and at a much larger scale than it would actually exist), is due to the nature of the isotropic etching step in the BOSCH DRIE process.

3.2 Web Width Determination

The dimensions of the web cross section in the theta specimens are critical in determining the relationships between the load applied to the sample, P, and stress, σ, generated in the web, and the load-point displacement, h, and web strain, ε. The dimension of the web in the section AA′ in Figure 3.7(a), the web *width*, w, controlled the P-σ and h-ε relationships (see Ch. 4), as the sample and web thickness were controlled by the SOI device layer thickness; lithographic and DRIE variability generated variations in web width but not web thickness. High-contrast optical microscope images were digitally recorded for every theta sample, as shown in the example Figure 3.7(a). The images were imported into an image processing program (IGOR Pro v.6.1.0.9, WaveMetrics Inc., Lake Oswego, OR) and the image intensity variation across hundreds of sections such as AA′ determined over the central section of the web. An example of an intensity variation is shown in Figure 3.7(b). The minimum and maximum intensity in an image were then used to set a half-maximum intensity variation and a web dimension at each section was defined as the full-width at half maximum (FWHM) of the intensity variation. The web dimensions from every section in an image were then combined to generate a mean and standard deviation web dimension in pixels for that sample. Such over-sampling enabled super-resolution sub-pixel standard deviations to be obtained for the web widths. (Details of the image processing routine are presented in the Appendix.) Calibration of the microscope and image processing program using a calibrated pitch grating enabled the web width in micrometers to be calculated from the pixel dimensions. Figure 3.8(c) shows histograms of the web widths of the 105 fabricated and tested Durelli and arch

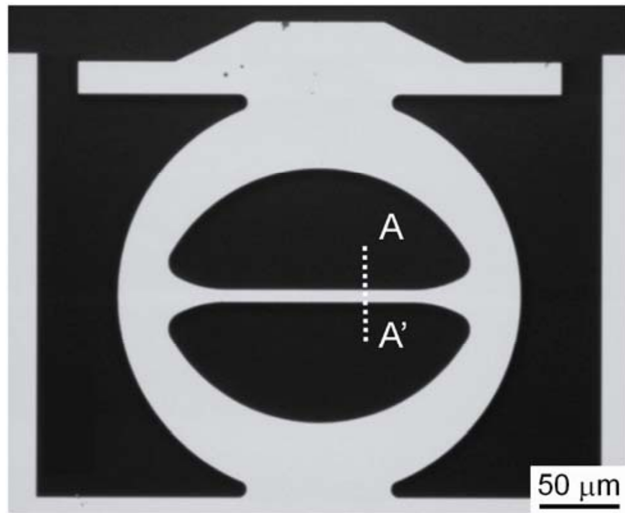

(a)

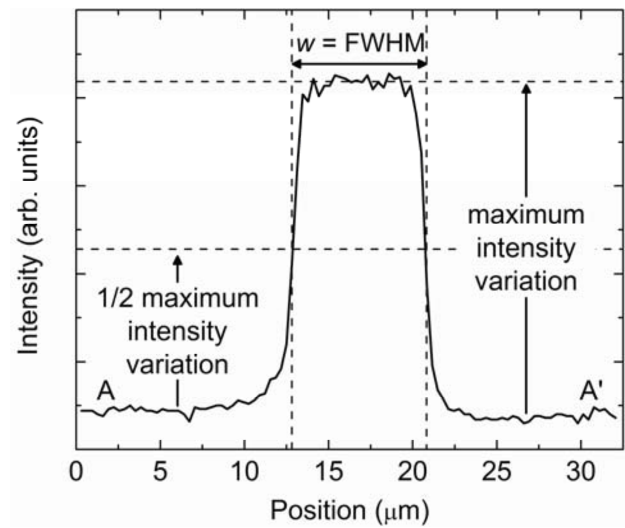

(b)

Figure 3.7: (a) Grayscale optical image of an arch theta test sample. An optical image of each sample was imported into an image processing routine prior to testing. (b) Vertical line scans of the pixel intensity were analyzed using a full-width half-maximum (FWHM) criteria to determine the web width. The web widths from these line scans were averaged over the entire web segment, resulting in sub-pixel resolution for *w*.

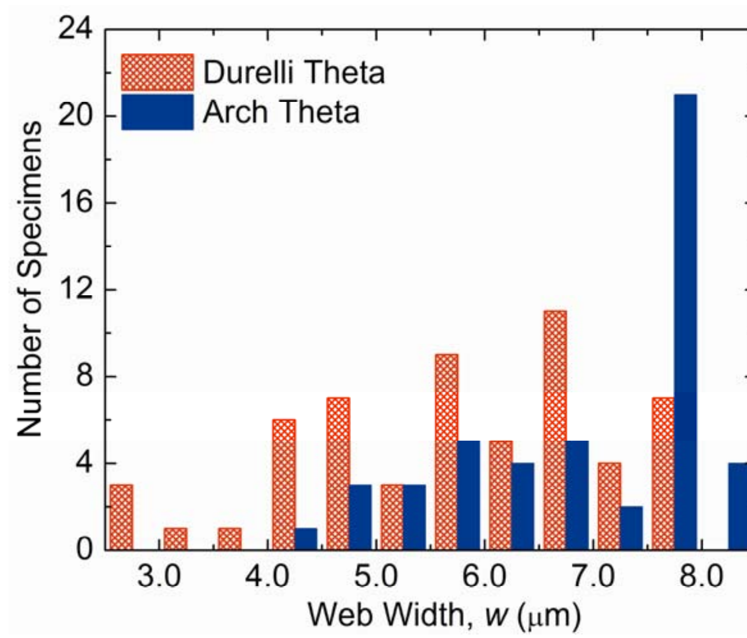

Figure 3.8: Histograms of the web width distribution for Durelli and arch theta samples at 0.5 μm intervals.

theta samples from the first batch of second generation samples. Note that most samples had web widths less than the target of 8 μm. Trials of the lithographic process showed that the variability in web width resulting from the intended DRIE process was 0.7 μm and hence some other, unintended, process over-etched the samples to generate significantly smaller web widths as was discussed in Ch. 2.

Resulting samples from the first batch had web widths from 2.65 μm to 8.17 μm with web width standard deviation in the range of 0.02 μm to 0.40 μm. After making the changes in the mask design and the fabrication sequence discussed in Ch. 2, the second and third batches had more narrow distributions better aligned with lithographic testing variability of 0.7 μm. The second batch of the tested 198 samples had web widths from 6.83 μm to 7.35 μm with web width standard deviation ranging from 0.01 μm to 0.03 μm, and the third batch of the tested 209 samples had web widths from 6.72 μm to 7.16 μm with web width standard deviation ranging from 0.01 μm to 0.06 μm. The use of the measured web widths will be discussed in Ch. 4.

Images were also captured prior to the testing of C-ring and gapped-arch theta samples. All captured images were examined to confirm that the resulting samples had the correct dimension and samples that failed to be fabricated correctly were eliminated. In some cases, an error occurred during the fabrication, such as an air bubble in the lithography step, which affected the sample geometry in such a way to make the test specimen invalid. These samples were ruled out from testing.

An image processing routine was not used in the translation of the load-displacement behavior of the C-ring and gapped-arch theta sample, as is performed for

the Durelli and arch theta samples in Ch. 4. Only the second batch of the second generation C-ring and gapped-arch theta samples, which only had a 0.5 μm dimensional variation across the sample set, were tested. The dimensions of the C-ring and gapped-arch theta specimens have less critical dimensions than the Durelli and arch theta specimens.

3.3 Summary

AFM and optical microscopy has been used to develop processing-structure relationships for the fabricated theta samples. Web width determination showed a wide distribution in web widths for the batch A samples resulting from the uncontrolled etching problem and narrow distributions for the batch B and C samples where this etching problem had been resolved. AFM topographical analysis revealed varied sample surface roughness for the Bosch DRIE samples with the large surface roughness resulting on the generation I samples. Power spectrum analysis distinguished the periodicity or the scallops on the Bosch DRIE samples and the scalloped samples exhibited nearly self-similar fractal natures while the cryogenic DRIE and pitting etch samples did not appear to be fractal at any scale.

Chapter 4: Finite Element Analysis

In this chapter the structure-mechanical properties relationships for the test specimens are simulated and analyzed. Finite element modeling software (Abaqus v.6.7-v.6.11, Simulia, Providence, RI) was used to perform simulations of instrumented indentation testing on each of the strength test specimens. Simulations were carried out to cover the range of fabricated sample dimensions and experienced experimental loads; mathematical relationships were developed to translate load-displacement response at the indenter-to-sample interface into the stress-strain response in the test region. Simulations of the gapped-arch theta specimen were carried out by a colleague who implemented the routine I developed below for the Durelli and arch theta specimens; the results of these simulations have been included for comparison.

4.1 Model Configuration

For each specimen design, three-dimensional finite element analysis (FEA) simulations of loading were performed. Each specimen simulation utilized more than 100,000 eight-node linear hexahedral mesh elements; for the theta specimens the critical web segment had 36 to 66 elements in cross-section and approximately 2,000 to 10,000 total elements within the web segment, with more elements used for smaller web widths. Silicon orthotropic elastic properties were used and oriented as in the fabrication sequence, aligning <110> with the theta web axis; the elastic stiffness values were C_{11} = 165.773 GPa, C_{12} = 63.924 GPa, and C_{44} = 79.619 GPa [McSkimin and Andreatch, 1964]. This material orientation was identical for the C-ring specimen. The boundary

conditions for all specimens are illustrated in Figure 4.1. The very bottom horizontal surface (highlighted in red) was fixed in the global *x*-, *y*-, and *z*-directions. The red highlighted vertical surfaces were constrained so that they were fixed in the global *x*- and *z*-directions but free in the global *y*-direction. The top horizontal surface of the sphere had a pressure applied in the *y*-direction and was constrained so that it was fixed in the global *x*- and *z*-directions but free in the global *y*-direction (indicated by the orange markings). The silicon anisotropic elastic property orientation along <110> is specified by the two yellow diagonal dashed lines as a local coordinate system. The relative size comparison between the spherical indenter tip and the test sample is also apparent.

4.2 Durelli and Arch Theta Specimens

Simulated loads of 20 mN to 200 mN in increments of 20 mN, along with a load of 2 N, were applied to the top center of the Durelli and arch theta specimens using a hemisphere with a 250-µm radius indenter and isotropic elastic property values approximating sapphire with a Young's modulus of 400 GPa and a Poisson's ratio of 0.24 [Holm *et al.*, 1999]. Simulations were performed under ideal loading conditions; previously, simulations were performed of non-ideal loading on a generation I theta specimen [Fuller *et al.*, 2007] that resulted in the inclusion of the top hat structure in generation II specimens and the adoption of a spherical indenter tip for testing.

FEA images of the maximum principle stress for both theta specimens with ideal dimensions are shown in Figure 4.2. Both specimens have the same applied load. The maximum principal stress is clearly greatest in the constant cross-section web segment; this stress is nearly invariant within this region, and is nearly equal for the two designs.

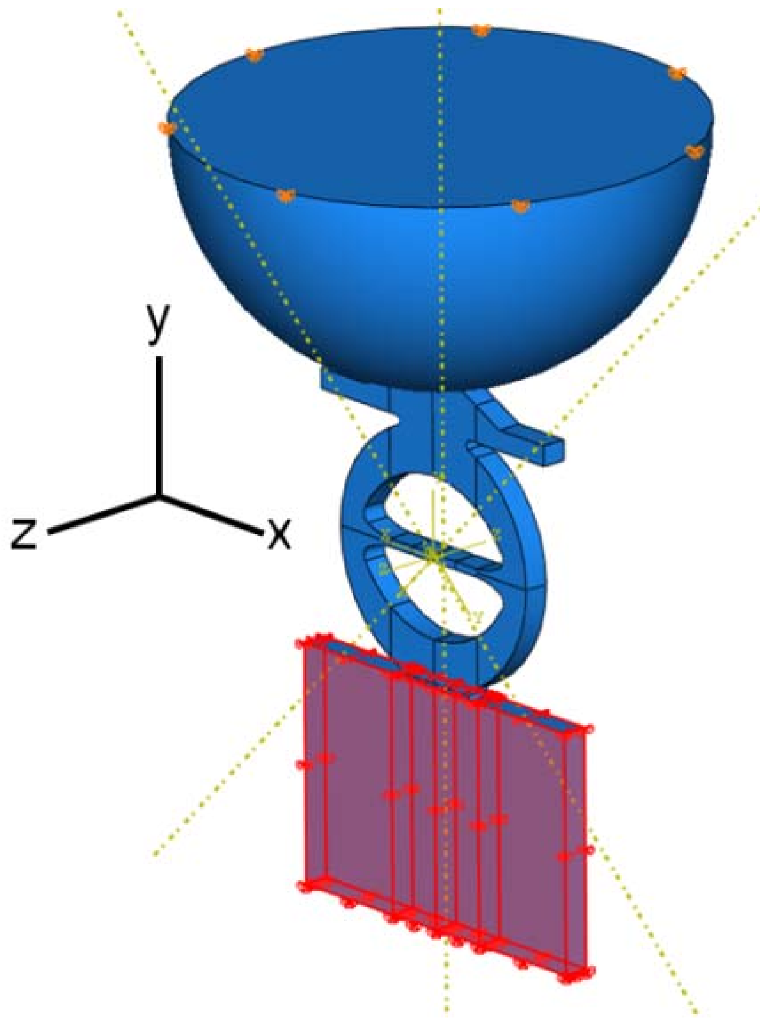

Figure 4.1: The boundary conditions applied to each sample modeled with FEA. The samples have fixed boundary conditions placed on the bottom block beneath the sample to represent the test strip material to which each sample was fixed. The global coordinate system is indicated on the left with the sample thickness in the *z*-direction. The indenter is constrained to load along the *y*-direction indicated by the orange attachments along the circumference of the hemisphere cross-section. Material orientation properties were assigned with a 45° rotation of the global coordinate system in the *x*-*y* plane using the diagonal yellow dash lines to make the length of the web segment along <110>.

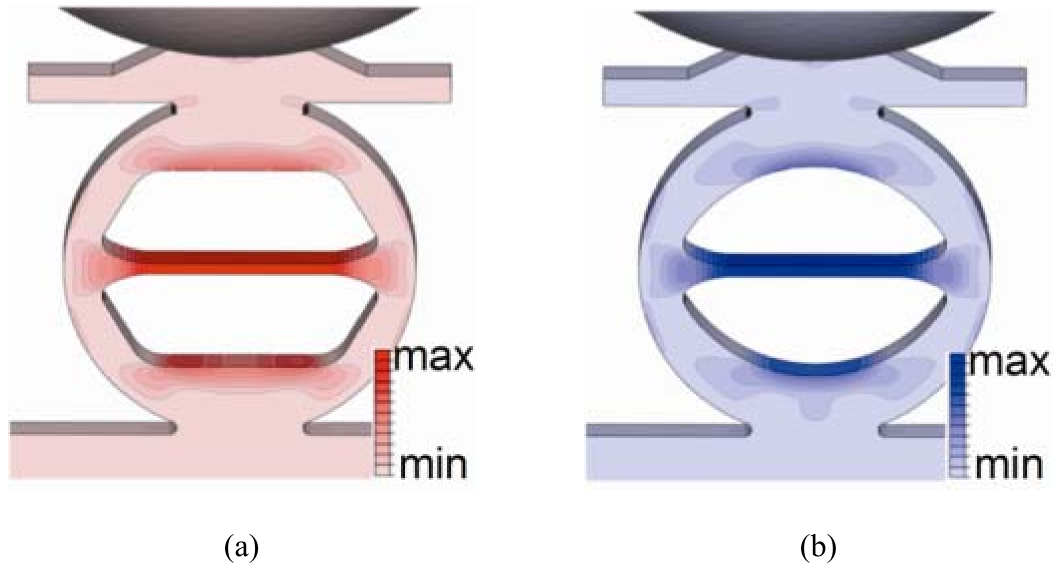

(a) (b)

Figure 4.2: Maximum principal stress distribution for the (a) Durelli and (b) arch theta test specimens subjected to loading with a sapphire sphere. The largest maximum principal stress, σ_{max}, occurs in the web segment, and the largest secondary stress, σ_{sec}, is located at the top and bottom of the inner theta region. For the Durelli theta, the stress ratio $\sigma_{sec}/\sigma_{max}$ = 0.65. For the arch theta, the stress ratio $\sigma_{sec}/\sigma_{max}$ = 0.62. Thus, for both geometries, initial fracture is expected to occur in the web segment.

The stress fields were essentially uniaxial along the web axis for most of the web length, with consequent longitudinal and Poisson-contracted lateral strain fields. Secondary stresses located at the top and bottom of the inside theta regions are significantly less than the primary stress in the web. Both the extent and magnitude of the secondary stress are reduced in the arch theta specimen compared with the Durelli design. In Figure 4.2(a) the maximum secondary stress is 0.65 of the maximum stress in the web, and the secondary stress region in Figure 4.2(b) has a maximum stress of 0.62 of the stress in the web. (The second generation Durelli theta design is an improvement from the first generation round theta design, which had a maximum secondary stress of 0.87 of the maximum stress in the web [Quinn *et al.*, 2005].)

Small regions of stress concentration were observed at the ends of the constant cross-section web regions of the two theta specimens, as shown in Figure 4.3. The stress scale in Figure 4.3 is narrowed to that observed in and around the web region to highlight the stress concentration, which was not discernable in Figure 4.2. The stress scale is normalized to the maximum principal stress in the middle region of the web section. The Durelli theta specimen has a stress concentration of 3 % greater than the main web stress [Figure 4.3(a)] and the arch theta specimen has a stress concentration of 2 % greater than the main web stress [Figure 4.3(b)]. This decreased stress concentration is another positive aspect of the arch theta specimen design. (However, these stress concentration did not appear to cause premature fracture for the tested and observed samples as will be discussed in Ch. 7.)

The simulations were used to translate the applied indentation load, P, and load-point displacement, h, response into stress and strain behavior in the web segment of the

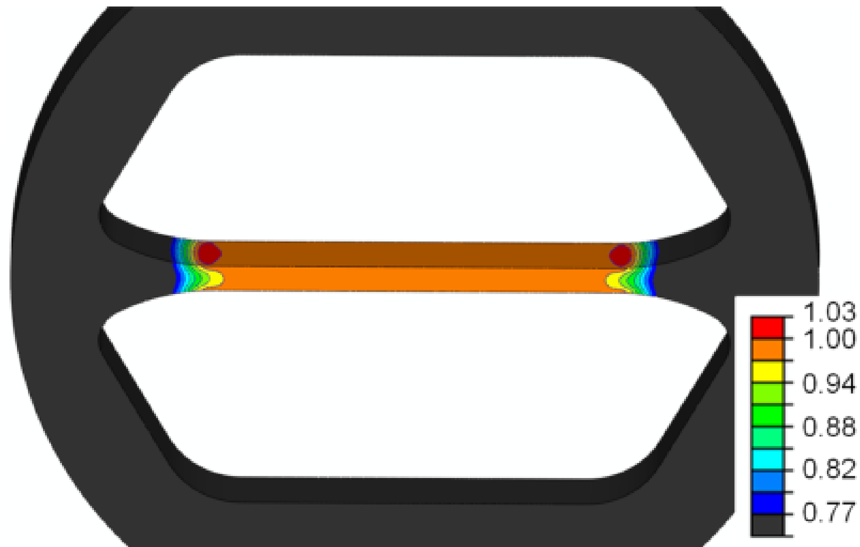

(a)

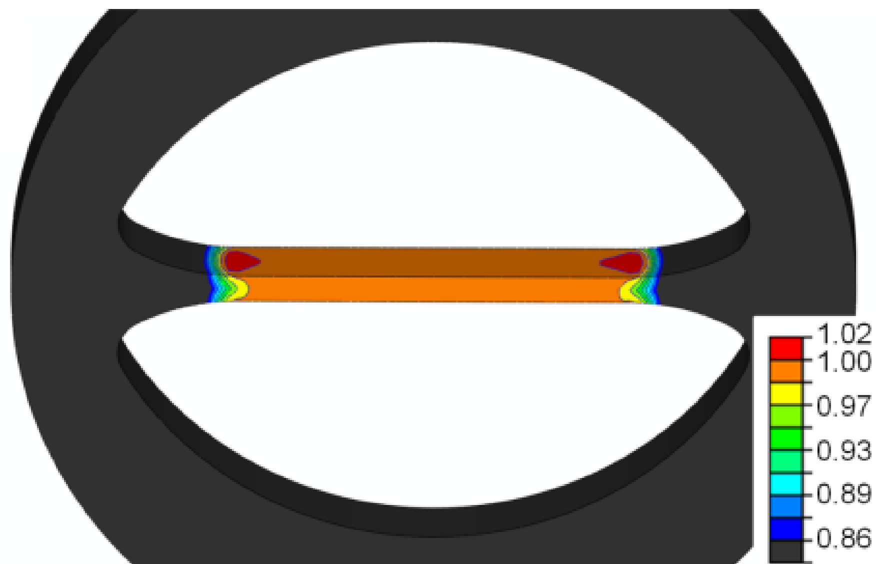

(b)

Figure 4.3: Stress concentration in the ends of the web region of the maximum principal stress for each theta specimen geometry. (a) Durelli stress concentration is about 3 % greater than the stress in the web. (b) Arch stress concentration is about 2 % greater than the stress in the web.

theta specimens of ideal dimensions. In all simulations, P and h were linearly related and specimen compliance, λ, was determined by averaging over all simulated loads. Stress, σ, and strain, ε, in the web segment were determined by averaging the principal stress and strain over the cross-section of the center of the web, respectively. In all simulations, σ and ε were linearly related and linearly related to P and h, respectively. This behavior is highlighted in the arch theta simulation data presented in Figure 4.4, where the stress [Figure 4.4(a)], strain [Figure 4.4(b)], and load-displacement [Figure 4.4(c)] trends were linear up to a simulated load of 2 N. Equations for σ and ε as functions of P and h, theta diameter, D, and specimen thickness, t, were established by averaging responses over all simulated loads. For the Durelli theta specimen these equations were

$$\sigma_{\mathrm{D}} = -14.367\, P/Dt\,, \tag{4.1}$$

$$\varepsilon_{\mathrm{D}} = -0.563\, h/D\,, \tag{4.2}$$

where σ_{D} is in GPa, P is in mN, and D, t, and h are in μm; correlation coefficients for these linear relations were $R^2 > 0.9999$. The related specimen compliance for the Durelli design was $\lambda_{\mathrm{D}} = 6.03$ nm mN^{-1}. The stress and strain equations include negative signs as the load and load-point displacement were taken in the specimen compressive direction while the stress and strain were taken in the web tensile direction. The original Durelli specimen equations had coefficients of 13.8 for stress and 0.585 for strain [Durelli *et al.*, 1962; Durelli and Parks, 1962; Durelli, 1967]. Equations (4.1) and (4.2) contain different coefficients due to the changes in outer specimen design geometry, namely the included top hat and specimen bottom attachment. For the arch theta specimens, the stress and strain in the web segment were determined to be

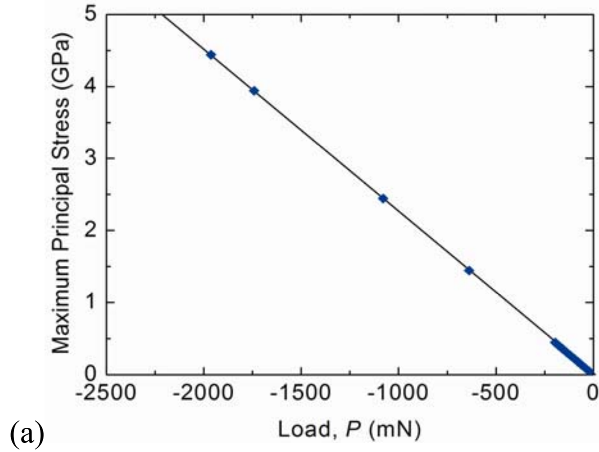

(a)

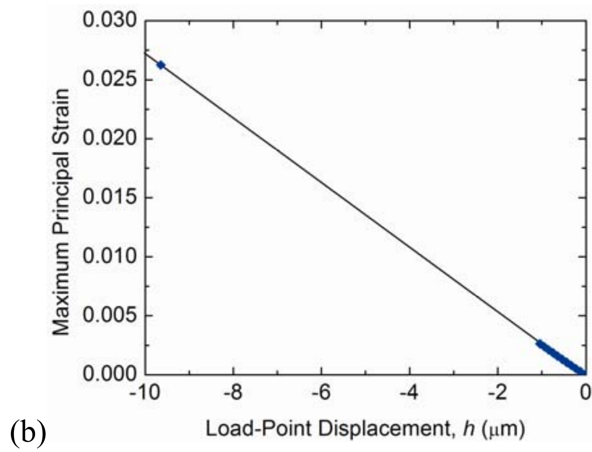

(b)

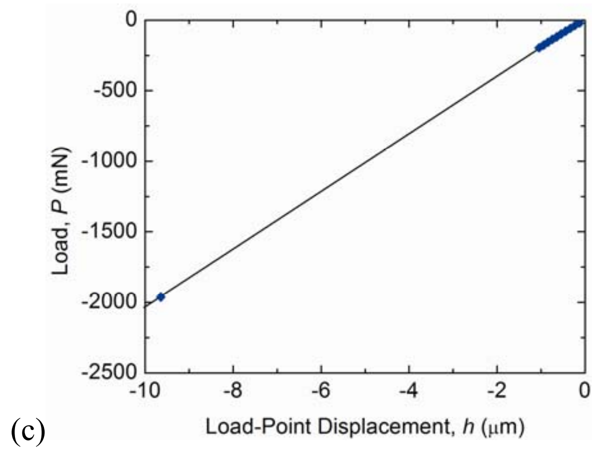

(c)

Figure 4.4: (a) Stress, (b) strain, and (c) load-displacement behavior remained linear at loads up to 2 N. A solid line is drawn through the arch theta data to illustrate the linearity of the data.

$$\sigma_{\mathrm{A}} = -14.239\, P/Dt\,, \tag{4.3}$$

$$\varepsilon_{\mathrm{A}} = -0.639\, h/D\,, \tag{4.4}$$

with arch theta compliance of λ_{A} = 5.27 nm mN^{-1} and units as for Eqs. (4.1) and (4.2). (The change in coefficients in Eqs. (4.3) and (4.4) compared to those cited previously [Gaither *et al.*, 2010] is due to a more detailed analysis of the finite element model.) Equations (4.1) to (4.4), describing the behavior of specimens of ideal geometry, provide the basis for determining the uncertainty arising from the use of the finite element interpolation equations describing the behavior of specimens with non-ideal web widths.

The variation in fabricated sample web widths, illustrated by Fig. 3.8, was incorporated into the FEA simulations in order to accurately determine the mechanical behavior. Stress, strain, and compliance formulas as a function of web width, w, were developed for both theta specimens. The geometry of each specimen was altered by incrementally performing 0.5 μm offsets over the entire specimen plane surface, leaving the thickness unaltered, resulting in 1 μm changes in web width. In particular, offsets were performed to create specimens with 3 μm to 9 μm web widths in 1 μm increments. Simulated loads were applied and the resulting load-point displacements and web stress and strain were determined as described above for each simulated web width and the coefficients relating these four parameters similarly determined. The relationships between the parameters maintained the same form with coefficients, K, which depended on w:

$$\sigma = -K_{\sigma}\, P/Dt\,, \tag{4.5}$$

$$\varepsilon = -K_{\varepsilon}\, h/D\,, \tag{4.6}$$

$$\lambda = K_{\lambda}\lambda_{\mathrm{I}}, \tag{4.7}$$

where λ_{I} is the ideal, $w = 8$ μm, compliance for a given specimen geometry.

The simulation data for each incremental web width, of both theta geometries, over the simulated set of loads (up to 200 mN) are shown in Figure 4.5. Every data set is clearly linear. The maximum principal stress [Figure 4.5(a)], maximum principal strain [Figure 4.5(b)], and load-displacement [Figure 4.5(c)] all have linear trends with different slopes at each increment in web width, and these trends all appear to go through the plot origins. The slope of the linear fits for each data set in Figure 4.5 are used to determine the *K*-factors associated with each web width value for each of the three properties of interest in Eqs. (4.5) to (4.7).

The coefficients *K* were found to be well described by simple inverse dependencies on *w*, and averaging over the seven width simulations for each specimen generated the following expressions

$$K_{\sigma,\mathrm{D}}(w) = 97.224/w + 2.408 \tag{4.8}$$

$$K_{\varepsilon,\mathrm{D}}(w) = 1.660/w + 0.363, \tag{4.9}$$

$$K_{\lambda,\mathrm{D}}(w) = 2.469/w + 0.705, \tag{4.10}$$

for Durelli theta specimens, and

$$K_{\sigma,\mathrm{A}}(w) = 86.001/w + 3.751, \tag{4.11}$$

$$K_{\varepsilon,\mathrm{A}}(w) = 1.670/w + 0.439, \tag{4.12}$$

$$K_{\lambda,\mathrm{A}}(w) = 2.309/w + 0.725, \tag{4.13}$$

for the arch theta specimens. In Eqs. (4.5) to (4.13), K_{σ}, K_{ε}, and K_{λ} are dimensionless and w is in μm. R^2 values for the above dependencies were 0.98 or greater. The fits used to

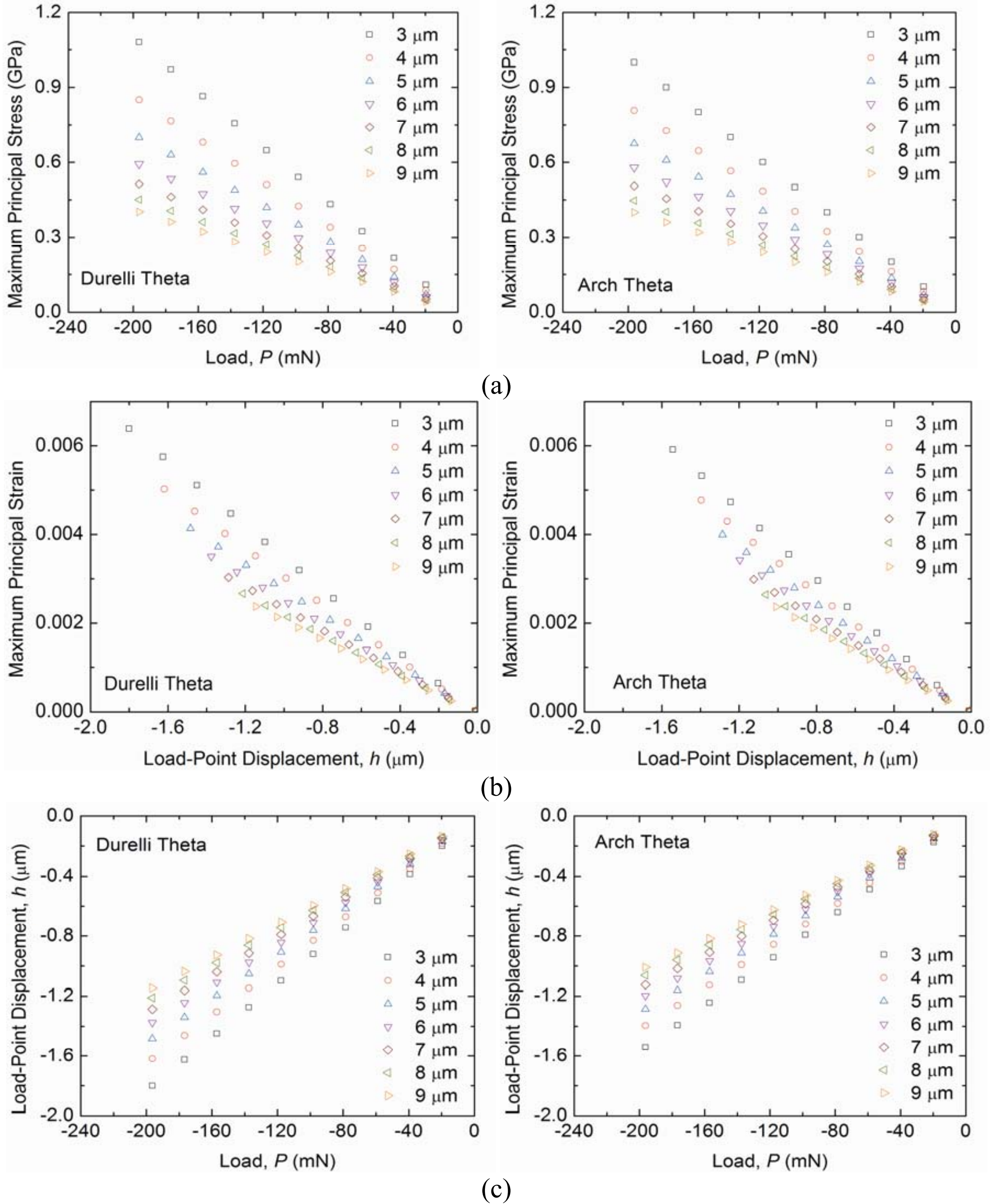

Figure 4.5: (a) Stress (b) strain, and (c) load-displacement behavior for each of the web width simulated for the Durelli (left) and arch (right) theta specimens. Each sample set is linear and slopes from linear fits to these data were used to generate the interpolation equations, Eqs. (4.8) to (4.13).

generate Eqs. (4.5) to (4.13) are shown in Figure 4.6. Inserting $w = 8$ μm into the above interpolation equations reveals about one percent variation from the coefficients for stress and strain given in Eqs. (4.1) to (4.4) and about two percent variation from the ideal compliance values. Eqs. (4.8) to (4.13) are determined from these linear fits. Equations (4.8) to (4.13) are used to analyze the elastic behavior and determine the fracture strength of each batch of Durelli and arch theta samples described in Ch. 2. The validation of the finite element simulations, the translation of the experimental load-displacement behavior, and the resulting sample strength of each batch of theta samples will be presented in Ch. 5 and 6.

4.3 C-ring Specimen

C-ring simulations were performed with an applied pressure over a small area on the center line of the C-ring tophat. This change from the way the Durelli and arch theta simulations were performed was due to the difficulty in simulating contact in the finite element simulations; that this was an approximately equal loading, based on St. Venant's principle and the relatively large tophat structure, to what was simulated in the previous theta section. 12 load steps were simulated at increasing intervals up to 20 mN. The effects of loading misalignment were also examined by performing simulations with 20 μm offsets to the right and left of the center-point on the tophat along the specimen center line. The offset simulations were performed with the same load steps.

Figure 4.7 shows the maximum principal stress for the ideal loading [Figure 4.7(a)] and offset loading [Figure 4.7(b) and (c)] cases. Each simulation is shown at the same load step and the figure includes both an edge-on and tilted view for each case to

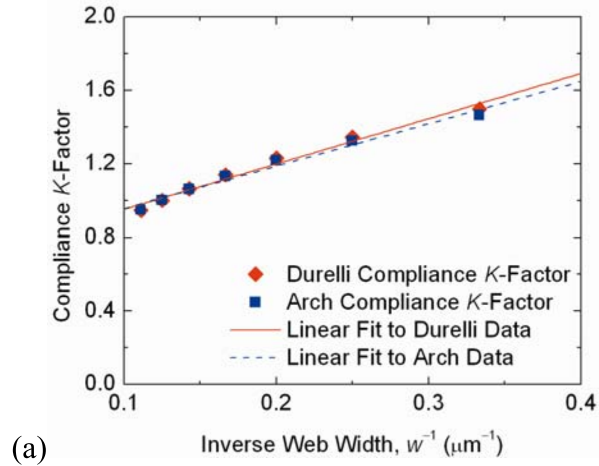

(a)

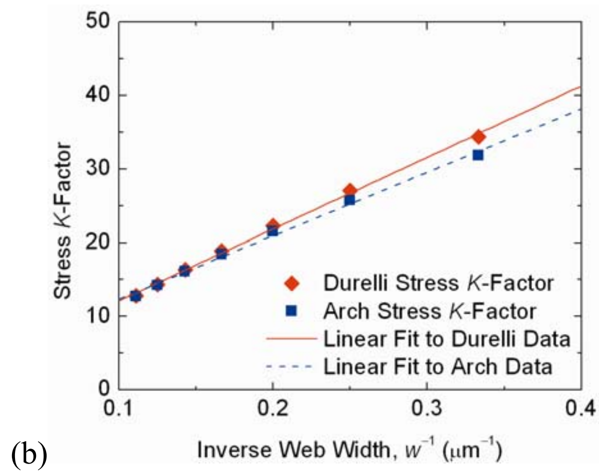

(b)

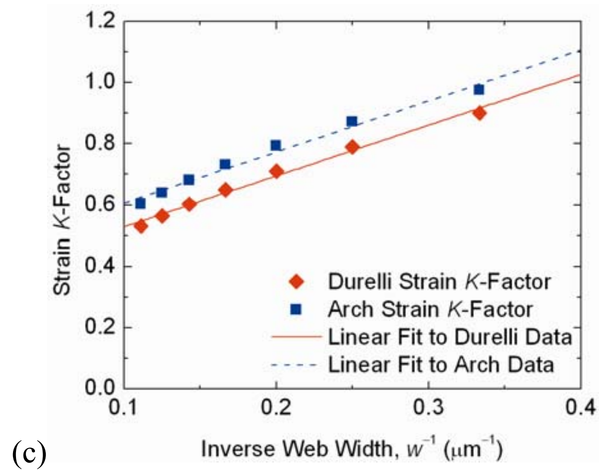

(c)

Figure 4.6: (a) Compliance, (b) stress, and (c) strain *K*-factor plots as functions of inverse web width and corresponding linear fit lines.

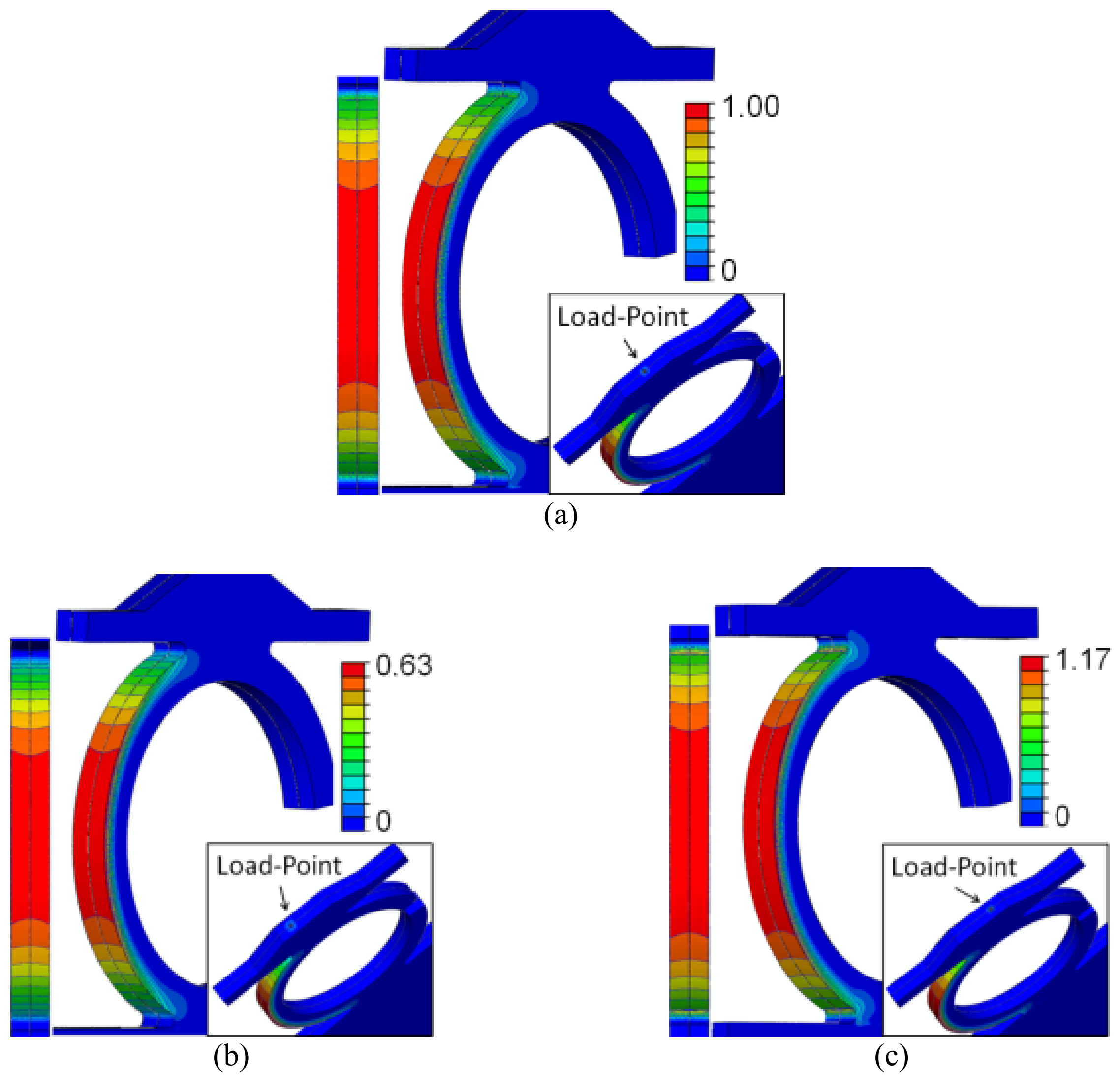

Figure 4.7: Maximum principal stress for the C-ring specimen under ideal and off-center loading. In (a) the ideal load condition is applied at the center point of the tophat as indicated in the inset. The off-center loading conditions used a load-point applied 20 μm to the (b) left and (c) right of the center point as indicated in the insets. The stress scales are normalized to the max stress in (a), the ideal loading case.

observe the stress state in the C-ring. The insets of the figures indicate the loading condition. The maximum principal stress is clearly in the central region of the left side of the C-ring. The effects of offsetting the load location does not change the location of the maximum stress, however the stress magnitude is affected. Each stress scale is normalized to the ideal C-ring loading maximum stress value; the maximum stress increases as the load location is moved from left to right.

The equation for the maximum stress, σ, as a function of applied load, P, follows the strength of materials formula presented in the C-ring ASTM standard [C1323–96, 2001]. Combining all the sample dimension factors into a single coefficient for simplification and calculating that coefficient based on dimensions of this C-ring design, the equation for stress becomes

$$\sigma_{\mathrm{c}} = C_{\mathrm{I}} P \, , \tag{4.14}$$

where C_{I} is the sample geometry coefficient for an ideal C-ring geometry based on the ASTM standard [C1323–96, 2001]. Based on the dimensions of the C-ring specimen, $C_{\mathrm{I}} = 0.0448\ \mathrm{nm}^{-2}$; however, the C-ring specimen here does not have the ideal specimen geometry due to the bottom attachment and the tophat structure. It is therefore necessary to include a "geometric adjustment factor", K_{R}, in the stress equation to account for the effects of the additional features on the specimen. The C-ring stress is then defined as

$$\sigma_{\mathrm{c}} = K_R C_{\mathrm{I}} P \, . \tag{4.15}$$

For the center-point loaded C-ring simulation, $K_{\mathrm{R}} = 1.613$; the stress was determined as the average stress across the center line of the maximum stress region. The correlation coefficient for this linear relation was $R^2 > 0.999$. The specimen compliance for the C-

ring design was λ_C = 937 nm mN^{-1}, more than two orders of magnitude greater than the compliance of the Durelli and arch theta specimens.

The simulation of the C-ring specimen at 20 mN is shown in Figure 4.8. As is clear in the figure, the 40 μm C-ring opening is almost completely closed at this applied load. This load corresponds to a C-ring stress of 1.45 GPa. Once the two ends of the opening come into contact the test is no longer the intended C-ring bend test. As will be discussed in subsequent chapters, this load and stress limitation can have adverse effects on the sample testing results.

4.4 Gapped-Arch Theta Specimen

The gapped-arch theta was simulated in the same manner as the C-ring specimen. Simulations were performed at load increments of 20 mN up to 200 mN and subsequently loaded with six larger increments to reach a max simulated load of 2 N. The gapped-arch theta was simulated without a tensile test sample across the gapped region. This allowed for the determination of the specimen compliance and the sample stress and strain relations to load and load-point displacement, respectively, to utilize the gapped-arch theta as an alternative bend test specimen. The gapped-arch theta simulated this way produces four maximum principal stress regions, two regions at the inner top and two at the inner bottom as is pointed out in Figure 4.9. These maximum principal stress regions are the secondary stress regions of the arch theta and are much smaller regions of stress than both the theta specimens and the C-ring specimen. Following the same equation forms as Eqs. (4.1) to (4.4) for the Durelli and arch thetas, the stress and strain at these maximum stress regions are

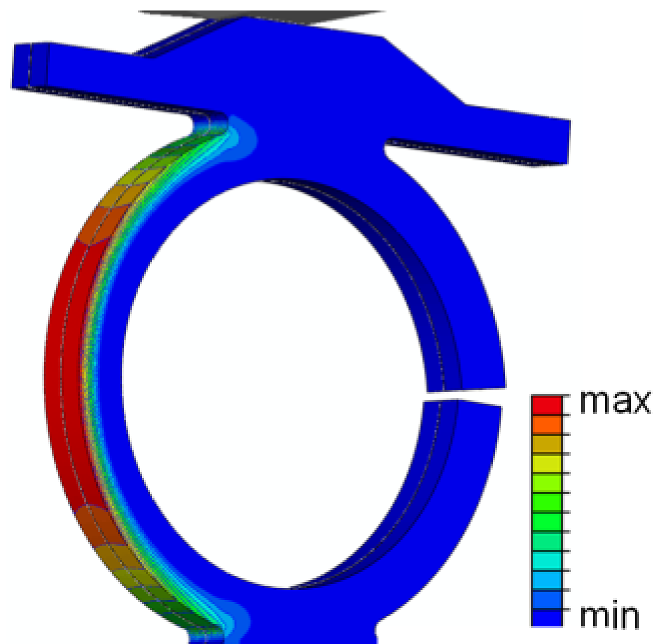

Figure 4.8: The C-ring simulation at the step just prior to contact between the faces of the 40 μm C-ring opening at a simulated load of 20 mN.

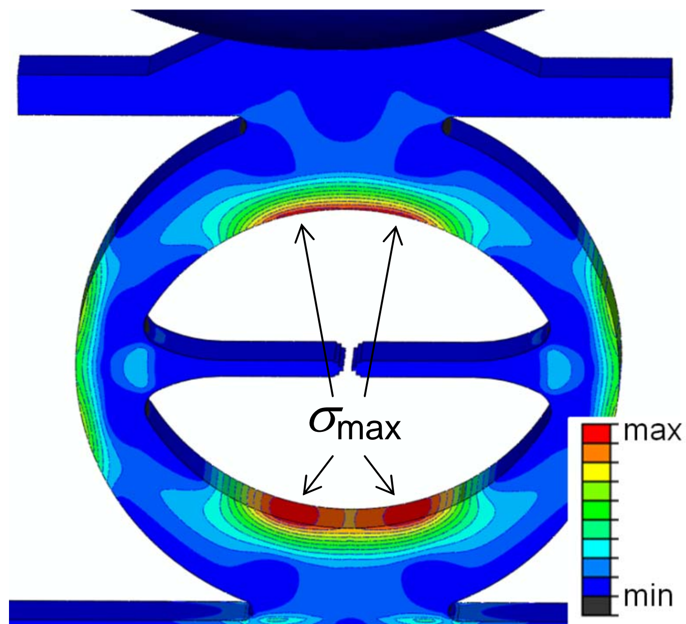

Figure 4.9: The gapped-arch theta specimen. The maximum stress is seen in the region designated as the secondary stress region for the Durelli and arch theta.

$$\sigma_{\mathrm{G}} = -20.3\frac{P}{Dt}, \tag{4.16}$$#

$$\varepsilon_{\mathrm{G}} = -0.544\frac{h}{D}. \tag{4.17}$$#

There was a slight difference in the top and bottom stress and strain with the top being 0.3 % and 1.3 % less, respectively. The coefficients in Eqs. (4.16) and (4.17) are averages of the bottom and top coefficients. The predicted compliance of the gapped-arch theta specimen is λ_{G} = 9.59 nm mN^{-1}; the gapped-arch specimen compliance is more than 50 % greater than the compliance of both the Durelli and Arch specimens, which might be expected due to the geometry of the theta specimen changing to an essentially ring-like structure.

4.5 *Summary*

The structure-properties relationships for the elastic behavior of each sample geometry and sample dimension variation has been developed via FEA. Simulations were performed with single-crystal silicon material properties with the same orientation as the fabricated samples. The largest maximum principle stress is in the web region of the Durelli and arch thetas, the outer-left surface of the C-ring specimen, and the top and bottom regions of the internal arches of the gapped-arch theta specimen. Load-displacement behavior for each of the specimen geometries is predicted to be linear elastic. The closure of the C-ring opening is predicted to occur at approximately 20 mN.

Chapter 5: Elastic Behavior

In this chapter the structure-properties relationship is examined across sample geometries and dimensional variations though the analysis of elastic deformation behavior. The elastic deformation is examined against the FEA simulations in Ch. 4. Sample compliance measurements from load-displacement responses are compared to predicted behavior across sample web width variations to validate the FEA simulations. Cyclic loading is examined to confirm proper mounting configuration and Young's modulus measurements are made with converted load-displacement data.

5.1 Theta Elastic Deformation

Figure 5.1 shows load-displacement responses for five of each of the fabricated Durelli and arch samples taken from the initial cyclic loading between a peak load of 200 mN and 100 mN. Responses for sample widths from just less than the target width of 8 μm to slightly greater than 4 μm are shown, and only the first unloading response for each sample is shown. The compliance of the samples for both geometries increases with decreasing web width, as highlighted by the best fit straight lines passing through the extremes of the web widths. Best fits to all the responses generated compliance values that were all slightly greater than the compliance values predicted from the FEA, Eqs. (4.7), (4.10), and (4.13). There was no trend of the increase in compliance with sample web width, suggesting that the additional inferred deformation and resulting compliance was associated with indenter contact and test strip mounting. The mean and standard deviation of the additional test system compliance, determined from the 10 samples in

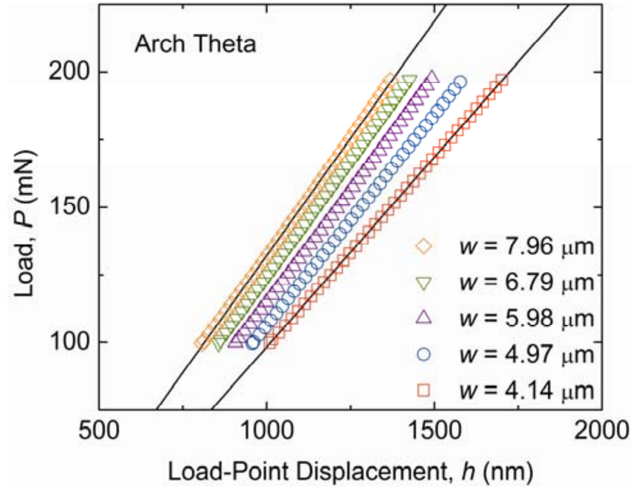

(a)

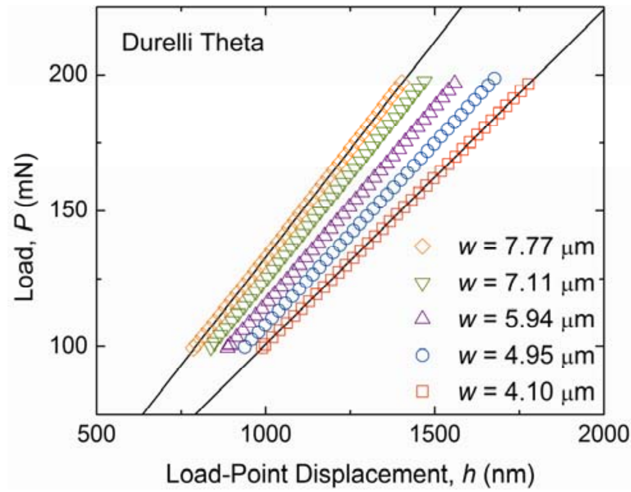

(b)

Figure 5.1: *P*-*h* data for the first unloading segment of 5 different cyclically loaded (a) Durelli and (b) arch theta test samples with a 4 μm to 8 μm distribution of web widths. As w decreases, the compliance, λ, of the theta test specimen increases, illustrated by the changing slope of the data sets. Best fits to all the responses generated compliance values that were all slightly greater than the compliance values predicted from the FEA due to test system deformation compliance.

Figure 5.1 was (0.21 ± 0.10) nm mN^{-1}, approximately 3 % of the average experimental compliance value for the 10 samples. Deformation associated with this test-system compliance was subsequently subtracted from all presented theta displacement data. The agreement between the measured and predicted compliance values, notwithstanding the additional test system compliance, indicates that the FEA of the specimens was accurate and that the dependencies of Eqs. (4.8) to (4.13) are accurate for relating web stress and strain to indenter load and displacement.

Figure 5.2 shows the complete cyclic load-displacement responses for single example Durelli and arch samples. Equations (4.8), (4.9), (4.11), and (4.12) were used to generate web stress and strain data from the sample load-displacement data. An initial, recoverable, non-linear response is visible for the example arch sample, Figure 5.2(b); this was typical of the initial first-cycle response for all samples examined and is probably associated with seating and unseating of the spherical indenter on the rough etched surface of the hat. This initial non-linear response was quite variable, and in some cases extended over several micrometers of displacement. In other cases, this first-cycle non-linearity was barely discernible, as shown in the example Durelli sample, Figure 5.2(a). After the initial loading, the data for all the loading cycles between 100 mN and 200 mN for both geometries are indistinguishable, indicating negligible subsequent hysteresis; this lack of cyclic hysteresis was common to all samples tested, indicating a completely elastic response after initial indenter seating and that the sample mounting configuration was effective and essentially lossless. Best-fit straight lines to the cyclic loading data are shown in Figure 5.2, giving rise to elastic moduli values of (171 ± 3) GPa and (167 ± 3) GPa, for the example Durelli and arch samples, respectively, where

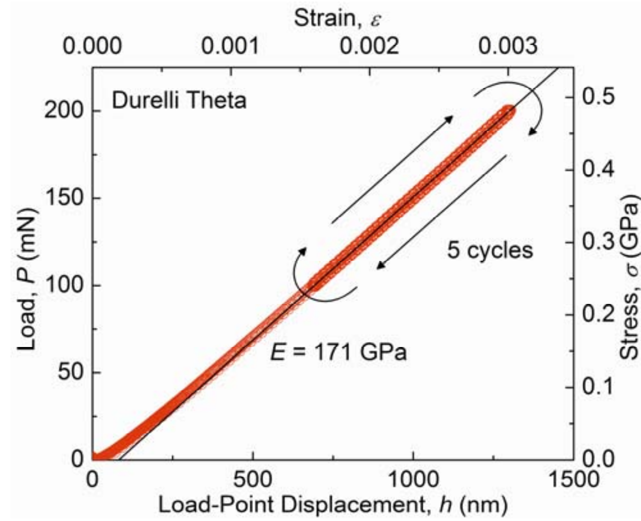

(a)

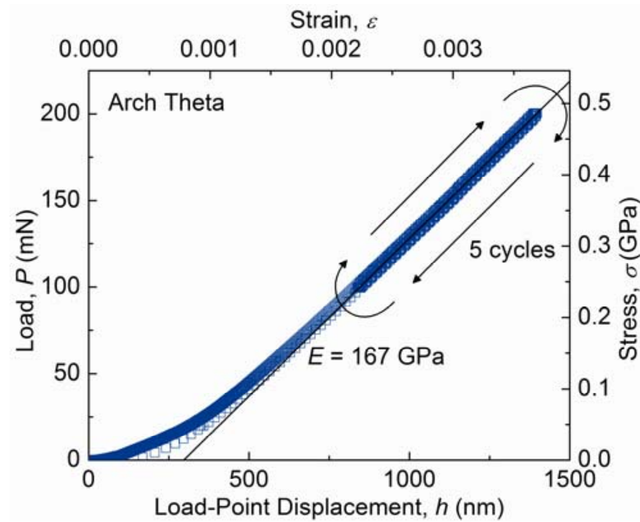

(b)

Figure 5.2: P–h and corresponding σ–ε data for (a) Durelli and (b) arch theta test samples subjected to five load-unload cycles with a maximum load of roughly one-fifth the typical fracture load. The traces are linear with no discernable hysteresis, which suggests a secure and stable test platform. E was determined from the slope of the linear portion of the trace. For these particular samples, E = 171 GPa for the Durelli theta and E = 167 GPa for the arch theta.

the uncertainty includes the measurement uncertainty and the finite element interpolation equations uncertainty. These values compare with 168.9 GPa for the Young's modulus of Si in the <110> directions [Brantley, 1973]. The elastic responses and moduli agreement serve to validate the combined experimental and analytical approaches.

5.2 *C-Ring Elastic Deformation*

C-rings from the second batch of second generation samples were mounted and load was applied in the same manner as the Durelli and arch theta specimens. From Ch. 4, the C-ring elastic response was predicted to be linear with a relatively large compliance (λ_C = 937 nm mN^{-1}). The C-ring specimen simulations also predicted the closure of the 40 μm C-ring opening at approximately 20 mN. The tested C-ring load-displacement responses did not generally follow this behavior.

Figure 5.3 shows two example C-ring load-displacement responses that illustrate the range of responses observed. In Figure 5.3(a) the load-displacement response has two different compliance regions, an initial region with a compliance of λ = 909 nm mN^{-1} that gradually transitions to a longer and stiffer compliance region with a compliance of λ = 100 nm mN^{-1}. The initial region has a compliance value similar to the predicted compliance; however this region only extends over a very small region. This transition does not appear to be due to the closure of the C-ring opening because the transition occurs at approximately one-tenth the predicted load. After the transition at approximately P = 2 mN the remainder of the trace is linear up to a load of P = 30 mN. At or near P = 20 mN there is no indication in the load-displacement data that there is a contacting event occurring. Furthermore, the load-point displacement at this load is far

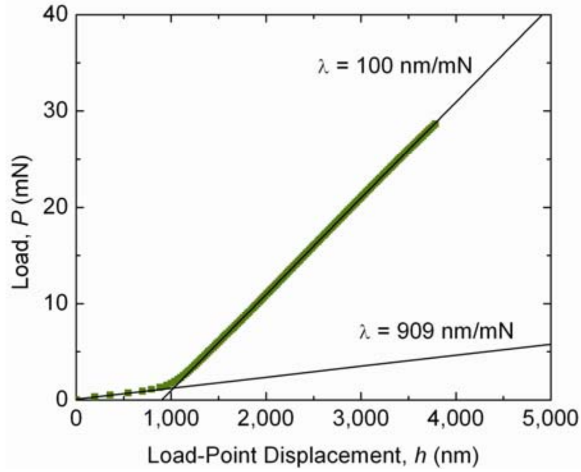

(a)

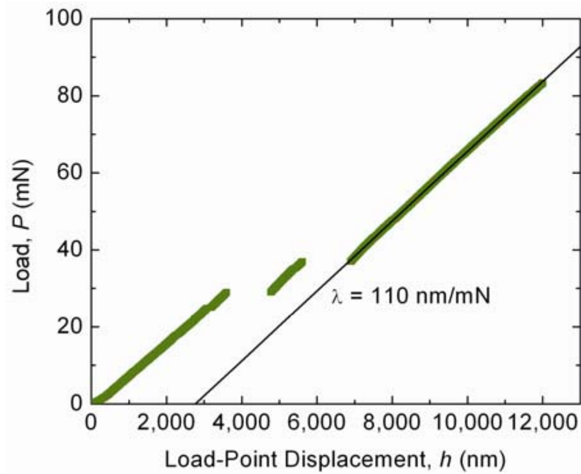

(b)

Figure 5.3: Examples of C-ring load-displacement behavior. (a) In this example there is an initial section with a very compliant linear response nearly that of the FEA predicted compliance that transitions gradually to a less compliant linear response. The compliances in the first and second region are λ = 909 nm mN^{-1} and λ = 100 nm mN^{-1}, respectively. (b) In this example there are jumps larger than 1 μm between segments of linear response that maintain nearly the same compliance, λ = 110 nm mN^{-1}, similar to that in the second region of (a).

too small for the contacting to have occurred. In Figure 5.3(b) the load-displacement response has three regions with similar compliances that have jumps larger than 1 μm between segments. The compliance of the third segment is λ = 110 nm mN^{-1}, similar to, but 10 % greater than, the second region of Figure 5.3(a). As was observed in Figure 5.3(a), no event occurs at or near P = 20 mN; the first jump in the data was at approximately P = 30 mN.

Figure 5.4 shows the complete cyclic load-displacement responses for two example C-ring samples. The examples in Figure 5.4(a) and (b) have initial load segments with similar behavior to those in Figure 5.3(a) and (b), respectively. The cyclic data shows a slight hysteresis with an overall shift in displacement. The lowest load region of the cyclic data in Figure 5.4(b) is slightly non-linear and is likely due to a low-load indenter-to-sample contact interaction. Because the cyclic data in Figure 5.2 did not exhibit a hysteresis, and the same mounting and loading procedure was used in the testing both the theta (Figure 5.2) and C-ring (Figure 5.4) samples, the cause of this hysteresis is likely related to interaction between the sample top and indenter tip. This hysteresis and shift in overall displacement was observed to a greater or lesser extent in most C-ring samples tested; in a very few cases there was a negligible hysteresis (as in Figure 5.2) in the cyclic load-displacement data.

The load-displacement behavior of the tested C-rings had several characteristics in common: In most cases the load-displacement data had jumps in displacement along the linear region of the data; the initial loading region had a significantly greater compliance behavior, sometimes observed along with the non-linear behavior associated with the indenter-to-sample seating discussed in the previous section; cyclic loading

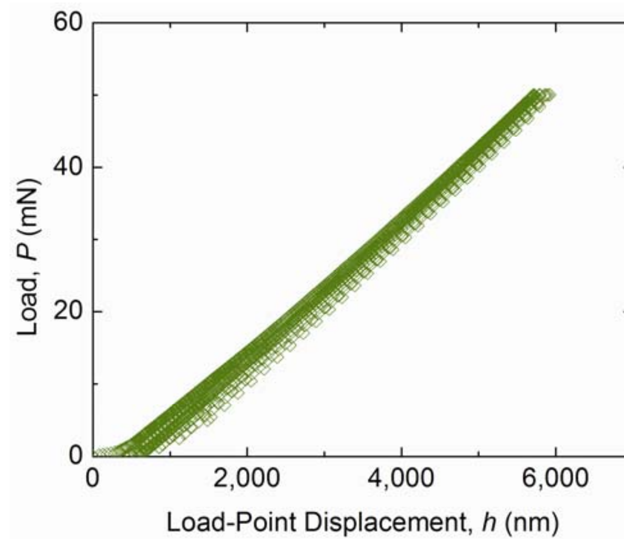

(a)

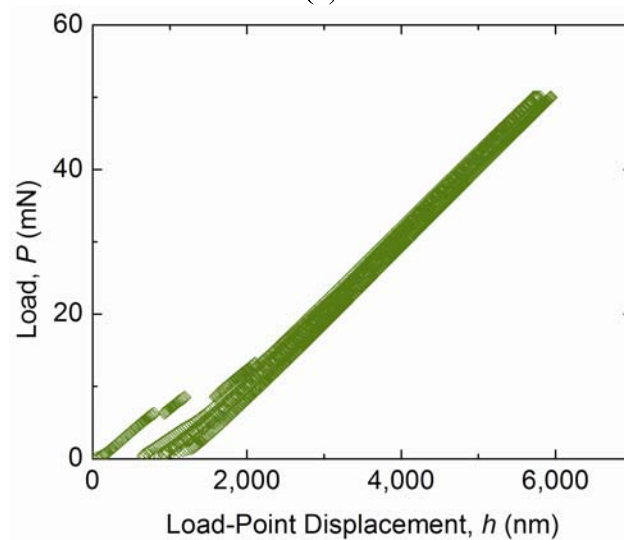

(b)

Figure 5.4: Examples of 5-cycle load-displacement behavior for the C-ring specimen. After the initial non-linear region in the first load step, the load-displacement data over the five load-unload cycles exhibits a slight hysteresis that results in a progressive shift in displacement. The initial load segments in (a) and (b) corresponds to the load-displacement behavior highlighted in Figure 5.3(a) and (b), respectively.

exhibited some hysteresis and a progressive increase in overall displacement; only in the initial loading region of the load-displacement data for only some of the tested C-ring samples was there agreement between the FEA predicted compliance and the measured compliance, and this compliance agreement changed prior to the expected load required to induce closure of the C-ring opening.

The displacement jumps in the initial loading and the increase in overall displacement during the cyclic loading may be a result of the asymmetry of the C-ring design, which allowed a tilting of the C-ring top surface during testing. The cyclic segment of the IIT routine was operated in load-control causing the indenter to constantly increase the load regardless of the displacement behavior. Due to the fixed base and design asymmetry of the C-ring the top of the C-ring will have a rightward elastic response as load is applied, as was seen in the C-ring FEA simulations (Ch. 4). This may cause a possible frictional sliding between the indenter tip and sample top surface resulting in large displacement changes at the indenter-to-sample interface; however this does not altogether explain the *increase* in displacement, as it is unclear whether the rightward movement of the sample top surface would have presented a "higher" or "lower" surface to the indenter tip. Further investigation may determine the cause of this behavior.

The initial region of greater compliance is the only region where there is agreement with the FEA simulations. It is not observable for every sample due to the non-linear behavior associated with the indenter-to-sample seating. It is unlikely that the FEA simulations are invalid because the simulations were performed in the same way as the simulations for the Durelli and arch specimens and there is good agreement between

these latter simulations and experimental data. There may be an unforeseen interaction occurring during testing that is producing a smaller compliance behavior in the data, such as contact with the strip or backer plate sidewalls very early in the test. It may also be the case that the IIT routine is not sensitive enough to determine initial contact with the surface and "finds" the sample surface, and "zeros" the load-point displacement, after it has already caused a significant displacement in the sample top surface. This would allow for earlier events in the load-displacement data that would indicate closure of the C-ring opening. Further investigation is needed to determine the cause of the disagreement between predicted behavior and experimental data.

5.3 Gapped-Arch Theta Elastic Deformation

Figure 5.5 shows the load-displacement response for a gapped-arch theta sample loaded to 250 mN and cycled five times down to nearly 0 mN. The five-cycle region in Figure 5.5 is linear and does not exhibit hysteresis. (There is a small slightly non-linear response at the lowest load region of the cyclic data that is likely due to a low-load indenter-to-sample contact interaction.) The load-displacement responses for the gapped-arch theta resemble the Durelli and arch theta samples in Figure 5.2; after an initial non-linear seating and loading segment, the cyclic region has no discernable hysteresis. The compliance of the sample in Figure 5.5, calculated from the entire cyclic loading test segment, was $\lambda = 9.23$ nm mN^{-1}, which is about 4 % less than the predicted compliance of $\lambda_G = 9.59$ nm mN^{-1}. For the 24 samples tested the overall compliance behavior was $\lambda = (9.74 \pm 0.40)$ nm mN^{-1}, in good agreement with the predicted sample compliance.

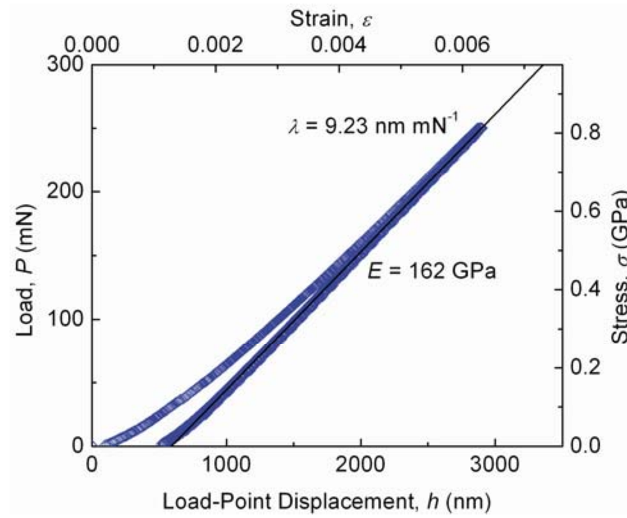

Figure 5.5: *P*-*h* and corresponding σ–ε data of a gapped-arch theta sample for the cyclic loading segment of the test. After an initial non-linear loading segment the five cycle data is linear with negligible hysteresis and a compliance of λ = 9.23 nm mN^{-1} and corresponding elastic modulus of E = 162 GPa.

From the linear region of the translated σ–ε data in Figure 5.5, the elastic modulus is determined to be E = 162 GPa. This is the modulus measured at the four essentially equal secondary stress regions in the top and bottom arches of the gapped-arch theta. These regions are not oriented along <110>, but are on curved regions that have, at the largest secondary stress location, a slight deviation from <110>. As mentioned in an earlier section, the Young's modulus of Si in the <110> direction is 168.9 GPa; for Si in the <100> direction, the modulus is 130.2 GPa [Brantley, 1973]. Given that the orientations of these segments are not <110>, but are oriented between <110> and <100> and more closely oriented to <110>, this decrease in measured elastic modulus from the known value in the <110> direction is a reasonable result.

5.4 Summary

The agreement between the theta sample elastic response and the finite element simulations developed in Ch. 4 across the sample dimensional variations validates the simulation interpolation relationships. The sample mounting and testing configuration was shown to provide the effective control needed to perform the tests validly. The structure-properties relationship for the theta samples elastic behavior was developed with good agreement between measured and reported silicon elastic modulus values. Similar behavior and simulation agreement was observed for the gapped-arch theta.

The C-ring elastic response was problematic. Agreement between the sample compliance and simulate behavior was not observed. C-ring load-displacement behavior was not consistent with jumps in displacement and abrupt slope changes being observed. Attribution of the slope change might be due to the closure of the C-ring opening;

however, the displacement at which this occurred was far too low compared to the simulations in Ch. 4.

Chapter 6: Fracture Strength

In this chapter the structure-property relationship of the fabricated samples is examined through fracture strength measurements and Weibull analysis. The fracture strengths are determined using the FEA relationships developed in Ch. 4 and each set of the four sample geometries are discussed. The Durelli and arch theta samples are examined and compared across each batch of samples. The gapped-arch theta and C-ring sample strengths are also examined for the batch B fabrication runs.

6.1 Strength Measurement and Analysis

Strength values were determined using the stress interpolation equations developed in Ch. 4 for each of the specimen geometries. The strength of a sample was taken as the stress-converted load directly prior to the occurrence of a large increase in displacement during the load-to-failure segment of the load-displacement data. The resulting strength values were fit to a three-parameter Weibull distribution [Weibull, 1951]

$$P_{\mathrm{f}} = 1 - \exp\left(-\left(\frac{\sigma_{\mathrm{f}} - \sigma_{\mathrm{th}}}{\sigma_{\theta}} \right)^{m} \right), \tag{6.1}$$

where P_{f} is the cumulative probability of failure, σ_{th} is the threshold strength, σ_{θ} is a scaling stress (the "characteristic strength" is $\sigma_{\mathrm{th}} + \sigma_{\theta}$), and m is the Weibull modulus. The threshold strength is the stress at which no failure will occur for that particular flaw population; on a strength distribution it fixes the bottom end of the distribution. Broadly speaking, the Weibull modulus is a measure of how 'tight' the distribution is with a narrower distribution having a greater modulus; it is sometimes thought of as the slope of

the distribution. The cumulative failure probability was assigned to each strength value by

$$P_{\mathrm{f}} = (i - 0.5)/N, \tag{6.2}$$

where i is the rank of the strength in an ascending-order ranked strength distribution and N is the total number of strength values in the distribution. Weibull distribution parameter values were determined using a Levenberg-Marquardt fitting algorithm of Eq. (6.1) to the strength data.

It is common practice in the literature to use the two-parameter Weibull distribution [Jadaan *et al.*, 2003] where the threshold strength, σ_{th}, is set at zero, such that

$$P_{\mathrm{f}} = 1 - \exp\left(-\left(\frac{\sigma_{\mathrm{f}}}{\sigma_{\theta}}\right)^{m}\right), \tag{6.3}$$

where σ_{θ} is the characteristic strength. The use of Eq. (6.3) over Eq. (6.1) assumes that there is a non-zero potential for a flaw of any size to induce sample failure in a sample set. The two-parameter Weibull distribution is often used due to the ease of fitting the distribution after mathematical manipulation [C1239–07, 2001]. Some analysis will be performed in this chapter using Eq. (6.3) (e.g., for comparison to previous work); however, Eq. (6.1) is the crucial fitting function for the reliability assessment discussion (see Ch. 8) and will be the primary fitting function utilized here.

6.2 First and Second Generation Durelli Theta

Theta specimens fabricated in the first generation of designs were based on the Durelli theta geometry. First generation samples strength were in the range of 0.23 GPa and 0. 99 GPa based on the mean and three standard deviation values reported for more than 40

tested samples [Quinn *et al.*, 2005]. Strengths of second generation Durelli samples fabricated in batch A ranged from 0.76 GPa to 2.5 GPa. The batch A Durelli strength distribution, along with the range of strengths for the first generation Durelli samples are shown in Figure 6.1. Sample strengths for the second generation have some overlap at the bottom of the distribution with the range reported for the first generation. This is, in general expected, as the second generation samples have about one-quarter the thickness of the first generation and, as was observed in Fig 1.2, samples with smaller dimensions should tend to have greater strengths for similar processing techniques. However, the processes used to fabricate the two sample sets were not the same especially with the pitting etch result seen in the second generation batch A samples. The increased surface damage caused by the pitting etch process in the batch A wafer, which affected the majority of the Durelli samples decreased the strengths significantly and the overlap in strengths is coincidental.

6.3 Durelli and Arch Theta Strength

Figure 6.2 shows the load-to-failure responses for the example Durelli and arch samples described in Ch. 5 and in Fig. 5.2. Once again Eqs. (4.8), (4.9), (4.11), and (4.12) were used to generate web stress and strain data from the sample load-displacement data; initial non-linear responses are visible for the samples, associated with the re-seating of the indenter between the cyclic (Fig. 5.2) and load-to-failure measurements (Figure 6.2). (Tests of C-rings and gapped-arch thetas, discussed in the following sections, did not have this reseating of the indenter concern because the testing methodology was updated to move directly from the cyclic-loading into the load-to-failure test segments on each

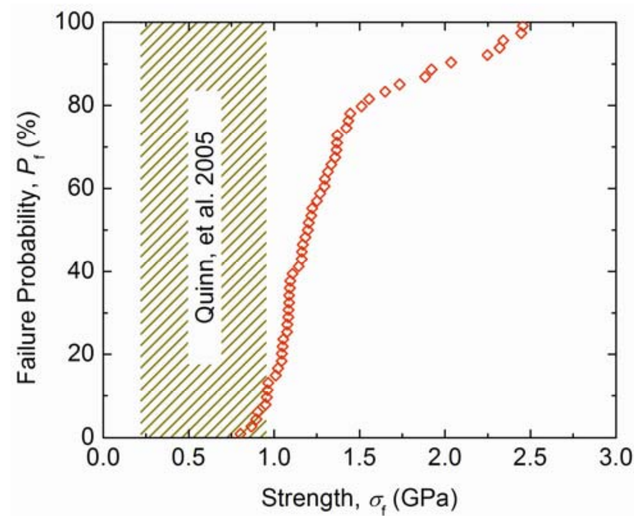

Figure 6.1: Strength comparison of the first batch (batch A) of second generation Durelli thetas to the first generation Durelli thetas. The improvement in test strip design and testing methodology is evident from the increased strengths of specimens. Some strength increase was expected due the decrease in sample size but the adverse effects of the unintended etching process should have affected some samples to have significantly decreased strengths. Even with these considerations, only a small overlap is seen for the strengths of the batch A Durelli thetas compared to the statistical distributions reported for the first generation Durelli thetas [Quinn *et al.*, 2005].

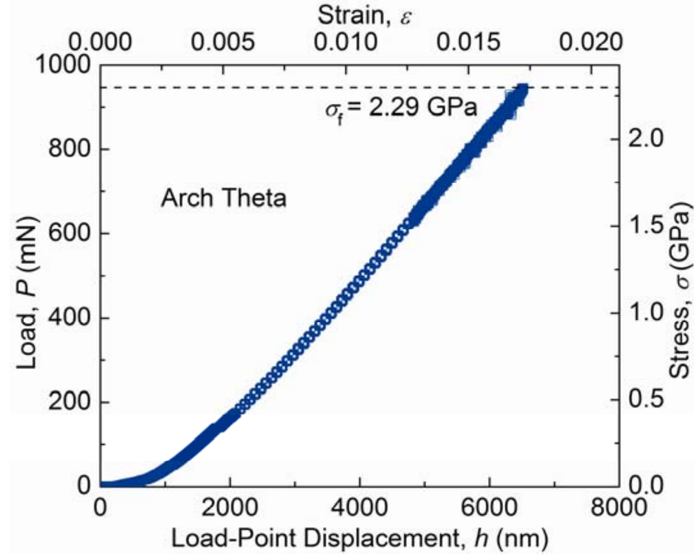

(a)

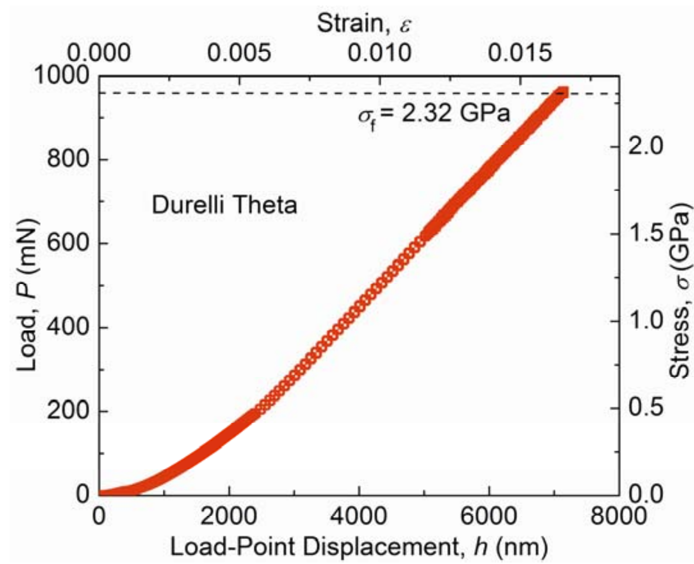

(b)

Figure 6.2: *P*-*h* and σ–ε data for (a) Durelli and (b) arch theta test samples loaded to failure. *E* was determined from the slope of the linear portion of the trace, and σ_f was the stress at which fracture occurred. For these particular samples, *E* was 169 GPa and 166 GPa and σ_f was 2.32 GPa and 2.29 GPa for the Durelli theta and arch theta, respectively.

sample.) The increased scatter in the data prior to peak load and failure is associated with a change in the loading mechanism of the instrumented indenter and decrease in stability at large loads. Linear best-fits to the data for 0.5 % strain prior to failure (not shown) in Figure 6.2, gave rise to elastic moduli values of (169 ± 3) GPa and (166 ± 3) GPa, for the example Durelli and arch samples, respectively, once again in good agreement with the expected value and values determined from the cyclic loading measurements of Fig. 5.2. The strengths for these example samples were 2.32 GPa and 2.29 GPa, respectively, comparable to the values reported in Fig. 1.2 for specimens of similar stressed area. In all samples measured, the stress-strain response was linear prior to failure, at strengths up to 2.7 GPa and corresponding sample failure strains (excluding seating deformation) of approximately 1.8 %.

As noted in Fig. 3.8, both Durelli and arch thetas from the first batch of second generation samples had significant distributions in sample web widths. The resulting strength, σ_f, values for the combined set of Durelli and arch theta samples are plotted as a function of sample web width in Figure 6.3(a). The ideal web width of w = 8 μm is indicated by the vertical solid line and the normal variability in web width observed for DRIE lithography, 0.7 μm, is indicated by vertical dashed lines. Overall, samples with near-ideal web width had greater strengths than samples with reduced web widths, and exhibited less variability in the web width; the mean and standard deviation of the web width of each sample is indicated by the symbol and horizontal uncertainty bar in Figure 6.3(a). (The uncertainty in the strength arising from the finite element interpolation equation and sample thickness uncertainty is smaller than the symbol size.) This variability was apparent when capturing the images for the web width calculation image

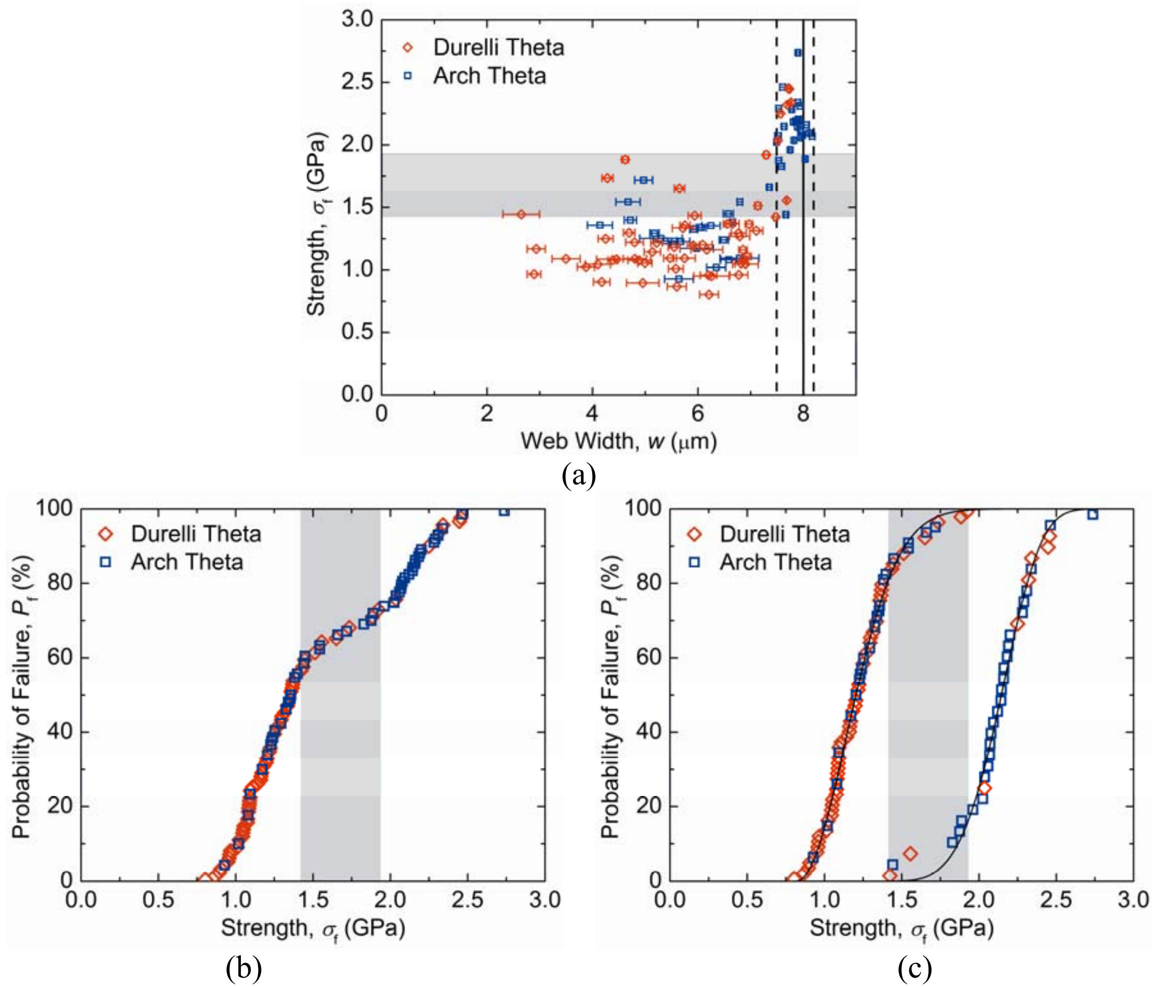

Figure 6.3: (a) Fracture strength as a function of web width. The data can be divided into two groups associated with the sample surface morphology as determined by the etching process as indicated by the dashed line at w = 7.5 μm. For w < 7.5 μm, σ_f varied from 0.8 GPa to 1.9 GPa. For w > 7.5 μm, σ_f varied from 1.4 GPa to 2.7 GPa. The smaller web width samples had greater web width standard deviations indicated by the data error bars. (b) The total strength distribution for the combined Durelli and arch theta test samples is bimodal, as there appear to be three inflection points in the distribution. (c) Weibull failure probability plots for the two distributions in (b) split at w = 7.5 μm. For w > 7.5 μm, $m, \sigma_\theta,$ and σ_{th} were 4.57, 0.90 GPa, and 1.32 GPa, respectively. For w < 7.5 μm, $m, \sigma_\theta,$ and σ_{th} were 2.00, 0.46 GPa, and 0.82 GPa, respectively. In (a) to (c), the grey bands indicate the overlap of the strength distributions.

processing routine (see Ch. 3); samples with smaller web widths had rough sample edges, including the web segment. Figure 6.3(b) is a plot of the cumulative failure probability, P_f, as a function of strength, σ_f, for the combined Durelli and arch theta sample data set. Examination of Figure 6.3(b) suggests that the strength distribution is bimodal, as there appear to be three inflection points in the distribution, with a strength range of approximately (1.4 to 1.9) GPa separating a low strength distribution from a high strength distribution. Comparison with Figure 6.3(a) suggests that this was in fact the case, with the strength, and dominant flaw size, related to the web width. The picture that emerges, considering Figure 6.3, 2.10, and 3.8, is that there are two flaw populations governing the overall strength distribution: The first flaw population is associated with DRIE scallops [Fig 2.10(b)], near-ideal web widths, and small surface roughness, giving rise to small flaws and large strengths. The second flaw population is associated with the pitted surface, [Fig. 2.10(c)], reduced web widths, and large surface roughness, giving rise to large flaws and small strengths. The vertical dashed line in Figure 6.3(a) at a web width of 7.5 μm indicates the boundary separating these width distributions. Flaw population considerations and calculations are covered in Ch. 7.

In Figure 6.3(c), the strength data from each distribution were fit to two different three-parameter Weibull distributions, Eq. (6.1). The strength data were separated into two groups on the basis of the surface morphology of the sample, DRIE scallops or pits, as indicated by the sample web width, near ideal (8.2 μm to 7.5 μm) or reduced (less than 7.5 μm). The strength distributions of the groups overlapped as shown in Figure 6.3(a) and (b) and fits to the two groups were performed separately. The solid lines in Figure

6.3(c) indicate the best-fit distributions, described by m, σ_θ, and σ_{th} values of 4.57 ± 1.18, (0.90 ± 0.26) GPa, and (1.32 ± 0.24) GPa, respectively, for the high strength group, and values of 2.00 ± 0.12, (0.46 ± 0.02) GPa, and (0.82 ± 0.02) GPa for the low strength group. The uncertainties are standard deviations of the fitted values. The R^2 values for these fits were > 0.99, consistent with the agreement between the data and the fitted lines in Figure 6.3(c). The overlap in the strength distributions was in the range (1.4 to 1.9) GPa as indicated by the grey bands in Figure 6.3.

The two subsequent batches of samples did not exhibit the web width variability that was observed in the first batch of samples. Figure 6.4 shows the sample strengths and corresponding web widths for each of the three batches of samples. In Figure 6.4(a), the second (blue) and third (orange) batch of samples had web widths that are grouped into a single distribution for each. These two data sets are shown along with the first (green) batch data [previously shown in Figure 6.3(a)] in Figure 6.4(b). It is clearly seen in Figure 6.4(b) that the second and third batches of samples were a vast improvement in the distribution of resulting sample web widths. The details of the web width range and corresponding web width standard deviations for each batch sample set were given in Ch. 3.

The two- and three-parameter Weibull fits to each of the four strength distributions are organized in Table 6.1. As can be seen from Figure 6.5 and Table 6.1, these strength distributions are well described by the two- and three-parameter Weibull distributions with better fits corresponding to the three-parameter Weibull distribution. Comparison to the single-crystal silicon strength literature also provides good agreement [Schweitz and Ericson, 1999; Namazu *et al.*, 2000; Jadaan *et al.*, 2003] for test samples

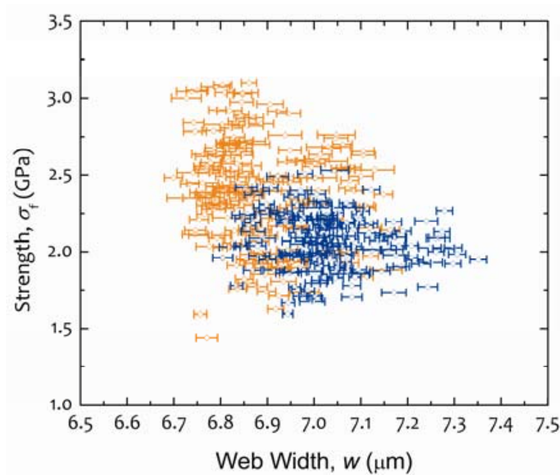

(a)

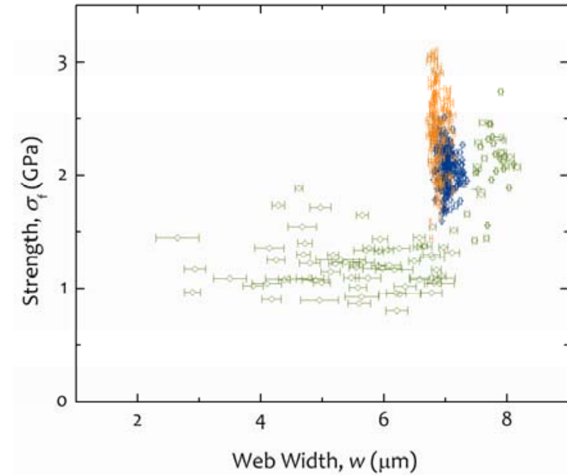

(b)

Figure 6.4: The strength of samples from the (a) second and third batch and (b) all three batches of second generation as a function of the sample web width. In (a), the second (blue) and third (orange) batches both have a single, relatively narrow, grouping of web widths centered at approximately 7.0 μm. The web width standard deviations, indicated by the horizontal bars on each data point, appear larger in the third batch of samples. In (b) the data in (a) is superposed on a graph with the data from the first batch of samples (green). [The data for the first batch was first presented in Figure 6.3(a)]. The fabrication improvements made in the second and third batches are clearly evident by the tighter distribution in web widths, reduced overall web width standard deviations, and sample strengths.

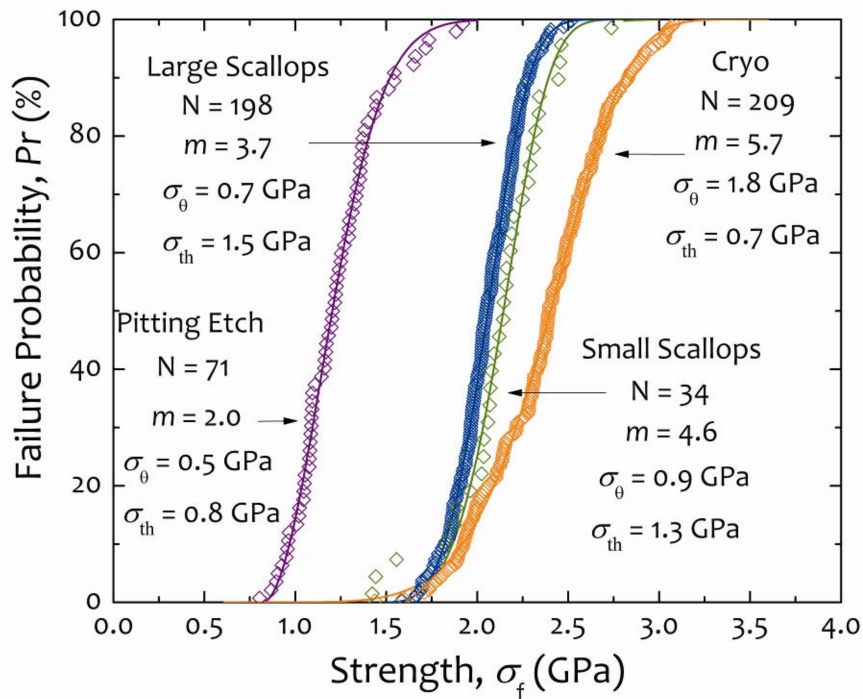

Figure 6.5: The strength distributions and three-parameter Weibull fits resulting from the three batches of theta samples. The pitting etch and small scallops correspond to batch A, the large scallops to batch B, and cryo to batch C.

Table 6.1: The Weibull distribution fit data for each set of theta samples.

		Batch A Pitting Etch	Batch A Small Scallops	Batch B Large Scallops	Batch C Cryogenic DRIE
N		71	34	198	209
Three-Parameter Weibull	m	2.00 ± 0.12	4.57 ± 1.18	3.73 ± 0.12	5.73 ± 0.27
	σ_θ (GPa)	0.46 ± 0.02	0.90 ± 0.26	0.66 ± 0.02	1.84 ± 0.09
	σ_{th} (GPa)	0.82 ± 0.02	1.32 ± 0.24	1.46 ± 0.02	0.67 ± 0.09
	R^2	0.987	0.989	0.998	0.997
Two-Parameter Weibull	m	7.21 ± 0.43	18.12 ± 1.34	12.87 ± 0.11	8.00 ± 0.05
	σ_θ (GPa)	1.406 ± 0.008	2.186 ± 0.006	2.126 ± 0.001	2.519 ± 0.001
	R^2	0.976	0.963	0.995	0.997

with similar stressed areas, with average strengths between 1.7 GPa and 7.7 GPa. Two-parameter Weibull modulus values varied between 3.6 and 7.2 in the same silicon strength literature, all of which are not as great as the two-parameter modulus values in Table 6.1 for all but the pitting etch sample set, suggesting that the etch processing used here produced a narrower size distribution of strength limiting flaws in comparison to the cited research.

6.4 Gapped-Arch Theta Strength

A small number of gapped-arch thetas were tested as bend strength specimens. As these samples were from batch B of the second generation samples the strength of these samples should be governed by the same surface flaws from the tested batch B arch thetas. An example of a batch B gapped-arch theta sample load-displacement break response is shown Figure 6.6. The data is clearly linear and using the simulation stress and strain interpolation equations from Eqs. (4.16) and (4.17), the sample had a strength of 1.77 GPa and a modulus of 162 GPa. The strength is within the range of strengths already determined for batch B theta samples in the previous section. The measured modulus value is less than that of <110> silicon, similar to that presented in section 5.3.

From the batch B fabrication 24 gapped-arch thetas were tested to failure. The gapped-arch theta strength distribution and three-parameter Weibull distribution fit are shown in Figure 6.7. The range of samples strengths are similar to the batch B arch samples in Figure 6.5 with maximum strength values at 2.5 GPa, though the gapped-arch data has strengths less than the arch samples strengths. The three-parameter Weibull modulus, m, for both distribution fits are also in agreement. Since the fabrication of the samples was the same, the threshold strength, σ_{th}, should be comparable; however, one

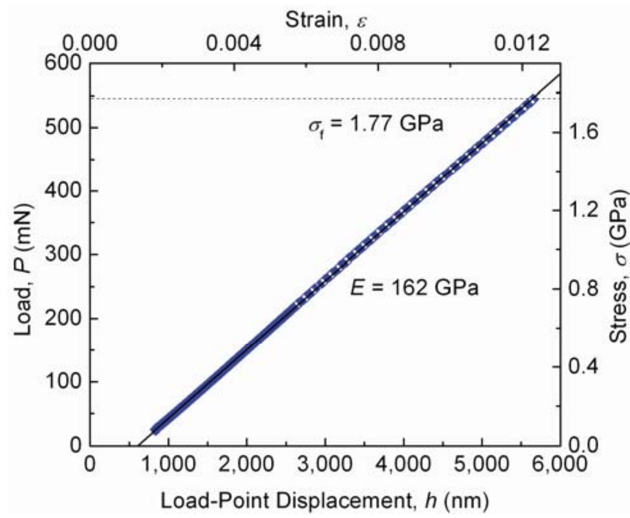

Figure 6.6: The break loading segment of the same gapped-arch theta sample in Fig. 5.5. This segment is linear with a corresponding elastic modulus of E = 162 GPa and a strength of σ_f = 1.77 GPa

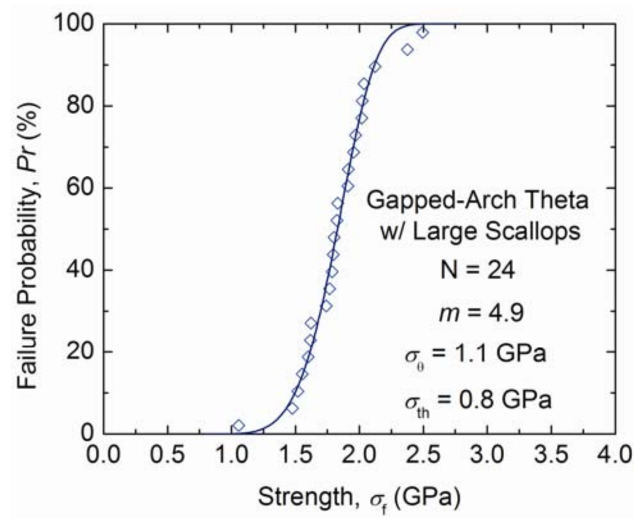

Figure 6.7: The gapped theta strength distribution and three-parameter Weibull distribution fit for the 24 tested samples. Sample strengths ranged from 1.0 GPa to 2.5 GPa. The three-parameter Weibull fit produces values of 4.9, 1.1 GPa, and 0.8 GPa for m, σ_θ, and σ_{th}, respectively.

gapped-arch theta strength value is much lower than the rest of the strength distribution in Figure 6.7. This likely has skewed the fitting results for the gapped-arch theta, reported in Table 6.2, away from the value reported in Table 6.1 for σ_{th} in the three-parameter fit of batch B samples. The Weibull modulus values determined with the two-parameter Weibull fit to the gapped-arch theta data (Figure 6.7), presented in Table 6.2, does not agree well with the batch B two-parameter Weibull modulus in Table 6.1. This may be due to the limited number of data points in Figure 6.7, or the data is simply not well-described by the two-parameter Weibull distribution due to the well-controlled etching process. The fitting results in Table 6.2 are only for the 24 data points; additional data points should result in better agreement between the three-parameter fitting results of the two sample sets.

The scaling stress, σ_{θ}, values from the three-parameter Weibull fits are also not in agreement, though this could be an issue of size scaling between the effective surface areas of the critically stressed regions of the two tested specimen types. For the arch theta, the surface area of the etched surfaces in the web region is approximately 5,750 μm^2 corresponding to the uniform tensile stress region. The equivalent area of the gapped-arch theta can be estimated from the best-fit Weibull distributions [C1683–08, 2008] because the two strength data sets come from samples created from the same processing. Recall from an earlier section that σ_{θ} is a scaling stress and the "characteristic strength" is $\sigma_{th} + \sigma_{\theta}$. This characteristic strength is utilized in the equivalent area calculation. For the three-parameter Weibull distribution [Eq. (6.1)], the equivalent surface area estimation can be determined by the relationship

Table 6.2: Weibull distribution fit data for the tested gapped-arch thetas.

		Batch B: Gapped-Arch
N		24
Three-Parameter Weibull	m	4.91 ± 1.71
	σ_θ (GPa)	1.13 ± 0.44
	σ_{th} (GPa)	0.78 ± 0.38
	R^2	0.987
Two-Parameter Weibull	m	8.67 ± 0.36
	σ_θ (GPa)	1.911 ± 0.006
	R^2	0.987

$$\frac{\sigma_{\theta 1}+\sigma_{\text{th}1}}{\sigma_{\theta 2}+\sigma_{\text{th}2}}=\left(\frac{A_2}{A_1}\right)^{1/m} \tag{6.4}$$

where $\sigma_{\theta n}$ is the scaling stress and σ_{thn} is the threshold strength for a sample set, A_n is the equivalent area for the corresponding sample set, and m is the three-parameter Weibull modulus of the flaw distribution. [In Eq (6.4) the two σ_{th} values should be the same, however as was mentioned earlier the gapped-arch distribution has been skewed downward due to a single low strength value.] Rearranging Eq (6.4) to solve for A_2, using the three-parameter fit values for σ_θ and σ_{th} from Table 6.1 and Table 6.2, and m = 3.73 from batch B in Table 6.2, the equivalent stressed area for the gapped-arch theta is approximately 8,485 μm^2. This stressed area is represented in Figure 6.8(a) with the red arcs place across the top and bottom internal sample arch structures. The calculated area is well within the arched region and this area is in agreement with the highest maximum principle stress shown in Figure 6.8(b), though the calculated region appears to represent a somewhat larger region

6.5 C-ring Strength

An example of a C-ring sample load-displacement break response is shown Figure 6.9. The trace is generally linear with a slight non-linearity for the beginning portion of this test segment. The compliance measure from the linear portion is λ = 99 nm mN^{-1}, which is in good agreement with the cyclic load responses in Fig 5.3, but again does not agree with the compliance determined by FEA. The strength of this sample, based on the simulation stress interpolation equation (Eq. 4.15), is 4.71 GPa. This is much greater than all theta sample strengths. The sample break was indicated at a load of 65 mN, much

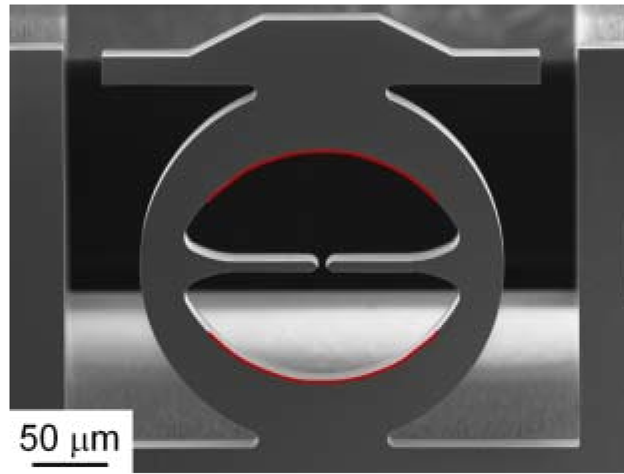

(a)

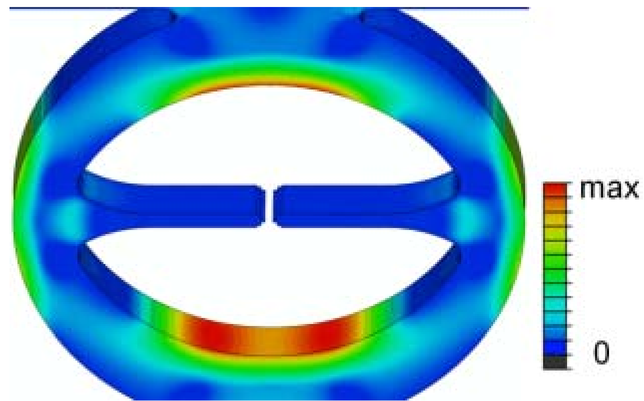

(b)

Figure 6.8: Gapped-arch theta equivalent area calculation. (a) The calculated equivalent area for the gapped-arch theta is represented by the red arches that trace across a portion of the internal arches of the sample. (b) Gapped FEA showing the maximum principle stress, tilted to observe the bottom highest stress region.

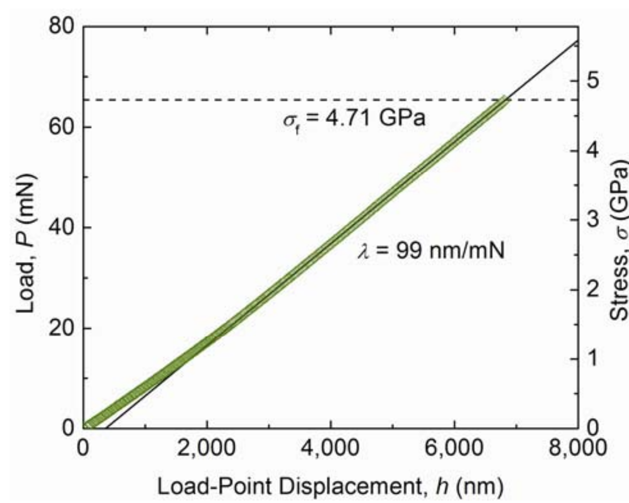

Figure 6.9: An example load-displacement data for a C-ring loaded to fracture. The compliance of this sample was λ = 99 nm mN^{-1} and the FEA translated strength is σ_f = 4.71 GPa.

greater than the load required to close the C-ring opening (approximately 20 mN). Because of these inconsistencies, it is likely that this test is invalid and the strength measurement cannot be trusted to represent a C-ring bend strength. Furthermore when all the break loads and corresponding strength values are examined it appears that every C-ring tested had this same inconsistent behavior. All C-ring load and load-point displacement data (at the point of break detection) for the tested batch B samples are presented in Figure 6.10. Break loads ranged from 45 mN to 120 mN with a corresponding strength range of 3.3 GPa and 8.7 GPa. The overall data trend in Figure 6.10 fits to a line through the origin and gives a trend compliance of $\lambda = 118$ nm mN^{-1}, a response behavior much stiffer than the predicted compliance of $\lambda_C = 937$ nm mN^{-1}. (The compliance measurement in Figure 6.10 is greater than the individual sample compliances because the displacement data has not been corrected for the seating and jumping behavior that typically occurs at the beginning of the sample test.)

The strength behavior of the C-ring should result in higher strengths than the thetas due to the smaller stressed region in the C-ring, however these calculated strength values based on this data appears significantly greater than a corresponding strength prediction would give with Eq (6.4). (The C-ring has a similar stressed area to the gapped-arch theta.) Additional work is needed to determine the cause of all the C-ring testing inconsistency. The fracture behavior of C-ring samples will be discussed in Ch. 7.

6.6 <u>*Summary*</u>

The fracture strength behavior of the theta specimens establishes structure-properties relationships for the range of fabrication batches. Each sample set exhibited fracture

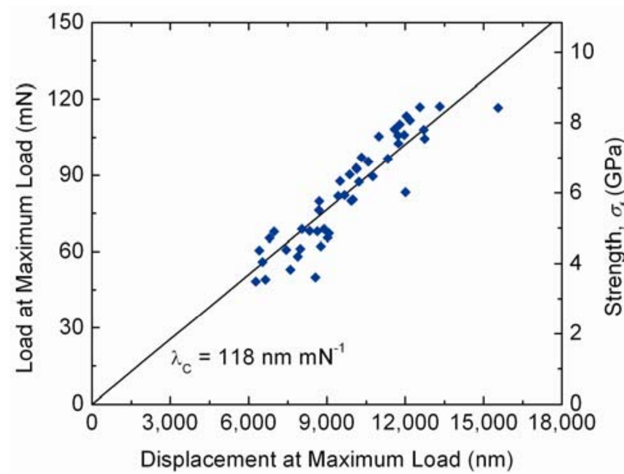

Figure 6.10: All tested C-ring break data and corresponding strengths. The C-rings load and displacement at failure have a linear trend and fitting the data to a line through the origin produces an approximate overall compliance λ_C = 118 nm mN^{-1} for all tested samples. The C-ring tests displayed strengths, based on Eq. (4.15), of between 3.3 GPa and 8.7 GPa.

strength behavior distinct to the processing, which fit well to a three-parameter Weibull distribution. Fracture strengths for the DRIE samples compare with other single-crystal silicon strength data and the processing used on these samples produced a well-controlled etch quality indicated by the relatively high Weibull modulus values. The Durelli and arch, with the same size maximum stress area, were described well on the same distribution indicating that the strength behavior is independent of test sample geometry. Equivalent surface area calculations relate the arch theta strength data to the gapped-arch theta strength data with reasonable agreement.

The C-ring fracture strength behavior, based on load-displacement responses translated with the interpolation relationship developed in Ch. 4, seem suspect based on the much larger sample strengths compared to the thetas and the unresolved C-ring load-displacement response problems and sample compliance disagreement discussed in Ch. 5. Examination of fracture behavior in the next chapter should reveal whether the C-ring sample tests were performed as intended and if sample fracture occurred in the expected sample region.

Chapter 7: Fractography

In this chapter the structure-properties relationship of the fabricated samples is examined through observations and measurements of sample fractures. This includes the fracture origin locations and plane propagations, comparisons of mirror sizes between sample batches, and crack size estimation.

7.1 Material Fracture Behavior

The fracture behavior of a particular sample provides information about the stress state, flaw location, and material properties, among other things. Examination of the fracture surface from a device or sample failure can reveal several important characteristics of the system, such as the most critical flaws in or on the sample, the loading (*e.g.*, tension, flexure) configuration the device or sample was under at failure, and fracture surface features characteristic of the sample or device material.

When a fracture occurs it initiates at a crack and propagates away from that initial crack into the surrounding material, creating new free surfaces. Prior to crack propagation and fracture, an applied load on a sample concentrates strain energy at the flaw(s), or crack. When the crack begins to advance the energy balance relationship then includes the kinetic energy of the advancing crack. The way in which the crack advances and the overall fracture surface features that occur are governed by many aspects [Lawn, 1993]. For instance, an isotropic, homogenous material in tension will start fracture with the crack accelerating and expanding orthogonal to the tensile direction. This linear propagation will not continue accelerating in a linear path to the material boundaries, but

rather the accelerating crack will reach a terminal velocity dependent upon the material that is fracturing and will branch off from the tensile orthogonal direction due to stress field deflection. When the crack reaches near terminal velocity the near-field stress cannot adjust fast enough to the accelerating crack, causing the maximum tension in front of the crack to shift away from the crack plane [Yoffe, 1951]. For an anisotropic material, the crack propagation will prefer particular cleavage planes; a crack propagating on a preferred cleavage plane will result in a resistance to crack branching until higher crack speeds are reached [Lawn, 1993]. The fracture behavior then becomes even more complicated for inhomogeneous materials and different loading configurations.

While the crack is propagating new free surfaces are being produced and kinetic energy is being created; however the energy consumed in the creation of the pairs of free surfaces will not be enough to balance the increasing mechanical energy. Once the crack reaches the boundaries the broken fragments are likely to 'fly off' when formed to release the remainder of the mechanical and strain energy. This makes it difficult to recover all sample fragments for observation, especially for greater strength samples.

Example fracture features for an anisotropic fracture are shown in the schematic diagram of Figure 7.1. In Figure 7.1(a), the fracture surface features include a smooth region, called the fracture mirror, located around the fracture causing flaw(s). Because the crack branching depends on the crack velocity for a particular material under a particular loading scheme a high strength sample will have a smaller mirror. (The size of the sample fracture mirror will be measured and compared in a later section.) Other features on the example fracture surface shown in Figure 7.1(a) moving out from the mirror surface include cathedral arcs that surround and define the fracture mirror and

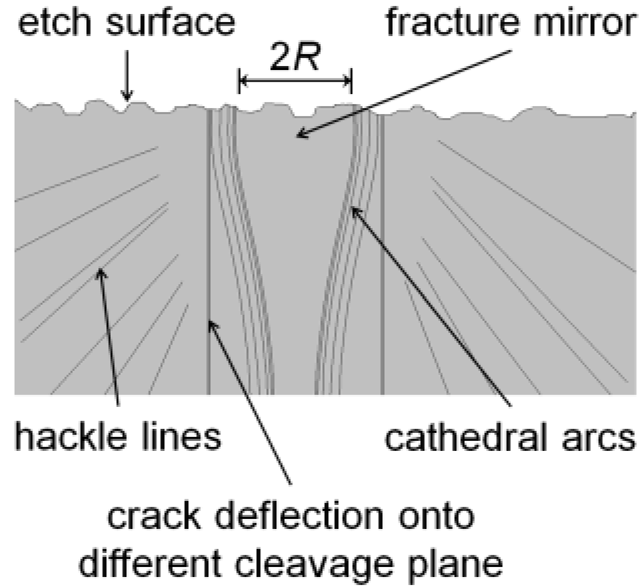

(a)

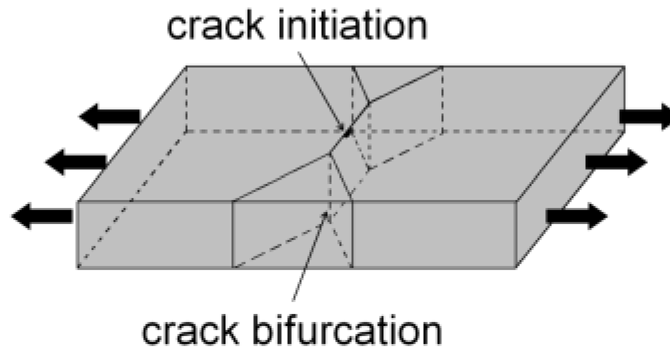

(b)

Figure 7.1: (a) Crack-scale features of the fracture surface. Fracture initiation is indicated by the fracture mirror, a smooth region surrounded by cathedral arc lines. Typically, the fracture will deflect onto a preferred cleavage plane. Hackle lines radiate from the fracture origin. (b) Specimen-scale features of the fracture surface. The crack initiates at a surface flaw, propagates perpendicular to the tensile loading, and then bifurcates or branches. For crystalline materials, this occurs along preferred cleavage planes.

hackle lines that radiate from the mirror origin. The bold vertical lines in Figure 7.1(a) denote crack deflection onto a preferred cleavage plane. On a larger scale, other fracture features include the bifurcation of the crack during fracture across the sample thickness that creates multiple fragments as is shown in schematic form in Figure 7.1(b) where the bifurcated crack in this example creates two free fragments (that would likely fly off when created and would not be recoverable for examination).

7.2 Theta Sample Fracture Behavior

Fragments from tested samples were collected to analyze the fracture behavior. Fractography was performed with field emission scanning electron microscopy (FESEM). Fracture samples were mounted on carbon taped scanning electron microscopy (SEM) stubs and organized for observations on a transmission electron microscopy (TEM) grid as shown in Figure 7.2. Fracture surfaces were examined to identify initial fracture locations, crystallographic crack propagation planes, and fracture mode.

The expected fracture cleavage planes for Si tested in tension along a <110> direction are {111} and {110} [Cook, 2006], giving rise to expected fracture planes for the web of the theta specimens as illustrated in the schematic diagram of Figure 7.3(a). FESEM images of web fracture surfaces are shown in Figure 7.3(b) and (c) for arch theta samples that contained DRIE scallop etch features [(Figure 7.3(b)] and pitting etch features (Figure 7.3(c)) on the web surfaces. In both cases, features on the fracture surfaces, including changes in fracture plane, cleavage step hackle, and arc-ribs surrounding a cathedral mirror [Tsai and Mecholsky, 1991; Quinn, 2007], enabled the fracture origin to be identified. In the two examples shown, fracture initiated on a {110}

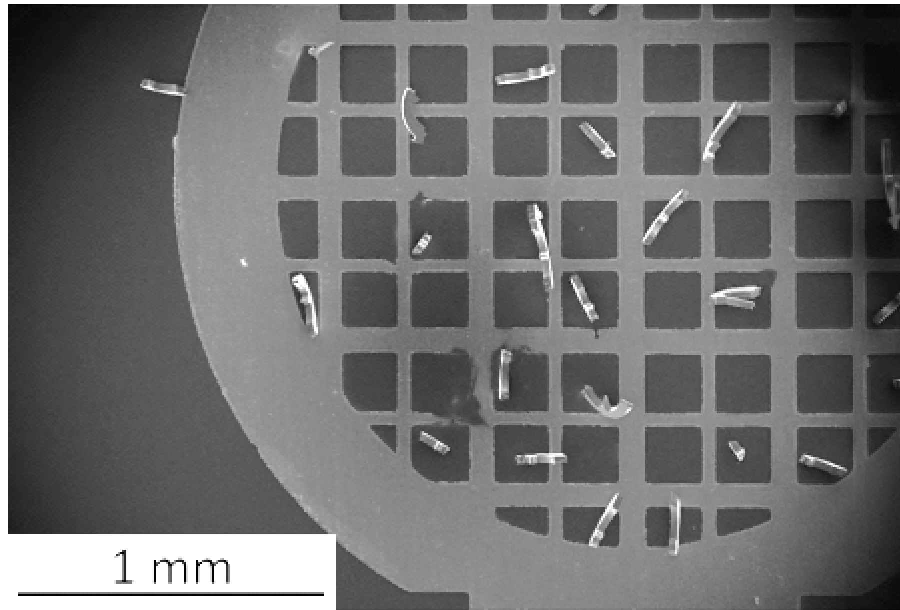

Figure 7.2: Fractography was performed by placing sample fragments between grid spaces on a TEM grid that is attached to a SEM stub. Many sample fragments have been attached in this image.

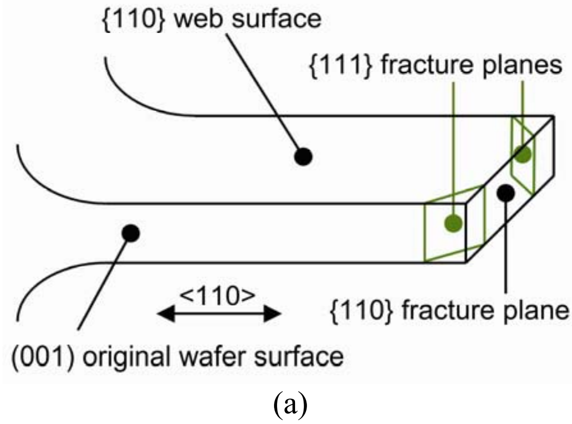

(a)

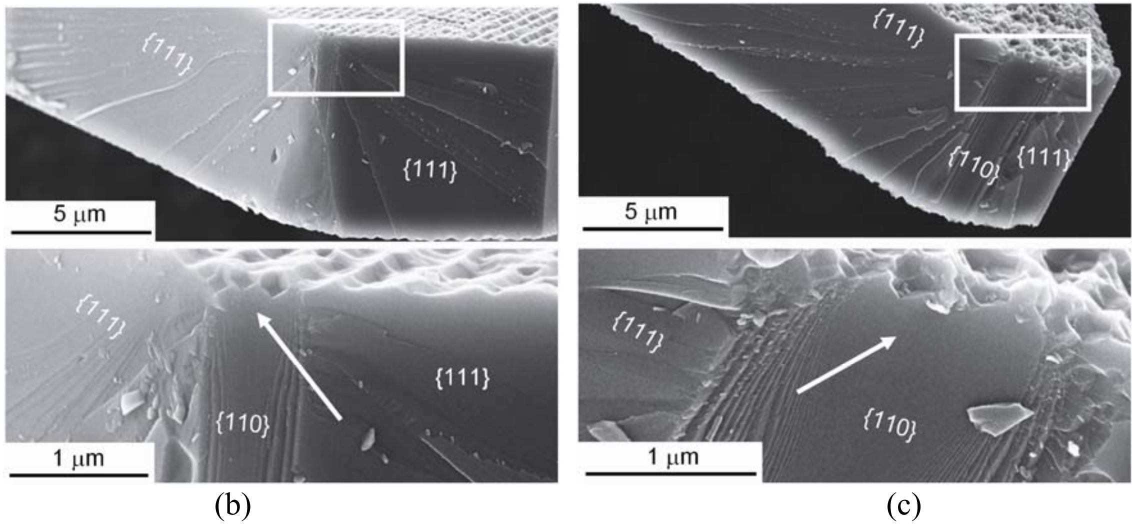

(b) (c)

Figure 7.3: (a) Schematic diagram of the {111} and {110} fracture planes that occur in the specimen web segment. (b) and (c) FESEM images of web segment fracture surfaces for the scallop and pit samples, respectively. In both examples fracture initiated on {110} fracture planes and changed to {111} fracture planes once the arc-ribs around the fracture mirror were generated. The mirror location and corresponding origin location is indicated by the arrow; in both (b) and (c), fracture initiated at a sidewall etch feature. Cleavage step hackle radiates from the fracture mirror and origin. The size of the fracture mirror in the scallop-etch example in (b) is clearly smaller than the mirror in the pit-etch example in (c).

plane perpendicular to the web long axis, and imposed tension, and after some small propagation distance deflected onto the smaller fracture energy {111} planes. Step hackle was predominantly restricted to these {111} planes and arc-ribs and associated cathedral mirrors were predominantly restricted to the initial {110} planes. The hackle, arc-ribs, and mirrors all radiated away from a single location that indicated the fracture origin, similar to Si {110} fracture observed previously [Tsai and Mecholsky, 1991]. Also in both cases, it appeared that as soon as the propagating cracks formed arc-ribs, the cracks deflected from the {110} to {111} planes. The arrows in the magnified images of Figure 7.3(b) and (c) indicate the fracture origin and the clear mirror center on the fracture surface. In the two examples, the fracture-inducing flaw is not obvious, although the web surfaces are clearly not flat at the fracture origin. These features were observed on the majority of the nearly 20 fractures surfaces examined, with one each of a complete {110} and a {111}-to-{110} failure mode also observed. Observations of fractured samples did not indicate initial fracture in any region other than the web segment.

Fractures results for batch B and C theta samples exhibited the same type of fracture behavior as the batch A samples. Figure 7.4 shows examples for these batch theta fractures. In Figure 7.4(a) the example batch B fracture initiated on a {110} fracture plane with the fracture mirror centered about a pair of etch defects from the Bosch DRIE process. The fracture deflected onto {111} fracture planes directly after the cathedral arcs were formed and hackle lines radiate outward along the {111} fracture planes indicating the fracture propagation. In Figure 7.4(b) the example batch C fracture initiated on a {110} fracture plane due to a large surface etch feature that was caused by the photoresist deterioration process observed during the cryogenic DRIE process development (see

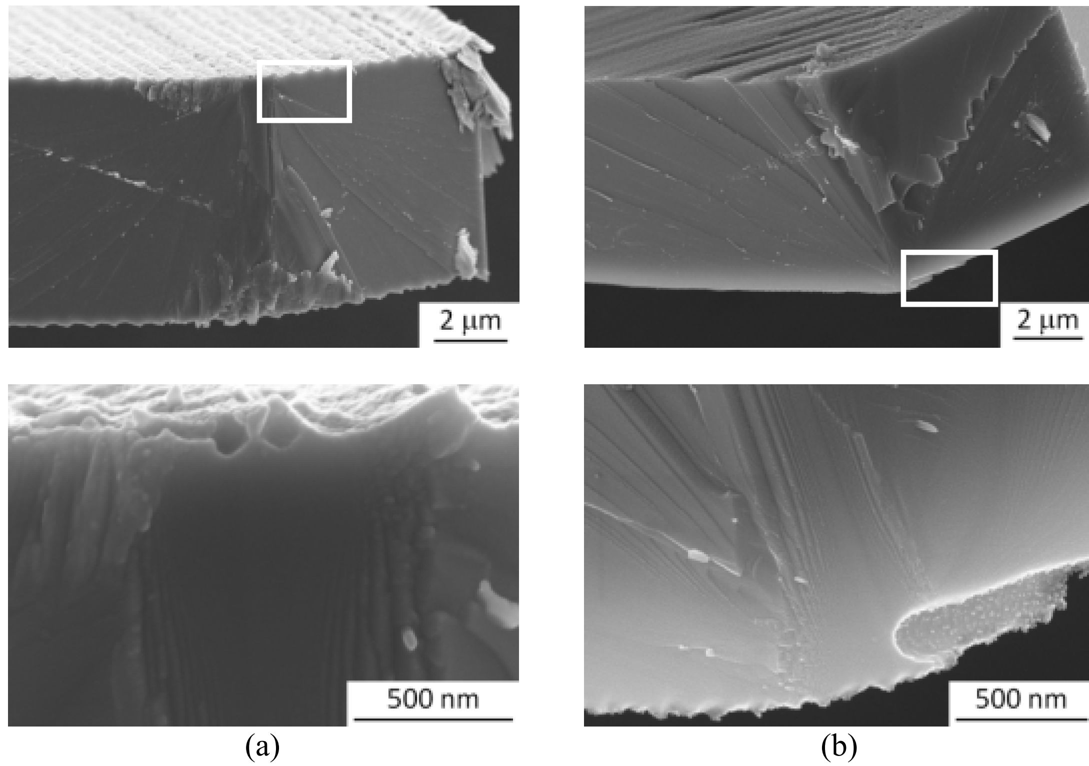

Figure 7.4: (a) An example batch B arch theta fracture surface and origin. Fracture occurred at the surface centered about a pair of flaws (bottom), initiated on {110}, and the fracture deflected onto {111} directly after cathedral arcs were formed (top). (b) An example batch C arch theta fracture surface and origin. Fracture was similar to (a). Fracture occurred at the surface due to a large etching defect (bottom), initiated on {110}, and the fracture deflected onto {111} directly after cathedral arcs were formed (top).

Ch. 2). This was the typical fracture location for the cryogenic DRIE sample; the leading etch front of this secondary etch produced an abrupt 'step' in the etched surface profile that acted as the fracture inducing flaw. Again, the fracture in Figure 7.4(b) deflected onto {111} fracture planes directly after the cathedral arcs were formed and hackle lines radiate outward along the {111} fracture planes indicating the fracture propagation.

7.3 *Fracture Mirror Radii*

Fracture mirror radii [Levengood, 1958; Johnson and Holloway, 1966; Quinn, 2007], *R*, on the fracture surfaces were estimated for comparison with the expected mirror radii calculated from the Orr equation

$$\sigma_{\mathrm{f}} R^{1/2} = A, \tag{7.1}$$

where σ_{f} is the stress at the origin at fracture and *A* is the mirror constant for Si fracture, approximately 1.6 MPa $m^{1/2}$ for the {110} tensile surface on the {110} fracture plane [Tsai and Mecholsky, 1991].

Measurements of fracture mirrors were performed on magnified images of fracture surfaces (such as in Figure 7.3(b) and (c) and Figure 7.4): The mirror radius was taken as half the separation of the first discernible cathedral arcs delineating the mirror at or near the web surface as shown schematically in Figure 7.1(a). Mirror radii, *R,* varied from just over 200 nm to 1100 nm. Combining the mirror radii with the strength values for all samples examined and using Eq. (7.1) generated a mean and standard deviation mirror constant of $A = (1.2 \pm 0.4)$ MPa $m^{1/2}$, which compares with the constant of (1.61 ± 0.14) MPa $m^{1/2}$ determined previously [Tsai and Mecholsky, 1991] for Si {110} fracture on a {110} tensile surface on micro- rather than nano-scale mirrors.

7.4 *Critical Crack Size Estimation*

The strength values were also used to estimate the critical flaw size leading to sample failure. The flaw sizes, c_s, were estimated assuming simple, non-residually-stressed flaws,

$$c_s = (T/\Psi\sigma_f)^2, \qquad (7.2)$$

where T is the material toughness, here taken as 0.71 MPa $m^{1/2}$ appropriate to the (110) plane of Si [Cook, 2006], and Ψ is a crack geometry term, here taken as $1.12\pi^{1/2}$ appropriate to a linear surface flaw [Lawn, 1993].

Fig. 3.1 shows AFM images and topographic line scans. The strength value ranges for the two strength distributions corresponding to these AFM images (batch A scallops and pits) noted in Ch. 6 and delineated in Fig. 6.3(c) are 0.8 GPa to 1.9 GPa and 1.4 GPa to 2.7 GPa. Using these strength values in Eq. (7.2) provides the corresponding critical flaw size ranges of 200 nm to 35 nm and 65 nm to 18 nm, respectively. As a consequence of the overlapping strength distributions, the estimated flaw size ranges also overlap. The pairs of dashed horizontal lines in the line scan graphs of Fig. 3.1 are separated by 35 nm [Fig. 3.1(a)] and 150 nm [Fig. 3.1(b)] indicating that the upper bounds of the calculated critical flaw sizes are comparable to the extremes of the surface topography for both surface types. Furthermore, the R_{rms} values from Table 3.1 for the batch A pits and scallops of 74.3 nm and 26.1 nm, respectively, are also comparable to the calculated critical flaw size ranges and are near the lower end of these ranges.

Figure 7.5(a) shows a schematic diagram of the failure-causing flaw as described by Eq. (7.2), a sharp edge crack of length c_s on a planar surface. Consideration of the surface roughness suggests a better representation of the flaw is that of a sharp crack of

Figure 7.5: Schematic diagrams of (a) a sharp crack on a planar surface and (b) a short sharp crack at the root of a semi-elliptical notch that is more representative of failure-causing flaws on rough etched surfaces.

length c_f at the bottom of semi-elliptical notch of depth a, as shown in Figure 7.5(b). Fracture mechanics analysis [Yamamoto *et al.*, 1974] shows that the relation between strength and size for a semi-elliptical notch with a crack flaw is Eq. (7.2) with $c_s = a + c_f$. Setting a as the characteristic topography dimensions above and using the estimated flaw sizes in this relation suggests crack lengths in the range of a few nanometers to a few tens of nanometers.

7.5 C-Ring Fractography

The C-ring samples were designed to fracture in the simulated maximum stress region of the outside C-ring, near the midline of the C (see Ch. 4). Because the C-ring specimen is a flexural test rather than a tensile test like the theta specimen, the fracture behavior should exhibit additional features to the theta sample fractures. The C-ring should have a cantilever curl structure on the fracture surface that is indicative of a bend stress field. This cantilever curl is a 'curling' away from the general fracture surface typically on the opposite side of the fracture surface from the maximum stress region. Furthermore, for the C-ring the maximum stress region is not well-aligned with a particular crystallographic orientation like the theta samples. The C-ring fracture propagation is unlikely to have a well-defined surface similar to the theta fractures in Figure 7.3(b) and (c) and Figure 7.4.

As was discussed in previous chapters (Ch. 5 and 6) the C-ring deformation response and strength behavior were problematic, with poor agreement between experimental results and theoretical predictions, as well as with other sample geometry behavior. The fracture of the C-ring should provide insight into how the sample was

loaded at failure and help explain the deformation and fracture strength behavior.

The batch B C-ring samples fractured at and above the C-ring midline. These fractures occurred on the outer surface of the C-ring as initially expected. Figure 7.6 features an example batch B C-ring fracture. In. Figure 7.6(a) the front view of the specimen shows that the fracture has occurred above the C-ring midline, approximately half-way between the midline and the top hat structure (not shown) along the C-ring curvature. Viewing closer and from the right side in Figure 7.6(b) the fracture is observed to have initiated from the outer surface of the C-ring indicated by the rough cantilever curl near the bottom of the fracture surface in the image. A closer look at the top right corner of the fracture surface in Figure 7.6(c) shows that the location of fracture initiation location is near and likely due to a fabrication error (the jutting material on the right top side). (This fabrication error is from the end of the front side etch where a small region of silicon did not completely etch away.) No clear origin is observed at this location however the hack-lines and arc-ribs extend out from this corner region, which indicates the origin of each fracture feature.

These batch B C-ring fracture observations correspond to the C-ring samples discussed in Ch. 5 and 6. Based on the simulated C-ring behavior in Ch. 4 and the disagreement with actual test data it was expected that the C-ring fracture behavior would give some indication of what may have caused the disagreement. Some indication of non-ideal testing is from the location of some of the fractures being well above the C-ring midline while none were observed below the midline. For these samples the fractures all occurred on the outside surface of the C-ring which does not suggest that the C-ring opening was closed when the sample fractured. If this had been the case the C-ring was

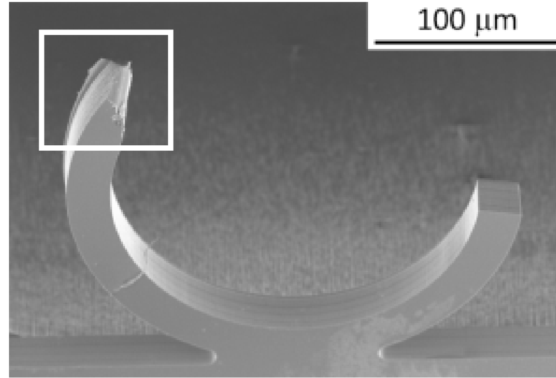

(a)

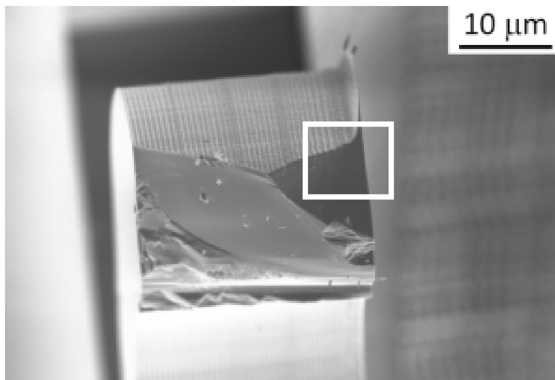

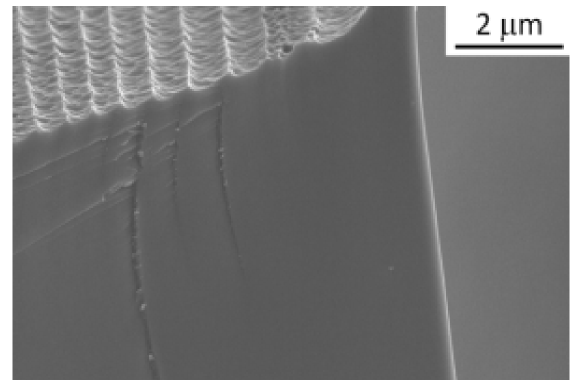

(b) (c)

Figure 7.6: Example of a batch B C-ring fracture. (a) The C-ring fracture occurred above the central high stress region located along the C-ring center line. (b) Straight-on view of the fracture face for the C-ring indicated by the box in (a). Fracture face shows cantilever curl at the bottom of the fracture face indicating that the C-ring had flexural load acting on it at fracture. (c) Fracture initiation location in the region of (b) indicated by the white box. The fracture initiated near the back edge of the C-ring near the thin layer of extra material jutting out from the sample. This material is an artifact of sample fabrication.

likely to behave like a simple ring test where the maximum stress would likely be on the inside surface likely near the top and bottom of the sample (similar to the gapped-arch theta). The fractures examined for batch B C-rings did not exhibit any inside fracture.

A preliminary investigation of the fracture of batch A C-rings exhibited fracture initiation on both the inside and outside of the C-ring, both occurring well below or above the C-ring midline. Some of these were very close to the C-ring base or top hat structure regions. These samples all had pitting etch surfaces and clear origins from the pitting etch are visible. These origins are well-defined with relatively large mirror structures with clear ribs, radiating hackle lines, and the cantilever curls indicative of flexure. The origins that occur on the outside of the C-ring suggest non-ideal loading at the moment of fracture. The origins that occurred on the inside region of the C-ring suggest that the C-ring opening had been closed at the time of fracture and the C-ring was, at that time, acting as a ring-like specimen where the maximum stress was located on the inside rather than outside of the ring specimen.

Non-ideal loading behavior was not exhibited by any of the theta samples; therefore the non-ideal loading was likely due to the C-ring sample geometry and loading response during testing rather than testing methodology. Further investigation is required to develop an understanding between the deformation and fracture strength behavior and the fractographic analysis. Design changes would likely be needed to optimize the C-ring specimen.

7.6 Summary

The fracture observations and flaw size calculations further establish the structure-

mechanical properties relationship for the theta samples. The theta samples exhibited tensile fractures in the web region. The fracture origins were located at the surface due to surface damage induced by the etching technique used, and the fracture propagated along the silicon preferred cleavage planes. The size of the fracture mirrors for the located origins were in agreement with measurements made on larger scales and the comparative sizes of the mirrors between sample sets correspond inversely to sample strengths as expected. Critical flaw size estimations were consistent with the surface roughness measurement made in Ch. 3.

The C-ring fracture observations are inconclusive. Fracture behavior of the C-ring samples present irregular cantilever curl fracture surfaces as expected, due to flexural loading and the crystallographic nature of the single-crystal silicon. The locations of the fractures were varied with few occurring in the intended location across the C-ring outer midline, though some occurred near this region. Initial fractures on the inside region of the C-ring further confuses the specimen behavior. The fracture origin locations of the C-ring samples did not exhibit any clear overall region. With these and the problematic experimental C-ring results in Ch. 5 and 6, it is clear the micro-scale C-ring specimen needs further investigation and development.

Chapter 8: Conclusions and Future Work

8.1 Conclusions

The research presented here has demonstrated that the theta specimen is an optimal test structure to measure strength at the micro-scale. The methodology of performing strength tests has been optimized to produce the best testing results with the least sensitivity to misalignments. The overall methodology, with all the optimizations and improvements of the second generation designs, allowed for straight-forward assessment and measurement of processing-structure-properties relationships for brittle materials used in MEMS fabrication.

The incorporation of a specimen hat and the use of a spherical IIT loading probe maximized the uniformity of stress in the web and minimized secondary, non-web stresses. This increased testing yield because all of the observed samples failed in the intended web segment. The arch theta specimen was designed to have smaller regions of secondary stress, but the tophat appears to have mitigated secondary stress effects for both Durelli and arch designs. Additional design, testing, and analysis features, such as separating the samples by blocks on the test strips (Fig 2.26), using a sample break detection routine, and incorporating variations in web width into the stress and strain analysis (see Ch. 4), also increased testing yield and measurement accuracy and precision. The microfabricated miniaturized theta specimens, both the original Durelli geometry and the new arch geometry, along with associated additional design features and calibration and testing protocols, provide a simple and effective method for

measuring the tensile strength of brittle materials at the micro-scale.

Statistically-relevant numbers of samples were successfully fabricated, tested, and evaluated. This is an important aspect in the assessment and optimization of a processing technique that would be used for MEMS device fabrication. Microfabrication methods allow many samples to be formed at once and the ease of use of the combined sample geometry and testing protocol allows many measurements to be performed in a time-effective manner, thus enabling statistically relevant numbers of strength measurements to be obtained. In my experiments hundreds of samples were formed on a single wafer and each sample could be tested in about five minutes. Forming the samples in a thin device layer on top of a thick handle wafer produced thick test strips incorporating thin samples that could be handled easily. This enabled sample mounting in the IIT system with negligible loading hysteresis and very small system loading compliance. Direct checking of the measured load-displacement responses to verify the accuracy of the compliance and stress and strain analyses was thus a simple matter. The ease of sample handling also enabled straightforward recovery of broken samples for post-failure analysis. This was critical in determining processing-structure-strength relationships.

The surface measurements on the etched Si samples were an important linkage in the demonstration of the usefulness of the theta specimen for establishing processing-structure-properties relations. Variations in the etching processes led to four different surface structures that in turn led to four different strength distributions (Fig. 6.5). Surface roughness analysis was used to determine that the strength-controlling flaws in the samples were controlled by the particular etch process used to fabricate each sample set. The etched surfaces exhibited a particular surface roughness character specific to the

etch process, some of which were fractal in nature, in particular the Bosch DRIE processed samples. Critical flaw size estimations were comparable to the surface roughness measurements. Fracture observations of tested samples confirmed that samples were failing due to etched surface defects.

Good agreement between the measured small-scale Young's modulus and the bulk value was found, and the strength of the samples was controlled by flaw sizes linked to the surface roughness. Although the theta specimen is unlikely to reach the throughput of the multilayer specimens (thousands of specimens at a rate of one per minute [Boyce, 2010]), the advantages of the theta geometry are that the samples are formed from a single layer, which need not be silicon, the geometry is simple, and specialized equipment beyond an IIT system is not required. In addition, samples need not necessarily be formed by lithography and microfabrication, but by focused ion-beam [Greer and Nix, 2005] or laser machining [Pecholt and Molian, 2011], for example, leading to even greater flexibility in selection of materials.

A critical enabling element of the theta specimen protocol in enhancing yield and reliability is the ability to test a statistically relevant number of samples such that a lower bound or threshold value of a strength distribution, σ_{th}, can be determined with sufficient precision to be useful in design. If a precise strength threshold can be determined, the manufacturing and reliability design processes change from the stochastic process of minimizing the probability that a component or system will fail to the deterministic process of controlling the component geometry or manufacturing or operating environments such that a component is never exposed to stresses above the threshold strength and thus never fails. Here the relative precision of the threshold strength was a

few percent, suggesting that designing components to within a safety factor of two or even less is feasible. This MEMS reliability approach is in contradistinction to other "proof testing" approaches [Boyce *et al.*, 2008], where all devices are assessed after fabrication and the processing-structure-properties relationships are not developed, thereby limiting the ability to design components for optimal behavior.

Additional sample test structures were included in the fabrication and testing to investigate how this testing methodology can be extended to other testing modes. The gapped-arch theta was an effective bend test specimen. Testing of the gapped-arch theta as a bend-test specimen produced elastic deformation results that agreed with simulated behavior and a strength distribution in good agreement with the tested theta specimen from the same fabrication batch. The C-ring specimen testing was problematic. The elastic deformation predictions and experimental testing results for sample compliance were about an order of magnitude different and the C-ring load-displacement behavior was erratic. This may have been due to the asymmetry of the C-ring, where during testing the indenter tip was able to frictionally slide across the C-ring top surface. Another aspect of the C-ring design that may have cause testing problems was the size of the C-ring opening was small enough that the C-ring opening may have closed during testing. The C-ring strength test specimen needs further development.

8.2 Future Work

The future work is divided into two parts. The first part is the extension of the materials science of the theta and related specimens to establish further processing-structure-properties relations. Future work here would include

1. Fabricating and testing theta specimens of smaller sizes than currently tested to explore scaling effects on strength. The expectation is that smaller specimens would give rise to greater strengths

2. Fabricating and testing of C-ring specimens of larger sizes than currently tested to enable direct observation of the specimen during loading. Such observations would enable potential slippage of the indenter on the specimen tophat and closure of the C-ring opening to be verified directly.

3. Developing methods to attach nanomaterials and structures across the gap of the gapped-arch theta. By using the gapped-arch theta in this manner it is utilized as a universal ultra-small mechanical test structure.

4. Extending the theta geometry to other materials and fabrication methods. Materials should include ductile materials beyond the brittle silicon currently used.

The second part is the materials engineering application of the theta specimen methodology to establish properties-performance relations. A technologically important goal of materials engineering is to establish the linkage of material properties (set by processing and structure) to the performance of components formed from the material. Future work here would include

1. Using the theta specimen to predict the manufacturing yield and operational reliability of MEMS components. Strength distributions measured with theta specimens can be used to predict the strength distributions of other components fabricated by the same process; the theta strength distribution is used as input to extrapolate to the scale of the components (in the manner of the dashed lines in Figure 1.2).

2. If the loading spectrum and reliability of the components is known or assumed, the component strength distribution established by theta specimen testing can be used to predict the lifetime spectrum of the device. Alternatively, theta specimens could be incorporated into witness chips on MEMS wafers to ensure that fabrication processes remain within specification or to enable lifetime assurance on a wafer-by-wafer basis.

3. The next step in the theta specimen development is the properties-performance relationship. This relationship should be explored explicitly for MEMS reliability by performing witness chip and threshold failure load prediction experiments in the manner mentioned above. The long range goal of the theta specimen testing methodology is to establish it as an accepted tool for properties-performance assessment and reliability optimization in the MEMS industry. To achieve this goal the witness chip and threshold load experiments should be done through inter-laboratory studies or comparisons.

Appendix

A. Web Width Determination Procedure

Below is a copy of the code developed and used on image processing software (IgorPro v6.1.0.9, Wavemetrics Inc., Lake Oswego, OR) to determine the web width of samples from captured images prior to testing. The minimum and maximum *x*- and *y*-locations (imin, imax, jmin, and jmax) to denote the web region, and image intensity values (V_min and V_max) were determined for each image prior to this running the code. This procedure was developed in collaboration with Dr. Gheorghe Stan of the National Institute of Standards and Technology.

```
=================================================================

#pragma rtGlobals=1                    // Use modern global access method.
#include <FilterDialog> menus=0
#include <All IP Procedures>
#include <Image Saver>

Function widthbar(image)

Wave image
Variable imin=520, imax=820, jmin=520, jmax=620
Variable V_min=0, V_max=228
Variable intercept
Make/O/N=((imax-imin),(jmax-jmin)) select
Make/O/N=(jmax-jmin) line
Make/O/N=(imax-imin) bar
Make/O/N=(imax-imin) horiz
Wave W_FindLevels
Variable i,j

// WaveStats/Q image
// Print V_min
// Print V_max
intercept = floor(0.5*(V_max+V_min))
Print "intercept (midpoint) =", intercept
```

```
i=0
do
        j=0
        do
                select[i][j]=image[(i+imin)][(j+jmin)]          // execute the loop body
j+=1
        while (j<(jmax-jmin))                           // as long as expression is TRUE
i+=1                                                    // execute the loop body
while (i<(imax-imin))                                   // as long as expression is TRUE

i=0
do
j=0
        do
                line[j]=select[i][j]
                j+=1                            // execute the loop body
        while (j<(jmax-jmin))                   // as long as expression is TRUE

FindLevels/Q/P line, intercept                  // find all values in 'line' above 'intercept'
bar[i]=(W_FindLevels[1]-W_FindLevels[0])

FindLevel/Q/P line, intercept                   // value where 'intercept' is first crossed
horiz[i]=V_LevelX                               // for horizontal check of web region

i+=1
while (i<(imax-imin))                           // as long as expression is TRUE

WaveStats/Q bar
Print "V_avg =", V_avg                          // Average
Print "V_sdev =", V_sdev                        // Standard Deviation

End

==================================================================
```

References

(2007). "Standard practice for reporting uniaxial strength data and estimating weibull distribution parameters for advanced ceramics." *ASTM International* **C1239-07**: 19.

Addae-Mensah, K. A., S. Retterer, S. R. Opalenik, D. Thomas, N. V. Lavrik and J. P. Wikswo (2010). "Cryogenic etching of silicon: An alternative method for fabrication of vertical microcantilever master molds." *Journal of Microelectromechanical Systems* **19**(1): 64.

Anstis, G. R., P. Chantikul, B. R. Lawn and D. B. Marshall (1981). "A critical-evaluation of indentation techniques for measuring fracture-toughness .1. Direct crack measurements." *Journal of the American Ceramic Society* **64**(9): 533.

Ashby, M. F. (1999). *Materials selection in mechanical design*. Oxford, Pergamon Press.

Aue, J. and J. T. M. DeHosson (1997). "Influence of atomic force microscope tip-sample interaction on the study of scaling behavior." *Applied Physics Letters* **71**(10): 1347.

Bagdahn, J., W. N. Sharpe and O. Jadaan (2003). "Fracture strength of polysilicon at stress concentrations." *Journal of Microelectromechanical Systems* **12**(3): 302.

Banks-Sills, L., J. Shklovsky, S. Krylov, H. A. Bruck, V. Fourman, R. Eliasi and D. Ashkenazi (2011). "A methodology for accurately measuring mechanical properties on the micro-scale." *Strain* **47**(3): 288.

Barabasi, A.-L. and H. E. Stanley (1995). *Fractal concepts in surface growth*. New York, Cambridge University Press.

Bell, D. J., T. J. Lu, N. A. Fleck and S. M. Spearing (2005). "Mems actuators and sensors: Observations on their performance and selection for purpose." *Journal of Micromechanics and Microengineering* **15**(7): S153.

Bernstein, J., S. Cho, A. T. King, A. Kourepenis, P. Maciel and M. Weinberg (1993). *A micromachined comb-drive tuning fork rate gyroscope*. Micro Electro Mechanical Systems, 1993, MEMS '93, Proceedings An Investigation of Micro Structures, Sensors, Actuators, Machines and Systems. IEEE.

Boyce, B. (2010). "A sequential tensile method for rapid characterization of extreme-value behavior in microfabricated materials." *Experimental Mechanics* **50**(7): 993.

Boyce, B. L., R. Ballarini and I. Chasiotis (2008). "An argument for proof testing brittle microsystems in high-reliability applications." *Journal of Micromechanics and Microengineering* **18**(11): 4.

Boyce, B. L., J. M. Grazier, T. E. Buchheit and M. J. Shaw (2007). "Strength distributions in polycrystalline silicon mems." *Journal of Microelectromechanical Systems* **16**(2): 179.

Bradby, J. E., J. S. Williams, J. Wong-Leung, M. V. Swain and P. Munroe (2001). "Mechanical deformation in silicon by micro-indentation." *Journal of Materials Research* **16**(5): 1500.

Brantley, W. A. (1973). "Calculated elastic-constants for stress problems associated with semiconductor devices." *Journal of Applied Physics* **44**(1): 534.

C1239–07, A. (2001). "Standard practice for reporting uniaxial strength data and estimating weibull distribution parameters for advanced ceramics." *ASTM International* **C1239–07**: 1.

C1323–96, A. (2001). "Standard test method for ultimate strength of advanced ceramics with diametrally compressed c-ring specimens at ambient temperature." *ASTM International* **C1323–96**: 6.

C1683–08, A. (2008). "Standard practice for size scaling of tensile strengths using weibull statistics for advanced ceramics." *ASTM International* **C1683–08**: 6.

Chantikul, P., G. R. Anstis, B. R. Lawn and D. B. Marshall (1981). "A critical-evaluation of indentation techniques for measuring fracture-toughness .2. Strength method." *Journal of the American Ceramic Society* **64**(9): 539.

Chekurov, N., M. Koshenvuori, V.-M. Airaksinen and I. Tittonen (2007). "Atomic layer deposition enhanced rapid dry fabrication of micromechanical devices with cryogenic deep reactive ion etching." *Journal of Micromechanics and Microengineering* **17**: 1731.

Chen, K. S., A. Ayon and S. M. Spearing (2000). "Controlling and testing the fracture strength of silicon on the mesoscale." *Journal of the American Ceramic Society* **83**(6): 1476.

Chen, K. S., A. A. Ayon, X. Zhang and S. M. Spearing (2002). "Effect of process parameters on the surface morphology and mechanical performance of silicon structures after deep reactive ion etching (drie)." *Journal of Microelectromechanical Systems* **11**(3): 264.

Cook, R. F. (2006). "Strength and sharp contact fracture of silicon." *Journal of Materials Science* **41**(3): 841.

Cook, R. F. and G. M. Pharr (1990). "Direct observation and analysis of indentation cracking in glasses and ceramics." *Journal of the American Ceramic Society* **73**(4): 787.

Craciun, G., M. A. Blauw, E. van der Drift, P. M. Sarro and P. J. French (2002). "Temperature influence on etching deep holes with sf6/o2 cryogenic plasma." *Journal of Micromechanics and Microengineering* **12**: 390.

Davidge, R. W. (1979). *Mechanical behaviour of ceramics*. Cambridge, Cambridge University Press.

de Boer, M. J., J. G. E. H. Gardeniers, H. V. Jansen, E. Smulders, M.-J. Gilde, G. Roelofs, J. N. Sasserath and M. Elwenspoek (2002). "Guidlines for etching silicon mems structures using fluoring high-density plasmas at cryogenic temperatures." *Journal of Microelectromechanical Systems* **11**(4): 385.

Dotto, M. E. R. and M. c. U. Kleinke (2002). "Scaling laws in etched si surfaces." *Physical Review B* **65**(24): 245323.

Dudley, D., W. M. Duncan and J. Slaughter (2003). *Emerging digital micromirror device (dmd) applications*. MOEMS Display and Imaging Systems, Society of Photo-Optical Instrumentation Engineers.

Durelli, A. J. (1967). Development of a specimen for a tensile test. *Applied stress analysis*. Englewood Cliffs, NJ, Prentice-Hall**:** 173.

Durelli, A. J., S. Morse and V. Parks (1962). "The theta specimen for determining tensile strength of brittle materials." *Materials Research and Standards* **2**(2): 114.

Durelli, A. J. and V. J. Parks (1962). *Relationship of size and stress gradient to brittle*

failure stress. Fourth U.S. National Congress of Applied Mechanics, University of California, Berkley, CA, The American Society of Mechanical Engineers.
Eisner, R. L. (1955). "Tensile tests on silicon whiskers." *Acta Metallurgica* **3**(4): 414.
Ericson, F. and J. A. Schweitz (1990). "Micromechanical fracture strength of silicon." *Journal of Applied Physics* **68**(11): 5840.
Fan, T.-X., S.-K. Chow and Z. Di (2009). "Biomorphic mineralization: From biology to materials." *Progress in Materials Science* **54**(5): 542.
Field, J. S. and M. V. Swain (1993). "A simple predictive model for spherical indentation." *Journal of Materials Research* **8**(2): 297.
Field, J. S. and M. V. Swain (1995). "Determining the mechanical-properties of small volumes of material from submicrometer spherical indentations." *Journal of Materials Research* **10**(1): 101.
Flater, E. E., A. D. Corwin, M. P. de Boer and R. W. Carpick (2006). "In situ wear studies of surface micromachined interfaces subject to controlled loading." *Wear* **260**(6): 580.
Fuller, E. R., D. L. Henann and L. Ma (2007). "Theta-like specimens for measuring mechanical properties at the small-scale: Effects of non-ideal loading." *International Journal of Materials Research* **98**(8): 729.
Gaither, M. S., F. W. DelRio, R. S. Gates, E. R. Fuller and R. F. Cook (2010). "Strength distribution of single-crystal silicon theta-like specimens." *Scripta Materialia* **63**(4): 422.
Gambino, J. P. and E. G. Colgan (1998). "Silicides and ohmic contacts." *Materials Chemistry and Physics* **52**(2): 99.
Gouldstone, A., N. Chollacoop, M. Dao, J. Li, A. M. Minor and Y.-L. Shen (2007). "Indentation across size scales and disciplines: Recent developments in experimentation and modeling." *Acta Materialia* **55**(12): 4015.
Greer, J. R. and W. D. Nix (2005). "Size dependence of mechanical properties of gold at the sub-micron scale." *Applied Physics A-Materials Science & Processing* **80**(8): 1625.
Gulyaev, Y. V., A. N. Kalinkin, A. Y. Mityagin and B. V. Khlopov (2010). "Advanced inorganic materials for hard magnetic media." *Inorganic Materials* **46**(13): 1403.
Hazra, S. S., M. S. Baker, J. L. Beuth and M. P. de Boer (2009). "Demonstration of an in situ on-chip tensile tester." *Journal of Micromechanics and Microengineering* **19**(8): 5.
Hazra, S. S., M. S. Baker, J. L. Beuth and M. P. de Boer (2011). "Compact on-chip microtensile tester with prehensile grip mechanism." *Journal of Microelectromechanical Systems* **20**(4): 1043.
Henry, M. D., C. Welch and A. Scherer (2009). "Techniques of cryogenic reactive ion etching in silicon for fabrication of sensors." *Journal of Vacuum Science & Technology A* **27**(5): 1211.
Hoffmann, S., I. Utke, B. Moser, J. Michler, S. H. Christiansen, V. Schmidt, S. Senz, P. Werner, U. Gosele and C. Ballif (2006). "Measurement of the bending strength of vapor-liquid-solid grown silicon nanowires." *Nano Letters* **6**(4): 622.
Holm, B., R. Ahuja, Y. Yourdshahyan, B. Johansson and B. I. Lundqvist (1999). "Elastic and optical properties of alpha- and kappa-al(2)o(3)." *Physical Review B* **59**(20): 12777.

Hu, S. M. (1982). "Critical stress in silicon brittle-fracture, and effect of ion-implantation and other surface treatments." *Journal of Applied Physics* **53**(5): 3576.
Isono, Y., T. Namazu and N. Terayama (2006). "Development of afm tensile test technique for evaluating mechanical properties of sub-micron thick dlc films." *Journal of Microelectromechanical Systems* **15**(1): 169.
Jadaan, O. M., N. N. Nemeth, J. Bagdahn and W. N. Sharpe (2003). "Probabilistic weibull behavior and mechanical properties of mems brittle materials." *Journal of Materials Science* **38**: 4087.
Jansen, H., M. de Boer, R. Legtenberg and M. Elwenspoek (1995). "The black silicon method: A universal method for determining the parametersetting of a fluorine-based reactive ion etcher in deep silicon trench etching with profile control." *Journal of Micromechanics and Microengineering* **5**: 115.
Jansen, H., M. de Boer, H. Wensink, B. Kloeck and M. Elwenspoek (2001). "The black silicon method. Viii. A study of the performance of etching silicon using sf6/o2-based chemistry with cryogenical wafer cooling and a high density icp source." *Microelectronics Journal* **32**: 769.
Jansen, H. V., M. J. de Boer, S. Unnikrishnan, M. C. Louwerse and M. C. Elwenspoek (2009). "Black silicon method x: A review on high speed and selective plasma etching of silicon with profile control: An in-in-depth comparison between bosch and cryostat drie processes as a roadmap to next generation equipment." *Journal of Micromechanics and Microengineering* **19**(033001): 1.
Jeong, S. M., S. E. Park, H. S. Oh and H. L. Lee (2004). "Evaluation of damage on silicon wafers using the angle lapping method and a biaxial fracture strength test." *Journal of Ceramic Processing Research* **5**(2): 171.
Johansson, S., J.-A. Schweitz, L. Tenerz and J. Tiren (1988). "Fracture testing of silicon microelements in situ in a scanning electron microscope." *Journal of Applied Physics* **63**(10): 4799.
Johnson, J. W. and D. G. Holloway (1966). "On the shape and size of the fracture zones on glass fracture surfaces." *Philosophical Magazine* **14**(130): 731.
Kamto, A., R. Divan, A. V. Sumant and S. L. Burkett (2010). "Cryogenic inductively coupled plasma etching for fabrication of tapered through-silicon vias." *Journal of Vacuum Science & Technology A* **28**(4): 719.
Kim, H. (2003). "Atomic layer deposition of metal and nitride thin films: Current research efforts and applications for semiconductor device processing." *Journal of Vacuum Science & Technology B* **21**(6): 2231.
Kovacs, G. T. A. (1998). *Micromachined transducers sourcebook*. New York, NY, McGraw-Hill.
Lawn, B. R. (1993). *Fracture of brittle solids*. Cambridge, Cambridge University Press.
Le, H. P. (1998). "Progress and trends in ink-jet printing technology." *Journal of Imaging Science and Technology* **42**(1): 49.
Levengood, W. C. (1958). "Effect of origin flaw characteristics on glass strength." *Journal of Applied Physics* **29**(5): 820.
Li, J., Q. X. Zhang and A. Q. Liu (2003). "Advanced fiber optical switches using deep rie (drie) fabrication." *Sensors and Actuators a-Physical* **102**(3): 286.
Liu, Y. H., D. Wang, K. Nakajima, W. Zhang, A. Hirata, T. Nishi, A. Inoue and M. W. Chen (2011). "Characterization of nanoscale mechanical heterogeneity in a

metallic glass by dynamic force microscopy." *Physical Review Letters* **106**(12): 4.
Lord, J. D., B. Roebuck, R. Morrell and T. Lube (2010). "25 year perspective: Aspects of strain and strength measurement in miniaturised testing for engineering metals and ceramics." *Materials Science and Technology* **26**(2): 127.
Madou, M. J. (2002). *Fundamentals of microfabrication: The science of miniaturization*. Boca Raton, FL, CRC Press.
McLaughlin, J. C. and A. F. W. Willoughby (1987). "Fracture of silicon-wafers." *Journal of Crystal Growth* **85**(1-2): 83.
McSkimin, H. J. and P. Andreatch (1964). "Measurement of third-order moduli of silicon and germanium." *Journal of Applied Physics* **35**(11): 3312.
Mencik, J., D. Munz, E. Quandt, E. R. Weppelmann and M. V. Swain (1997). "Determination of elastic modulus of thin layers using nanoindentation." *Journal of Materials Research* **12**(9): 2475.
Miller, D. C., B. L. Boyce, M. T. Dugger, T. E. Buchheit and K. Gall (2007). "Characteristics of a commercially available silicon-on-insulator mems material." *Sensors and Actuators A: Physical* **138**(1): 130.
Mohanty, B. C., H. R. Choi and Y. S. Cho (2009). "Scaling of surface roughness in sputter-deposited zno:Al thin films." *Journal of Applied Physics* **106**(5): 6.
Nakao, S., T. Ando, M. Shikida and K. Satol (2006). "Mechanical properties of a micron-sized scs film in a high-temperature environment." *Journal of Micromechanics and Microengineering* **16**(4): 715.
Namazu, T., Y. Isono and T. Tanaka (2000). "Evaluation of size effect on mechanical properties of single crystal silicon by nanoscale bending test using afm." *Journal of Microelectromechanical Systems* **9**(4): 450.
Oliver, W. C. and G. M. Pharr (1992). "An improved technique for determining hardness and elastic-modulus using load and displacement sensing indentation experiments." *Journal of Materials Research* **7**(6): 1564.
Oliver, W. C. and G. M. Pharr (2004). "Measurement of hardness and elastic modulus by instrumented indentation: Advances in understanding and refinements to methodology." *Journal of Materials Research* **19**(1): 3.
Oyen, M. L. and R. R. Cook (2009). "A practical guide for analysis of nanoindentation data." *Journal of the Mechanical Behavior of Biomedical Materials* **2**(4): 396.
Parkin, S., X. Jiang, C. Kaiser, A. Panchula, K. Roche and M. Samant (2003). "Magnetically engineered spintronic sensors and memory." *Proceedings of the IEEE* **91**(5): 661.
Pearson, G. L., W. T. Read and W. L. Feldmann (1957). "Deformation and fracture of small silicon crystals." *Acta Metallurgica* **5**(4): 181.
Pecholt, B. and P. Molian (2011). "Nanoindentation of laser micromachined 3c-sic thin film micro-cantilevers." *Materials & Design* **32**(6): 3414.
Persson, B. N. J., O. Albohr, U. Tartaglino, A. I. Volokitin and E. Tosatti (2005). "On the nature of surface roughness with application to contact mechanics, sealing, rubber friction and adhesion." *Journal of Physics-Condensed Matter* **17**(1): R1.
Quinn, G. D. (2007). *Fractography of ceramics and glasses*. Washington, DC, National Institute of Standards and Technology.
Quinn, G. D. (2008). "Fractographic analysis of miniature theta specimens." *Ceramic Engineering and Science Proceedings* **29**(3): 189.

Quinn, G. D. (2009). Fractographic analysis of very small theta specimens. *Fractography of advanced ceramics iii*. J. Dusza, R. Danzer, R. Morrell and G. D. Quinn. Stafa-Zurich, Switzerland, Key Engineering Materials. **409:** 201.

Quinn, G. D., E. Fuller, D. Xiang, A. Jillavenkatesa, L. Ma, D. Smith and J. Beall (2005). "A novel test method for measuring mechanical properties at the small-scale: The theta specimen." *Ceramic Engineering and Science Proceedings* **26**(2): 117.

Romig, A. D., M. T. Dugger and P. J. McWhorter (2003). "Materials issues in microelectromechanical devices: Science, engineering, manufacturability and reliability." *Acta Materialia* **51**(19): 5837.

Sainiemi, L. and S. Franssila (2007). "Mask material effects in cryogenic deep reactive ion etching." *Journal of Vacuum Science & Technology B* **25**(3): 801.

Schweitz, J.-Å. and F. Ericson (1999). "Evaluation of mechanical materials properties by means of surface micromachined structures." *Sensors and Actuators A: Physical* **74**(1-3): 126.

Senturia, S. D. (2001). *Microsystem design*. Boston, Kluwer Academic Publishers.

Sharpe, W. N., B. Yuan and R. L. Edwards (1997). "A new technique for measuring the mechanical properties of thin films." *Journal of Microelectromechanical Systems* **6**(3): 193.

Slaughter, J. M. (2009). "Materials for magnetoresistive random access memory." *Annual Review of Materials Research* **39**: 277.

Soref, R. A. (1993). "Silicon-based optoelectronics." *Proceedings of the IEEE* **81**(12): 1687.

Spearing, S. M. (2000). "Materials issues in microelectromechanical systems (mems)." *Acta Materialia* **48**(1): 179.

Sun, Y., S. N. Fry, D. P. Potasek, D. J. Bell and B. J. Nelson (2005). "Characterizing fruit fly flight behavior using a microforce sensor with a new comb-drive configuration." *Journal of Microelectromechanical Systems* **14**(1): 4.

Sundararajan, S., B. Bhushan, T. Namazu and Y. Isono (2002). "Mechanical property measurements of nanoscale structures using an atomic force microscope." *Ultramicroscopy* **91**: 111.

Suwito, W., M. L. Dunn, S. J. Cunningham and D. T. Read (1999). "Elastic moduli, strength, and fracture initiation at sharp notches in etched single crystal silicon microstructures." *Journal of Applied Physics* **85**(7): 3519.

Sylwestrowicz, W. (1962). "Mechanical properties of single crystals of silicon." *Philosophical Magazine* **7**(83): 1825.

Tsai, Y. L. and J. J. Mecholsky (1991). "Fractal fracture of single-crystal silicon." *Journal of Materials Research* **6**(6): 1248.

Tsuchiya, T., M. Hirata, N. Chiba, R. Udo, Y. Yoshitomi, T. Ando, K. Sato, K. Takashima, Y. Higo, Y. Saotome, H. Ogawa and K. Ozaki (2005). "Cross comparison of thin-film tensile-testing methods examined using single-crystal silicon, polysilicon, nickel, and titanium films." *Journal of Microelectromechanical Systems* **14**(5): 1178.

Tsui, K., A. A. Geisberger, M. Ellis and G. H. Skidmore (2004). "Micromachined end-effector and techniques for directed mems assembly." *Journal of Micromechanics and Microengineering* **14**(4): 542.

Van Kessel, P. F., L. J. Hornbeck, R. E. Meier and M. R. Douglass (1998). "A mems-

based projection display." *Proceedings of the IEEE* **86**(8): 1687.
van Spengen, W. M. (2003). "Mems reliability from a failure mechanisms perspective." *Microelectronics Reliability* **43**(7): 1049.
Vedde, J. and P. Gravesen (1996). "The fracture strength of nitrogen doped silicon wafers." *Materials Science and Engineering B* **36**: 246.
Walker, M. J. (2001). "Comparison of bosch and cryogenic processes for patterning high aspect ratio features in silicon." *Proceedings of the Society of Photo-Optical Instrumentation Engineers*.
Wallace, R. M. and G. D. Wilk (2003). "High-kappa dielectric materials for microelectronics." *Critical Reviews in Solid State and Materials Sciences* **28**(4): 231.
Weibull, W. (1951). "A statistical distribution function of wide applicability." *Journal of Applied Mechanics-Transactions of the ASME* **18**(3): 293.
Wilson, C. J. and P. A. Beck (1996). "Fracture testing of bulk silicon microcantilever beams subjected to a side load." *Journal of Microelectromechanical Systems* **5**(3): 142.
Wilson, C. J., A. Ormeggi and M. Narbutovskih (1996). "Fracture testing of silicon microcantilever beams." *Journal of Applied Physics* **79**(5): 2386.
Yamamoto, Y., Y. Sumi and K. Ao (1974). "Stress intensity factors of cracks emanating from semi-elliptical side notches in plates." *International Journal of Fracture* **10**(4): 593.
Yan, R., D. Gargas and P. Yang (2009). "Nanowire photonics." *Nature Photonics* **3**(10): 569.
Yang, H. N., A. Chan and G. C. Wang (1993). "Examination of the multilevel diffraction model for interface roughness characterization by scanning-tunneling-microscopy." *Journal of Applied Physics* **74**(1): 101.
Yang, H. N., Y. P. Zhao, A. Chan, T. M. Lu and G. C. Wang (1997). "Sampling-induced hidden cycles in correlated random rough surfaces." *Physical Review B* **56**(7): 4224.
Yi, T. C., L. Li and C. J. Kim (2000). "Microscale material testing of single crystalline silicon: Process effects on surface morphology and tensile strength." *Sensors and Actuators* **83**: 7.
Yoffe, E. H. (1951). "The moving griffith crack." *Philosophical Magazine* **42**(330): 739.
Zhao, Y.-P., J. T. Drotar, G.-C. Wang and T.-M. Lu (1999). "Roughening in plasma etch fronts of si(100)." *Physical Review Letters* **82**(24): 4882.
Zhao, Y. P., J. B. Fortin, G. Bonvallet, G. C. Wang and T. M. Lu (2000). "Kinetic roughening in polymer film growth by vapor deposition." *Physical Review Letters* **85**(15): 3229.
Zhu, Y., F. Xu, Q. Q. Qin, W. Y. Fung and W. Lu (2009). "Mechanical properties of vapor-liquid-solid synthesized silicon nanowires." *Nano Letters* **9**(11): 3934.

Curriculum Vitae

Michael Scott Gaither

Education

2006-2011 University of Maryland, College Park, Maryland

Ph.D. Materials Science and Engineering

2001-2006 Austin Peay State University, Clarksville, Tennessee

B.S. Physics

Publications

1. M.S. Gaither, F.W. DelRio, R.S. Gates, and R.F. Cook, “Effects of Plasma-Etched Silicon Surfaces on the Strength of Microscale Theta Specimens,” *Journal of Materials Research* **26** 2575 (2011). (Invited)

2. M.S. Gaither, F.W. DelRio, R.S. Gates, E.R. Fuller, Jr., and R.F. Cook, “Strength distribution of single-crystal silicon theta-like specimens,” *Scripta Materialia*, **63** 422 (2010).

3. M.S. Gaither, F.W. DelRio, R.S. Gates, E.R. Fuller, Jr., and R.F. Cook, “Theta-like specimen to determine tensile strength at the micro scale,” *IEEE 23rd International Conference on Micro Electro Mechanical Systems (MEMS)*, 540 (2010).

Presentations

1. M.S. Gaither, F.W. DelRio, R.S. Gates, and R.F. Cook, "Effects of Deep Reactive Ion Etching on the Strength of Micro-Scale Theta Specimens," The Society of Experimental Mechanics Annual Meeting, Metrology and Standards for MEMS and NEMS, oral presentation (2011).

2. M.S. Gaither, F.W. DelRio, R.S. Gates, and R.F. Cook, "Effects of Plasma-Etched Silicon Surfaces on the Strength of Theta-like Micromechanical Test Structures," *The Materials Research Society Fall Meeting*, Microelectromechanical Systems: Materials and Device IV, oral presentation (2010).

3. M.S. Gaither, F.W. DelRio, G.D. Quinn, R.S. Gates, E.R. Fuller, Jr., and R. F. Cook, "Theta-like Specimens to Determine Tensile Strength at the Micro Scale," *The Minerals, Metals, and Materials Society Fall Meeting*, Failure of Small-Scale Structures: Device Failure and Fatigue, oral presentation (2010).

4. M.S. Gaither, F.W. DelRio, G.D. Quinn, R.S. Gates, and R.F. Cook, "New Test-Specimen Geometries for MEMS-scale Measurement of Tensile and Bending Strength," *The Materials Research Society Fall Meeting*, Microelectromechanical Systems: Materials and Device II, oral presentation (2008).

5. M.S. Gaither, F.W. DelRio, R.S. Gates, and R.F. Cook. "Microscale Theta Specimen to Determine Tensile Strength," *11th Mid-Atlantic Micro/Nano Alliance Symposium,* JHU Applied Physics Laboratory, poster presentation (2010).

6. M.S. Gaither, F.W. DelRio, R.S. Gates, E.R. Fuller, Jr., and R.F. Cook. "Theta-like Specimen to Determine Tensile Strength at the Micro and Nano Scale," *Nanomaterials Symposium,* JHU Applied Physics Laboratory, poster presentation (2010).